Freak Wave Analysis in High-Order Weak Non-linear Wave Interaction with Bottom Topography Change

Zuorui Lyu

2021

Abstract

With the development of observation technology, we found a kind of disaster named “freak wave” in deep ocean water. It is also known as “rogue wave”, “giant wave” and “extreme wave”, which has abnormally huge waves bringing about a risk for the vessels and marine structures. The generation of the freak wave comes from the quasi-resonant four-wave interaction of high-order non-linear modulated wave train, and the occurrence probability of freak wave in deep-water can be estimated by the fourth-order cumulant of surface elevation. From recent observation records and physical experiments, freak wave not only occurs in deep and finite water but also in shallow water and offshore area.

The Non-linear Schrödinger (NLS) equation is widely applied in the numerical simulation of the freak wave, since it reflects the high-order interaction in the modulated non-linear wave trains. Modified NLS equation can derived based on different hypotheses and boundary conditions. In this study, we derive the modified NLS equation over an uneven bottom in a two-dimensional wavefield, and establish a numerical evolution model of the envelope of modulated wave trains. The contribution from four-wave interaction to the wave train instability is considered as an initial value problem, and we integrate the envelope from the offshore to onshore assuming periodic boundary conditions in time to give wave surface elevation through the pseudo spectral method and discrete Fourier transform. Setting random phase in initial data, we conduct a Monte Carlo simulation to analyze the evolution of the high-order nonlinearity and the occurrence of extreme events in the statistics of wave surface elevation. Compared with the previous studies, we give an exhaustive discussion about the evolution of the non-linear effect and its reflection in real surface elevation, and consider the effect from the shape of bottom topography specifically.

Firstly, we summarize the simulation from the unidirectional modulated wave train, and concentrate on the contribution from the initial condition and spatial inhomogeneity on the

surface instability. We take the mean value of the high-order moment of surface elevation to reflect the nonlinearity in wave train and record the distribution of the maximum wave height and crest in the Monte Carlo simulation. The result indicates, the four-wave interaction contributes to the occurrence probability of extreme events in deep-water, and the second-order effect becomes an important factor in medium and shallow water. A steep slope angle will lead to the increase of the occurrence probability of the freak wave in the wave shoaling.

Based on the numerical analysis of the unidirectional wave, we expand the non-linear evolution model into a two-dimensional wavefield. The directional dispersion effect is taken into consideration as a parameter in the initial condition, which disperses the four-wave interaction and gives a lower instability. Additionally, we discuss the wave evolution over different types of bottom shapes and the oblique incident wave case with a small angle between the principal direction and the gradient of depth.

Key word: *freak wave*; *NLS equation; modulated wave train; two-dimensional wavefield; spatial inhomogeneity; directional dispersion*

Acknowledgements

Many years later, as he faced this thesis, the author was to remember those late nights that he spent on the derivation of formulas and searching for bugs in the program.

When I graduated from high school and was admitted to the hydraulic engineering, I started working in water wave-related research. I arrived in Japan in Oct 2018 for my PhD at Kyoto University, and this thesis is a summary of my three years of work on the non-linear wave evolution.

The accomplishment of this thesis is inseparable from the kind help from my supervisor Prof. Nobuhito Mori. I received so much useful advice from him, and every discussion with him was very enlightening for me.

I deeply appreciate Dr. Hiroaki Kashima about the help in calculation program and advice for the manuscript.

In the derivation of theoretical work, I acknowledge Prof. Karsten Trulsen and Dr. Junlong Lyu's suggestions about Taylor series and complex analysis.

I would like to thank for the economic support from the MEXT scholarship from the Ministry of Education, Culture, Sports, Science, and Technology of the Government of Japan.

I also want to thank all members of the coastal engineering laboratory. It's an impressive experience for me to work with them, especially Dr. Audrius Sabūnas and Dr. Nobuki Fukui who have been with me for the whole three years.

Finally, I am sincerely grateful to my family members. They support all of my plans and decisions, which gives me the opportunity to do whatever I want to do.

Contents

Chapter 1

Introduction

1.1 Background

As the development of observation technology in these decades, a special type of wave records has been found in deep-water showing how the vessels and marine structures were destroyed by the huge wave crest without any portent. With the summary from reports and stories mainly from the North Pacific and the North Atlantic, Draper (1965) introduced a concept as “freak wave” for the waves with very abnormal wave height. This disaster is also known as “rogue wave”, “giant wave” and “extreme wave”, and usually it was defined as the wave height exceeds the significant wave height by a factor of 2. Not only in water waves, a similar phenomenon has also been found in other mediums, such as acoustic and optical waves.

With the systematical and comprehensive data collection and analyzation, thousands of freak waves have been found in the ocean. **Figure 1.1** gives the wave data as one of the highest wave crests ever recorded in the North Sea by the Draupner platform on Jan 1st 1995 in the North Sea from Haver (2004), which is also called “New Year’s Wave” as a famous freak wave. In **Figure 1.1 (a)**, a spike is recorded at around 250s with a very large crest, which brings about a wave height in 25.6m while the significant wave height is 12m in this group of wave trains. **Figure 1.1 (b)** gives the record of surface elevation for twenty minutes in the next hour, and there is no freak wave that can be observed. In this typical case, the duration of the freak wave is very short, but the prodigious wave height is too dangerous for navigation and marine structures.

In the early study about the generation mechanism of the freak wave, researchers

concentrated on the linear random wave theory and external influence such as wind and current interaction. Dean (1990) discussed the probability density function of extreme events in the linear model based on the Rayleigh distribution for wave heights, and the observed data in field significantly disagreed with the Rayleigh distribution. Wind effect on wave instability has been considered in the study from Kharif et al. (2008), and the result suggested the wind forcing on energy focusing process of the freak wave is limited. Based on the non-linear wave evolution model, Benjamin(1967) indicated that modulational instability will lead to the generation of spectral-sidebands effect and the eventual breakup of the waveform in a uniform wave train by nonlinearity, which is considered to become an important reason causing freak wave in deep-water after 90's.

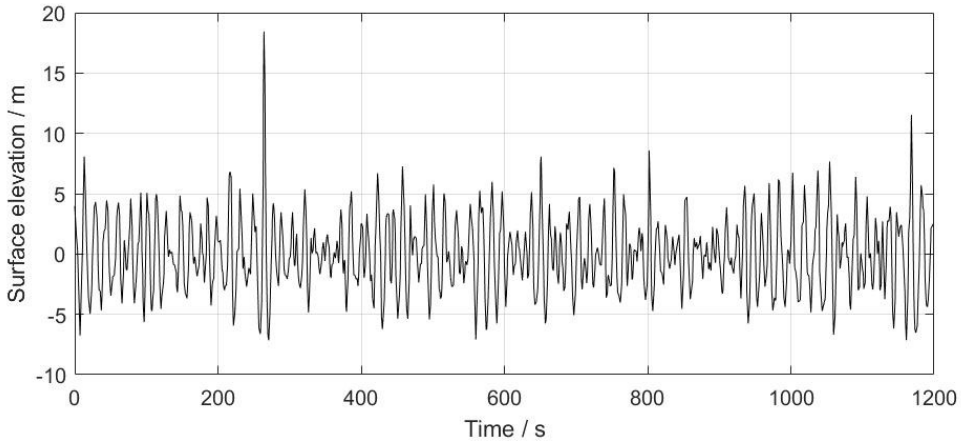

(a) Wave record 1520.

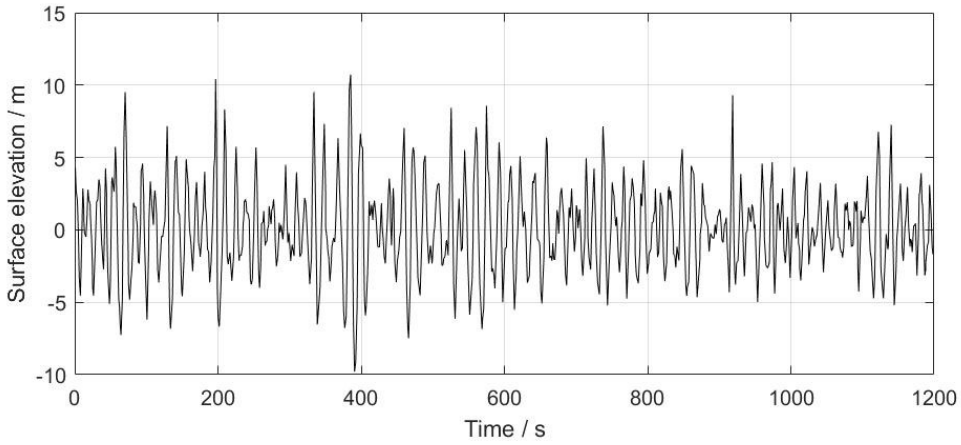

(b) Wave record 1620.

Figure 1.1. Surface elevation in time series recorded by the Draupner platform on Jan 1st 1995 in the North Sea (Haver, 2004)

In the early 90's, preliminary numerical and experimental studies have demonstrated that the freak wave can be generated in the long-distance propagation of random waves in deep-water (Stansberg, 1990, Yasuda et al., 1992). Compared with other mechanisms and theoretical models, modulated wave trains can predict the occurrence probability of the freak wave in a more accurate way with the consideration of the surface instability due to the high-order non-linear interactions.

The total energy of the fluid Ef can be expressed in an expansion in terms of wave steepness ε from Hamiltonian:

$$Ef = \varepsilon^2 Ef_2 + \varepsilon^3 Ef_3 + \varepsilon^4 Ef_4 + O(\varepsilon^5), \qquad (1-1)$$

where the subscript represents the contribution from different orders of ε. The second-order term corresponds to the linear wave, and the third-order and fourth-order term correspond to the contribution from the non-linear effect, which are also known as three-wave interaction and four-wave interaction. In deep-water, the contribution from the three-wave interaction to wave energy is very limited, and the wavefield is mainly determined by the fourth-wave interaction (Janssen, 2003; Krasitskii, 1990). The relation between the fourth-wave interaction and wave envelope reflects in the Zakharov equation (Zakharov, 1968):

$$\frac{\partial b_1}{\partial t} + \mathrm{i}\omega_1 b_1 = -\mathrm{i} \iiint_{-\infty}^{\infty} d\boldsymbol{k_2}\, d\boldsymbol{k_3} d\boldsymbol{k_4} T_{1,2,3,4} b_2^* b_3 b_4 \delta_{1+2-3-4}, \qquad (1-2)$$

where b is the function of amplitude, $\boldsymbol{k}$ is wave number vector, the subscript represents the contribution from different orders and $b_1 = b(\boldsymbol{k_1})$. $T_{1,2,3,4}$ is the non-linear transfer coefficient and δ is Dirac delta function.

Modulational instability represents how much wave energy focusing through four-wave interaction from the different harmonics in wave train, and it can be estimated by a dimensionless number named Benjamin–Feir index (BFI) introduced by Janssen (2003) based on narrowband approximation of Zakharov equation:

$$\mathrm{BFI} = \frac{\sqrt{2}\varepsilon}{\sigma_s}, \qquad (1-3)$$

where σ_s is dimensionless spectral bandwidth. This ratio gives the balance between nonlinearity and the dispersion.

The prediction theory of the freak wave is combined between high-order non-linear theory and random wave statistics. Mori and Janssen (2006) discussed the distribution of maximum

wave height in deep-water, and gave exceeding probability function of extreme events, which is determined by the kurtosis of surface elevation. Kurtosis μ_4 and skewness μ_3 are dimensionless moment in the fourth-order and third-order of surface elevation η:

$$\mu_4 = \frac{EX\left(\eta_i - \bar{\eta}\right)^4}{\eta_{\mathrm{rms}}^4}, \qquad \mu_3 = \frac{EX\left(\eta_i - \bar{\eta}\right)^3}{\eta_{\mathrm{rms}}^3}, \tag{1-4}$$

where EX represents expected value, $\bar{\eta}$ is the mean value and η_{rms} is the root mean square value of η. For a wave train in the Gaussian process (i.e. linear random waves), μ_4 = 3 and μ_3 = 0. The value of μ_4 can be changed with different non-linear processes or hypotheses. For a narrowband second-order non-linear wave train, the Stokes wave model gives contribution from bound wave (Longuet-Higgins, 1963). Thus, values of μ_4 and μ_3 are related to the wave steepness ε:

$$\mu_4^b = 3 + 24\varepsilon^2, \qquad \mu_3^b = 3\varepsilon. \tag{1-5}$$

In Janssen (2003) and Mori and Janssen (2006), μ_4 can be changed on the quasi-resonant and non-resonant interactions than Eq.(1-5). It is parameterized by the fourth-order cumulant κ_{40}, which is proportional to the square of BFI defined by Janssen (2003):

$$\mu_4^* = \kappa_{40} + 3, \qquad \kappa_{40} = \frac{\pi}{\sqrt{3}}\mathrm{BFI}^2. \tag{1-6}$$

Based on the contribution from the quasi-resonant four-wave interactions in Eq.(1-6) on wave height, Mori and Janssen (2006) gave the exceeding probability $P(H)$ of wave height H:

$$P(H) = e^{\frac{-H^2}{8}}\left[1 + \frac{\kappa_{40}}{384}(H^4 - 16H^2)\right], \tag{1-7}$$

and exceeding probability $P_m(H_{\max})$ of maximum wave height $H_{\max}$:

$$P_m(H_{\max}) = 1 - \exp\left\{-N_0 e^{\frac{-H_{\max}^2}{8}}\left[1 + \frac{\kappa_{40}}{384}(H_{\max}^4 - 16H_{\max}^2)\right]\right\}, \tag{1-8}$$

where N_0 represents the number of waves in a wave train. Eq. (1-8) is well validated by the kurtosis in wave tank experiment from Mori et al. (2007) and Kashima & Mori (2019). In a two-dimensional (2D) wavefield, Alber and Saffman (1978) discussed the stability of deep-water random waves in 2D space and several studies demonstrated the suppression of instability in directional dispersion (e.g. Waseda et al., 2009; Onorato et al., 2009a; Mori et al., 2011). With the consideration of directional effect, Mori et al. (2011) gave the estimation of maximum κ_{40} with the directional spread σ_θ by asymptotic analysis in Monte Carlo simulation:

$$\kappa_{40} = \frac{\pi}{\sqrt{3}} \mathrm{BFI}^2 \left(\frac{\alpha}{\sigma_\theta} \right), \qquad (1-9)$$

where α is the empirical coefficient.

In the simulation study to generate freak wave numerically, Non-linear Schrödinger (NLS) equation derived by Zakharov (1968) is widely applied since it can reflect the four-wave interaction in wave evolution. Based on the Laplace equation and non-linear boundary conditions, the NLS equation gives the evolution of wave envelope at time and space. The form of the NLS equation varies from different hypotheses and boundary conditions, such as the assumption of bottom topography and surface tension. With the application of the pseudo spectral method and the Fourier transform, surface elevation of wave train can be constructed in a computational fluid dynamics (CFD) model from given the initial conditions.

1.2 Research purpose and outline

Previous research indicates the generation mechanism of freak wave in deep-water, and the numerical simulations have well validated it in related studies. However, the occurrence of the freak wave still exists in shallow water depth even the contribution from modulational instability becomes weak. In this dissertation, we concentrate on the medium and shallow water depth from offshore to onshore, and we intend to investigate the specific impacts from the bottom topography on the modulated wave trains at sea states.

With the strong correlation between the high-order non-linear interactions and the occurrence probability of freak wave, we focus on investigating how the spatial inhomogeneity from the water depth variation and slope angle affects four-wave interaction in the envelope evolution of modulated wave, as the process water wave entering continental shelf from deep sea with mild slope. A numerical evolution model of modulated wave trains is established through modified Non-linear Schrödinger (mNLS) with water depth change and Monte-Carlo simulation. Dimensionless moment kurtosis and skewness are used as indicators for high-order interaction, and wave height distribution is given from the construction of discrete surface elevation. In a 2D wavefield, further development of the model considers the directional dispersion effect on four-wave interaction and the oblique incident wave.

In **Chapter 2**, we introduce the traditional derivation of NLS equation and the third-order

mNLS model for the wave propagating over an uneven bottom that we applied in this study.

In **Chapter 3**, we give the numerical result for mNLS model in the unidirectional (1D) wave trains. Four-wave interaction is given in Eq.(1-3), and we deal with the wave simulation as an initial value problem. Spatial inhomogeneity from the water depth change is reflected in spatial step for different bottom types. With Monte-Carlo simulation from random initial phase information, we discuss the evolution of the nonlinearity of wave trains from the high-order standardized moments of surface elevation, and wave height distribution at different conditions to analysis extreme events.

In **Chapter 4**, we give the numerical result in a 2D wavefield based on the result in **Chapter 3**. Directional dispersion effect is taken into consideration from a directional random wave train, and the comparison between 1D and 2D shows the attenuation of four-wave interaction in a 2D wavefield. Additionally, we consider the effect from the bottom topography from different types of uneven bottom and the oblique incident wave with a small angle of incidence.

A summary of the above results is given in **Chapter 5**.

Chapter 2

Evolution Equations for Modulated Water Waves

2.1 Introduction

In fluid dynamics, the potential flow theory is well applied to describe the spatial and temporal distribution of physical quantity in a flow field. For an irrotational, inviscid and incompressible flow field, the velocity potential satisfies the Laplace equation inside and the boundary conditions on the physical boundaries. For gravity water waves with a free surface, wave train becomes modulated due to the non-linear interactions from the high-order effect. Related discussion about the non-linear modulated wave can be referred to the reviews in Yuen and Lake (1980, 1982), Hammack and Henderson (1993), Dias and Kharif (1999) and Liu (1999).

The Non-linear Schrödinger (NLS) equation is the simplest form in the study of modulated wave trains. Zakharov (1968) firstly derived the NLS equation from the non-linear boundary conditions by Hamiltonian function for narrow spectral bandwidth, which is also called the Zakharov equation. The NLS equation gives the evolution of wave envelope at time and space in the form of a partial differential equation on the third-order. The non-linear term can reflect four-wave interaction to estimate modulational instability of wave train, so the NLS equation is widely used in freak wave study. Davey and Stewartson (1974) gave the derivation of NLS equation in an easy-to-understand way. With the application of the multiple scales method, they discussed the expression of the velocity potential and surface elevation of the Stokes wave in different orders and harmonics. In their study, wave packet is defined as a three-dimensional (3D) problem due to the form of wave surface in stereoscopic space. We can also call it a two-

dimensional (2D) problem since the value of surface elevation on the vertical direction can be determined by the value from the other two dimensions at a certain time (this definition is used in the following content). For the NLS equation in standard form, we can give some particular solutions as the theoretical solutions such as decaying solutions, soliton and breather. (e.g. Benney and Newell, 1967; Segur and Ablowitz, 1976; Hui and Hamilton, 1979). The derivation of the NLS equation in the standard form varies in different ways (e.g. Chu and Mei, 1970; Hasimoto and Ono, 1972; Djordjevic and Redekopp, 1977), as well as the related numerical work (e.g. Lo and Mei, 1985 & 1987).

With different hypotheses and boundary conditions, such as the special case in extreme condition, consideration of surface tension and an ambient current, modified NLS equations have been put up in various forms (e.g. Longuet-Higgins, 1976; Djordjevic and Redekopp, 1977; Dysthe, 1979; Turpin et al., 1983; Dysthe et al., 2003). With the contribution from spatial inhomogeneity on the modulation, Djordjevic and Redekopp (1978) derived a solution for an envelope-hole soliton moving over an uneven bottom and gave a modified NLS equation with slope effect. Variation of the depth in Liu and Dingemans (1989) was divided into different scales, then they gave evolution equations for modulated wave groups over an uneven bottom in different types. If fast varying component is ignored, Liu and Dingemans (1989)'s result for a very mild slope is the same as Djordjevic and Redekopp (1978)'s work.

2.2 Governing equations

With the hypothesis of an irrotational, inviscid and incompressible flow with free water surface, a coordinate system (x, y, z) is established. Plane (x, y) is defined along the quiescent water surface and z is defined vertically upward direction, opposite to the gravity acceleration g. We define the velocity potential Φ and free surface elevation η are functions of space and time t:

$$\Phi = \Phi(x, y, z, t), \eta = \eta(x, y, t). \qquad (2-1)$$

In the entire flow field Φ is a solution of the Laplace equation to satisfy continuity:

$$\nabla^2 \Phi = \frac{\partial^2 \Phi}{\partial x^2} + \frac{\partial^2 \Phi}{\partial y^2} + \frac{\partial^2 \Phi}{\partial z^2} = 0. \qquad (2-2)$$

On the boundary of free surface $z = \eta(x, y, t)$, Φ and η satisfy the kinematic boundary condition (i.e. free surface equation) and the dynamic boundary condition (i.e. Bernoulli equation):

$$\frac{\partial \Phi}{\partial z} = \frac{\partial \eta}{\partial t} + \frac{\partial \Phi}{\partial x}\frac{\partial \eta}{\partial x} + \frac{\partial \Phi}{\partial y}\frac{\partial \eta}{\partial y}, \qquad z = \eta, \qquad (2-3)$$

$$2\frac{\partial \Phi}{\partial t} + 2g\eta + \left(\frac{\partial \Phi}{\partial x}\right)^2 + \left(\frac{\partial \Phi}{\partial y}\right)^2 + \left(\frac{\partial \Phi}{\partial z}\right)^2 = 0, \qquad z = \eta. \qquad (2-4)$$

At the bottom of flow field, Φ satisfies the no-flux boundary along the sea floor. If the water depth h is constant at a flat bottom $z = -h$, Φ satisfies the flat bottom equation:

$$\frac{\partial \Phi}{\partial z} = 0, \qquad z = -h. \qquad (2-5)$$

If we assume the bottom is uneven and water depth varies at $z = -h(x, y)$, Φ satisfies the uneven bottom equation:

$$\frac{\partial \Phi}{\partial z} + \frac{\partial h}{\partial x}\frac{\partial \Phi}{\partial x} + \frac{\partial h}{\partial y}\frac{\partial \Phi}{\partial y} = 0, \qquad z = -h(x, y). \qquad (2-6)$$

Eq. (2-1) to (2-5) consist of the governing equations of the wave evolution on a flat bottom, and for an even bottom we use Eq. (2-6) instead of (2-5).

2.3 Method of multiple scales and solution of envelope

Base on the periodicity of the time and space in the propagation of gravity waves, wave frequency ω and wave number k satisfy the linear dispersion relation:

$$\omega = \sqrt{gk\sigma}, \qquad (2-7)$$

where $\sigma = \tanh kh$. For a medium has no temporal variation, carrier wave frequency $\omega = \omega_0$ is constant, where subscript 0 means linear waves. For a flat bottom with a constant water depth h, carrier wave number $k = k_0$ is also constant as ω; for an uneven bottom, wave number k will be changed because of spatial inhomogeneity due to bottom topography. The change in wave dispersion will also be reflected in the group speed c_g:

$$c_g = \frac{g}{2\omega}[\sigma + kh(1 - \sigma^2)]. \qquad (2-8)$$

In other words, k and c_g are functions of h.

For a weakly non-linear wave train, the modulation parameter comes from the contribution from the small perturbation in high-order harmonic, so we further expand the velocity potential Φ and free surface elevation η into harmonic functions. In this research, we assume the modulation caused by the nonlinearity and the depth variations are in the same order of magnitude referring to Liu and Dingemans (1989). We make this small parameter equal to wave steepness ε, and expand Φ and η in the form of :

$$\Phi(x,y,z,t) = \sum_{n=1}^{\infty} \varepsilon^n \left[\sum_{m=-n}^{n} \Phi_{nm}(x,y,z,t)\, E^m \right], \qquad (2-9)$$

$$\eta(x,y,t) = \sum_{n=1}^{\infty} \varepsilon^n \left[\sum_{m=-n}^{n} \eta_{nm}(x,y,t)\, E^m \right], \qquad (2-10)$$

$$E = \exp[\mathrm{i}(kx - \omega_0 t)], \qquad (2-11)$$

where E represent the harmonic functions, and the complex conjugates part satisfy $\Phi_{n,-m} = \tilde{\Phi}_{nm}$, $\eta_{n,-m} = \tilde{\eta}_{nm}$. We take $n \leq 3$ in the derivation since ε is very small.

With the expansion of Φ and η to the third-order of ε, the method of multiple scales introduced in Davey and Stewartson (1974) is applied to give the solution at different order and harmonic. The details in this process in similar to the Hasimoto and Ono (1972).

2.3.1 Solution of the envelope evolution for a flat bottom

Firstly, we concentrate on the derivation of Φ and η for the wave evolution on a flat bottom. We introduce the variables substitution as follow referring to Davey and Stewartson (1974):

$$\tau_1 = \varepsilon^2 t, \qquad \xi_1 = \varepsilon(x - c_g t), \qquad \zeta = \varepsilon y, \qquad (2-12)$$

which makes $\Phi = \Phi(\tau_1, \xi_1, \zeta, z)$ and $\eta = \eta(\tau_1, \xi_1, \zeta)$. The harmonic $E = 0$ represents the very long wave or wave-induced mean current, and we assume Φ_{10} and Φ_{20} are independent of z, and

$$\frac{\partial \Phi_{30}}{\partial z} = -(z+h)\left(\frac{\partial^2 \Phi_{10}}{\partial \xi_1^2} + \frac{\partial^2 \Phi_{10}}{\partial \zeta^2} \right). \qquad (2-13)$$

Take Eq. (2-9) into Eq. (2-2) and (2-5) to have a multiscale analysis, we get the basic solution of Φ_{nm} at different order and harmonic. We also need to pay attention to the high harmonic terms with the contribution from low harmonic in the non-linear interactions.

At $O(\varepsilon)$, we can get the ordinary differential equation about Φ_{11} from the Laplace equation:

$$\frac{\partial^2 \Phi_{11}}{\partial z^2} - k^2 \Phi_{11} = 0, \tag{2-14}$$

$$\Phi_{11} = A_1' e^{kz} + A_2' e^{-kz}. \tag{2-15}$$

With Eq. (2-5), we can get:

$$\Phi_{11} = A(\tau_1, \xi_1, \zeta) \frac{\cosh k(z+h)}{\cosh kh}, \tag{2-16}$$

where $A(\tau_1, \xi_1, \zeta)$ is an unknown coefficient. We can understand A to represent the envelope of the velocity potential Φ at the first-order and first-harmonic from the perspective of physical meaning.

At $O(\varepsilon^2)$, we can give Φ_{22} and Φ_{21} through the same process:

$$\Phi_{22} = F(\tau_1, \xi_1, \zeta) \frac{\cosh 2k(z+h)}{\cosh 2kh}, \tag{2-17}$$

$$\Phi_{21} = D(\tau_1, \xi_1, \zeta) \frac{\cosh k(z+h)}{\cosh kh} - \mathrm{i} \frac{\partial A}{\partial \xi_1} \frac{1}{\cosh kh} [(z+h)\sinh k(z+h) - h\sigma \cosh(z+h)], \tag{2-18}$$

where $F(\tau_1, \xi_1, \zeta)$ is an unknown coefficient of the envelope of the velocity potential Φ at the second-order and second-harmonic, and $D(\tau_1, \xi_1, \zeta)$ is for the second-order and first-harmonic.

At $O(\varepsilon^3)$, we only give Φ_{31} since the expression from higher harmonic is not required in the following derivation:

$$\begin{aligned}\Phi_{31} = {} & G(\tau_1, \xi_1, \zeta) \frac{\cosh k(z+h)}{\cosh kh} \\ & + \frac{(z+h)\sinh k(z+h) - h\sigma \cosh(z+h)}{2k \cosh kh} \left[2k \left(h\sigma \frac{\partial^2 A}{\partial \xi_1^2} - \mathrm{i} \frac{\partial D}{\partial \xi_1} - \mathrm{i}\varepsilon \frac{\partial A}{\partial \xi_1} \right) - \frac{\partial^2 A}{\partial \zeta^2} \right] \\ & - \frac{[(z+h)^2 - h^2]\cosh k(z+h)}{2\cosh kh} \frac{\partial^2 A}{\partial \xi_1^2},\end{aligned} \tag{2-19}$$

where $G(\tau_1, \xi_1, \zeta)$ is an unknown coefficient of the envelope Φ at the third-order and first-harmonic.

To determine the unknown coefficients in the expression, we take the result of Φ in Eq .(2-16) to (2-19) into Eq .(2-3) and Eq .(2-4). With the expansion of η from Eq .(2-10), we take the Taylor-expansion at the equilibrium position $z = 0$. The free surface equation in Eq .(2-3) can be written as:

$$0=\frac{\partial\eta}{\partial t}+\left(-\frac{\partial\Phi}{\partial z}+\frac{\partial\Phi}{\partial x}\frac{\partial\eta}{\partial x}+\frac{\partial\Phi}{\partial y}\frac{\partial\eta}{\partial y}\right)\Big|_{z=\eta}$$
$$=\frac{\partial\eta}{\partial t}+\left(-\frac{\partial\Phi}{\partial z}+\frac{\partial\Phi}{\partial x}\frac{\partial\eta}{\partial x}+\frac{\partial\Phi}{\partial y}\frac{\partial\eta}{\partial y}\right)\Big|_{z=0}+\eta\left[\frac{\partial}{\partial z}\left(-\frac{\partial\Phi}{\partial z}+\frac{\partial\Phi}{\partial x}\frac{\partial\eta}{\partial x}+\frac{\partial\Phi}{\partial y}\frac{\partial\eta}{\partial y}\right)\Big|_{z=0}\right]$$
$$+\frac{1}{2}\eta^2\left[\frac{\partial^2}{\partial z^2}\left(-\frac{\partial\Phi}{\partial z}+\frac{\partial\Phi}{\partial x}\frac{\partial\eta}{\partial x}+\frac{\partial\Phi}{\partial y}\frac{\partial\eta}{\partial y}\right)\Big|_{z=0}\right]+\cdots, \qquad (2-20)$$

and the Bernoulli equation in Eq .(2-4) can be written as:

$$0=2g\eta+\left[2\frac{\partial\Phi}{\partial t}+\left(\frac{\partial\Phi}{\partial x}\right)^2+\left(\frac{\partial\Phi}{\partial y}\right)^2+\left(\frac{\partial\Phi}{\partial z}\right)^2\right]\Big|_{z=\eta}$$

$$=2g\eta+\left[2\frac{\partial\Phi}{\partial t}+\left(\frac{\partial\Phi}{\partial x}\right)^2+\left(\frac{\partial\Phi}{\partial y}\right)^2+\left(\frac{\partial\Phi}{\partial z}\right)^2\right]\Big|_{z=0}$$
$$+\eta\left\{\frac{\partial}{\partial z}\left[2\frac{\partial\Phi}{\partial t}+\left(\frac{\partial\Phi}{\partial x}\right)^2+\left(\frac{\partial\Phi}{\partial y}\right)^2+\left(\frac{\partial\Phi}{\partial z}\right)^2\right]\Big|_{z=0}\right\}$$
$$+\frac{1}{2}\eta^2\left\{\frac{\partial^2}{\partial z^2}\left[2\frac{\partial\Phi}{\partial t}+\left(\frac{\partial\Phi}{\partial x}\right)^2+\left(\frac{\partial\Phi}{\partial y}\right)^2+\left(\frac{\partial\Phi}{\partial z}\right)^2\right]\Big|_{z=0}\right\}+\cdots. \qquad (2-21)$$

At $O(\varepsilon)$, the mean surface elevation $\eta_{10}=0$ and we get the surface elevation on first-harmonic:

$$g\eta_{11}=\mathrm{i}\omega_0 A. \qquad (2-22)$$

At $O(\varepsilon^2)$, we can give:

$$g\eta_{20}=c_g\frac{\partial\phi_{10}}{\partial\xi_1}-k^2|A|^2(1-\sigma^2), \qquad (2-23)$$
$$g\eta_{21}=c_g\frac{\partial A}{\partial\xi_1}+\mathrm{i}\omega_0 D, \qquad (2-24)$$
$$g\eta_{22}=-\frac{k^2A^2}{2\sigma^2}(3-\sigma^2),\qquad \omega_0 F=\frac{3\mathrm{i}k^2A^2}{4\sigma^2}(1-\sigma^4). \qquad (2-25)$$

At $O(\varepsilon^3)$, we give the final evolution equation of A by a equation set from E^0 and E respectively in the same form of Davey and Stewartson (1974):

$$(gh-c_g^2)\frac{\partial^2\phi_{10}}{\partial\xi_1^2}+gh\frac{\partial^2\phi_{10}}{\partial\zeta^2}=-k^2[c_g(1-\sigma^2)+2c_p]\frac{\partial|A|^2}{\partial\xi_1},\qquad c_p=\frac{\omega_0}{k}, \qquad (2-26)$$
$$\mathrm{i}\frac{\partial A}{\partial\tau_1}+\beta_x^1\frac{\partial^2A}{\partial\xi_1^2}+\beta_y^1\frac{\partial^2A}{\partial\zeta^2}=\beta_n^1|A|^2A+\beta_f^1A\frac{\partial\phi_{10}}{\partial\xi_1}, \qquad (2-27)$$

where

$$\beta_x^1=\frac{1}{2}\frac{\partial^2\omega}{\partial k^2}\equiv-\frac{1}{2\omega_0}[c_g^2-gh(1-\sigma^2)(1-kh\sigma)], \qquad (2-28)$$
$$\beta_y^1=\frac{1}{2k}\frac{\partial\omega}{\partial k}\equiv\frac{c_g}{2k}, \qquad (2-29)$$

$$\beta_n^1 = \frac{k^4}{4\omega_0}(9\sigma^{-2} - 12 + 13\sigma^2 - 2\sigma^4), \qquad (2-30)$$

$$\beta_f^1 = \frac{k^2}{2\omega_0}[2c_p + c_g(1-\sigma^2)]. \qquad (2-31)$$

Eq. (2-26) and (2-27) consist of the evolution equation of the envelope of velocity potential at the first-harmonic on a flat bottom. Eq. (2-26) is a Poisson-type equation for forcing mean flow, and the equation in the same form with Eq. (2-27) is known as the NLS equation for the weak non-linear wave evolution, and the non-linear term $\beta_n^1|A|^2A$ represents the high-order interaction from different harmonics. Based on different definitions of A, the expression of β_n^1 and β_f^1 are different (Liu, 1999). If A represents the envelope of surface elevation, Eq. (2-30) and Eq. (2-31) become:

$$\beta_n^{1*} = \frac{g^2k^4}{4\omega_0^3}(9\sigma^{-2} - 12 + 13\sigma^2 - 2\sigma^4), \qquad (2-32)$$

$$\beta_f^{1*} = \frac{gk^2}{2\omega_0^2}[2c_p + c_g(1-\sigma^2)]. \qquad (2-33)$$

2.3.2 Solution of the envelope evolution for an uneven bottom with mild slope

If we consider the contribution from spatial inhomogeneity on the modulational instability of wave trains, a modified NLS equation can be derived in a NLS-like form. The governing equations for an uneven bottom is almost the same with flat bottom case, but the no-flux boundary on the bottom requires the application of Eq.(2-6) instead of (2-5).

To simplify the problem, we suppose the water depth h varies slowly. Additionally, we want to concentrate on the variation of depth on the wave propagating direction, so we assume the magnitude of the gradient of depth change satisfies $h'(x)\sim O(\varepsilon^2)$ and $h'(y)\sim O(\varepsilon^3)$. Considering the expansion form in Eq. (2-9) and (2-10), the effect from bottom topography change only reflects in the third-order $O(\varepsilon^3)$ and $h'(y)\sim O(\varepsilon^3)$ is equivalent to $h'(y) = 0$. As for the dispersion relation between wave number and frequency, the carrier $\omega = \omega_0$ is still constant since there is no temporal variation, but carrier wave number k changes. Based on the above inference, we can get $k = k(x)$ and $c_g = c_g(x)$ on the principal wave direction, and the harmonic term is in the form as:

$$E = \exp\left\{\mathrm{i}\left[\int^x k(x)dx - \omega_0 t\right]\right\}, \qquad (2-34)$$

Moreover, we expect to reflect the variation of h in wave evolution process explicitly, so we introduce a different variable substitution of t and x referring to Djordjevic and Redekopp (1978):

$$\tau_2 = \varepsilon\left[\int^x \frac{dx}{c_g(x)} - t\right], \qquad \xi_2 = \varepsilon^2 x, \qquad \zeta = \varepsilon y. \tag{2-35}$$

Through a similar derivation process for the flat bottom in **2.3.1**, we give the solution of Φ and η at different order and harmonic.

At $O(\varepsilon)$:

$$\Phi_{11} = A(\tau_2,\xi_2,\zeta)\frac{\cosh k(z+h)}{\cosh kh}, \tag{2-36}$$

$$g\eta_{11} = \mathrm{i}\omega_0 A. \tag{2-37}$$

At $O(\varepsilon^2)$:

$$\Phi_{22} = F(\tau_2,\xi_2,\zeta)\frac{\cosh 2k(z+h)}{\cosh 2kh}, \tag{2-38}$$

$$\Phi_{21} = D(\tau_2,\xi_2,\zeta)\frac{\cosh k(z+h)}{\cosh kh} - \mathrm{i}\frac{\partial A}{\partial \tau_2}\frac{1}{c_g \cosh kh}[(z+h)\sinh k(z+h) - h\sigma \cosh k(z+h)] \tag{2-39}$$

$$g\eta_{20} = \frac{\partial \phi_{10}}{\partial \tau_2} - k^2|A|^2(1-\sigma^2), \tag{2-40}$$

$$g\eta_{21} = \frac{\partial A}{\partial \tau_2} + \mathrm{i}\omega_0 D, \tag{2-41}$$

$$g\eta_{22} = -\frac{k^2A^2}{2\sigma^2}(3-\sigma^2), \qquad \omega_0 F = \frac{3\mathrm{i}k^2A^2}{4\sigma^2}(1-\sigma^4). \tag{2-42}$$

At $O(\varepsilon^3)$:

$$\frac{\partial \Phi_{30}}{\partial z} = -(z+h)\left(\frac{\partial^2 \Phi_{10}}{\partial \tau_2^2}\frac{1}{c_g^2} + \frac{\partial^2 \Phi_{10}}{\partial \zeta^2}\right), \tag{2-43}$$

$$\begin{aligned}\Phi_{31} = {} & G(\tau_2,\xi_2,\zeta)\frac{\cosh k(z+h)}{\cosh kh} \\ & -\frac{\mathrm{i}}{2\cosh kh}\left[2k\frac{\mathrm{d}(h)}{\mathrm{d}\xi_2}A + \left(k'A - \frac{\mathrm{i}}{c_g^2}\frac{\partial^2 A}{\partial \tau_2^2}\right)(z+h)\right](z+h)\cosh k(z+h) \\ & +\frac{\mathrm{i}}{\cosh kh}\left[\sigma\frac{\mathrm{d}(kh)}{\mathrm{d}\xi_2}A - \frac{\partial A}{\partial \xi_2} - \frac{\mathrm{i}h\sigma}{c_g^2}\frac{\partial^2 A}{\partial \tau_2^2} - \frac{1}{c_g}\frac{\partial D}{\partial \tau_2} + \mathrm{i}\frac{1}{2k}\frac{\partial^2 A}{\partial \zeta^2}\right](z+h)\sinh k(z+h),\end{aligned} \tag{2-44}$$

where A, D, F, G are unknown functions of τ_2, ξ_2, ζ. At $O(\varepsilon)$ and $O(\varepsilon^2)$, the difference between **2.3.1** and **2.3.2** only comes from the different form of variable substitution. At $O(\varepsilon^3)$, the effect of depth change shows up and we can give the evolution equation of A in a similar equation set:

$$\frac{\partial^2\phi_{10}}{\partial\tau_2^2}\left(1-\frac{gh}{c_g^2}\right)-gh\frac{\partial^2\phi_{10}}{\partial\zeta^2}=k^2\left[(1-\sigma^2)+2\frac{c_p}{c_g}\right]\frac{\partial|A|^2}{\partial\tau_2}, \qquad (2-45)$$

$$\mathrm{i}\beta_h^2 A+\mathrm{i}\frac{\partial A}{\partial\xi_2}+\beta_t^2\frac{\partial^2 A}{\partial\tau_2^2}+\beta_y^2\frac{\partial^2 A}{\partial\zeta^2}=\beta_n^2|A|^2A+\beta_f^2 A\frac{\partial\phi_{10}}{\partial\tau_2}, \qquad (2-46)$$

where

$$\beta_h^2=\frac{(1-\sigma^2)(1-kh\sigma)}{\sigma+kh(1-\sigma^2)}\frac{d(kh)}{d\xi_2}=\frac{1}{2c_g}\frac{\mathrm{d}(c_g)}{\mathrm{d}\xi_2}, \qquad (2-47)$$

$$\beta_t^2=-\frac{1}{2\omega_0 c_g}\left[1-\frac{gh}{c_g^2}(1-\sigma^2)(1-kh\sigma)\right], \qquad (2-48)$$

$$\beta_y^2=\beta_y^1=\frac{1}{2k}\frac{\partial\omega}{\partial k}\equiv\frac{c_g}{2k}, \qquad (2-49)$$

$$\beta_n^2=\beta_n^1=\frac{k^4}{4\omega_0}(9\sigma^{-2}-12+13\sigma^2-2\sigma^4), \qquad (2-50)$$

$$\beta_f^2=\beta_f^1=\frac{k^2}{2\omega_0}[2c_p+c_g(1-\sigma^2)]. \qquad (2-51)$$

β_h^2 reflects the contribution from the variation of bottom topography, and it is proportional to the gradient of water depth change. When $\beta_h^2=0$, the modified equation set is equivalent to the flat bottom equation in **2.3.1**. From Eq. (2-47), the value of β_h^2 can be positive or negative depending on the kh, which implies the effect from bottom topography change on the non-linear interaction may convert at different water depth or bottom shape.

For the case that slope is not very mild and $h'(x)$~$O(\varepsilon)$, Liu and Dingemans (1989) also gave the evolution equation of wave envelope. The equation set for a unidirectional wave train in the form of:

$$\mathrm{i}\beta_h' A+\mathrm{i}\frac{\partial A}{\partial\xi}+\beta_t'\frac{\partial^2 A}{\partial\tau^2}=\beta_n'|A|^2A+\beta_1\frac{\partial\phi_{10}}{\partial x}A+\beta_2\frac{\partial\phi_{10}}{\partial t}A, \qquad (2-52)$$

$$\frac{\partial^2\phi_{10}}{\partial t^2}-\frac{\partial}{\partial x}\left(gh\frac{\partial\phi_{10}}{\partial x}\right)=\frac{g^2}{2\omega_0}\frac{\partial}{\partial x}(k|A|^2)-\frac{\omega_0^2}{4\sinh^2 kh}\frac{\partial|A|^2}{\partial t}, \qquad (2-53)$$

where $\beta_\mu', \beta_\lambda', \beta_v', \beta_1, \beta_2$ are coefficients consist of σ, k, ω_0, h and c_g. We don't apply Eq. (2-52) and (2-53) in this study, because the terms with ϕ_{10} make it difficult to give the solution even in a numerical model.

2.4 Real wave surface elevation

In **2.3**, we discuss the evolution equation of envelope in the NLS and NLS-like equation, and the expression can be different based on the definition of amplitude A. To give the real

wave surface elevation, usually we define A is the envelope of surface elevation η. Liu and Dingemans (1989) defined $\eta_{11} = \frac{1}{2}A$ as the basic solution in the first order, and considered the contribution from the second-order first-harmonic D to the surface elevation. Under this consideration, we can denote $\bar{A} = A + \varepsilon D$ instead of A including the second-order effects. Besides, the term about $\partial\phi_{10}$ is unknown in the solving of NLS equation, which increases the difficulty to determine A. Referring to Davey & Stewartson (1974) and Djordjevic & Redekopp (1978), Eq. (2-45) and Eq. (2-46) can be re-expressed in one equation:

$$\mathrm{i}\beta_h\bar{A} + \mathrm{i}\frac{\partial\bar{A}}{\partial\xi_2} + \beta_t\frac{\partial^2\bar{A}}{\partial\tau_2^2} + \beta_y\frac{\partial^2\bar{A}}{\partial\zeta} = \beta_n\left|\bar{A}\right|^2\bar{A} + \beta_\kappa\bar{A}Q_0, \tag{2-54}$$

where $\beta_h = \beta_h^2,\ \beta_t = \beta_t^2,\ \beta_y = \beta_y^2$,

$$\beta_n = k^2\omega_0\left[\frac{1}{16}(9 - 10\sigma^2 + 9\sigma^4) - \frac{1}{2\sinh^2 2kh}\right] + \left[\frac{\omega_0^3}{g}\frac{1}{2g}(\sigma^2 - 1) + \frac{k}{c_g}\right]\left(\frac{c_g^2}{c_g^2 - gh}\right)\left[\frac{g^2k}{2\omega_0 c_g} + \frac{\omega_0^2}{4\sinh(kh)^2}\right], \tag{2-55}$$

$$\beta_\kappa = \frac{k^2}{2\sigma}\frac{c_p}{c_g}\left[\frac{2c_p}{c_g} + (1 - \sigma^2)\right]. \tag{2-56}$$

Q_0 only effect phase in the result so we can regard Q_0 = 0. Strictly speaking, removing the last term in Eq. (2-54) requires a special transformation about envelope A. In this study, we construct wave surface elevation with random phase to conduct the Monte Carlo simulation as following chapters, so the precise value of Q_0 is not essential for the result we concentrate on.

Eq. (2-54) can be solved numerically to give the wave envelop in time and space. Based on the periodicity in wavefield, we give the real surface elevation considering the second-order and second-harmonic:

$$\eta(x, y, t) = \varepsilon E\eta_{11} + \varepsilon^2(E\eta_{21} + E^2\eta_{22}). \tag{2-57}$$

It can be expressed in the form of $\bar{A}$:

$$\eta(x, y, t) = \varepsilon\mathrm{Re}\left[\frac{1}{2}\bar{A}\exp\big(\mathrm{i}(k(x)x - \omega_0 t)\big)\right] + \varepsilon^2\mathrm{Re}\left[\frac{k\cosh kh}{8\sinh^3 kh}(2\cosh^2 kh + 1)\bar{A}^2\exp\big(2\mathrm{i}(k(x)x - \omega_0 t)\big)\right]. \tag{2-58}$$

Chapter 3

Numerical Model of Unidirectional Modulated Wave Train

3.1 Introduction

From the observation record of the World Ocean and the coast in Nikolkina and Didenkulova (2011), freak wave not only occurs in deep-water but also finite and shallow water. In the process water wave entering the continental shelf from deep sea with a slope, wave evolution will be influenced by the water depth changing. Benjamin(1967) indicated the effect of modulational instability on the wave train has a critical water depth at kh = 1.363. When kh <1.363, the modulational instability becomes weak and the occurrence of extreme value in wave train will significantly decrease. The evolution of modulated wave train over an uneven bottom can also refer to Peregrine (1983), Turpin and Mei (1983), Mei and Benmoussa (1984), Janssen et al. (2003).

In the numerical simulation, kurtosis and skewness of wave train are significantly affected by changes in water depth from Zeng and Trulsen (2012)'s study in Monte Carlo simulation through 1-D modified NLS equation. In deep and finite water, kurtosis and skewness monotonically decline as water depth decreasing. However, from the numerical simulation and physical experiments in shallow water, the slope of bottom topography brings about a rebounding process. From Kashima and Mori (2019) and Trulsen et al. (2020), kurtosis and skewness reach maximum value around the end of the slope region, which indicates the nonlinearity from shoaling effect increases wave train instability. Considering corresponding performance in wave height distribution, the slope angle of bottom topography may play an

important role for the occurrence probability of extreme value in the shallow water.

In this chapter, we concentrate on the numerical solution of mNLS equation for an uneven bottom. We expect to simulate the evolution of wave envelope, and study the effect from spatial inhomogeneity on the modulational instability in wave trains. To get rid of the directional dispersion effect on four-wave interaction, we set up a simple numerical model for unidirectional wave trains, and collect surface elevation in the wavefield of one-dimensional space-time (1D+T). We apply Monte Carlo simulation and pseudo spectral method in the numerical model, and consider the wave shoaling in different types of bottom topography shape.

3.2 Methodology

3.2.1 1D mNLS equation for an uneven bottom

Based on the theoretical result in **Chapter 2**, we apply the mNLS equation for the evolution of wave envelope over an uneven bottom with mild slope. A flow field with unidirectional incident wave trains can be regarded as an 1-D problem, and the coordinate system (x, z) is defined with origin O at quiescent water surface as shown in **Figure 3.1.** The x is defined along the quiescent water surface and z is defined vertically upward direction,

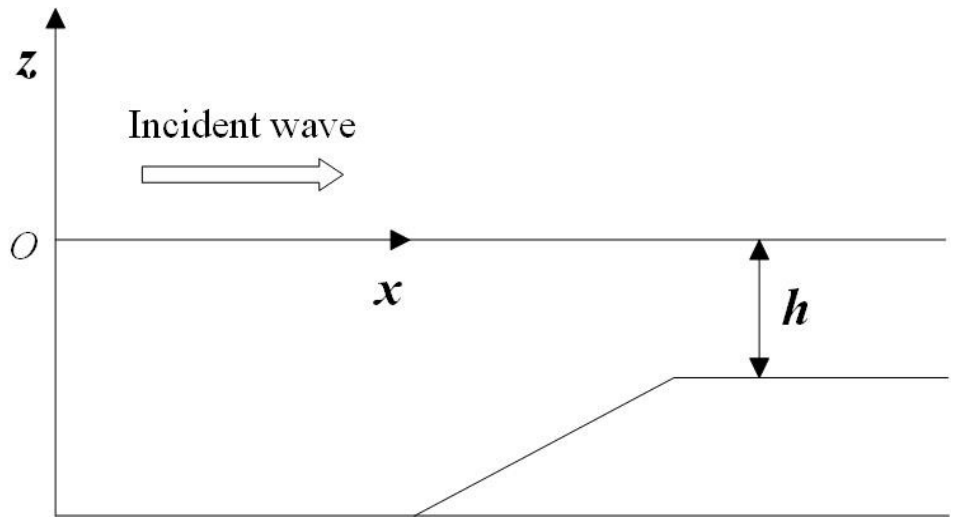

Figure 3.1 Sketch of coordinate with sloping bottom

opposite to gravity acceleration g. As previous assumption, the flow is irrotational, inviscid and incompressible with free surface, and potential theory is applied to give wave velocity potential $\Phi = \Phi(x,z,t)$ and free surface elevation $\eta = \eta(x,t)$. The bottom $z = -h(x)$ varies in the direction of propagation, and it can be divided into three districts: flat bottom in deep-water; sloping region with a constant slope angle; flat bottom in shallow water.

In the entire flow field Φ and η satisfy Eq. (2-1) to (2-4) and Eq. (2-6), and they can be simplified with omission of variation on y:

$$\nabla^2\Phi = \frac{\partial^2\Phi}{\partial x^2} + \frac{\partial^2\Phi}{\partial z^2} = 0, \tag{3-1}$$

$$\frac{\partial\Phi}{\partial z} + \frac{\partial h}{\partial x}\frac{\partial\Phi}{\partial x} = 0, \qquad z = -h(x), \tag{3-2}$$

$$\frac{\partial\Phi}{\partial z} = \frac{\partial\eta}{\partial t} + \frac{\partial\Phi}{\partial x}\frac{\partial\eta}{\partial x}, \qquad z = \eta, \tag{3-3}$$

$$2\frac{\partial\Phi}{\partial t} + 2g\eta + \left(\frac{\partial\Phi}{\partial x}\right)^2 + \left(\frac{\partial\Phi}{\partial z}\right)^2 = 0, \qquad z = \eta. \tag{3-4}$$

Based on the method of multiple scale and the dispersion relation in Eq. (2-7), Φ and η can be expanded into:

$$\Phi(x,z,t) = \sum_{n=1}^{\infty}\varepsilon^n\left[\sum_{m=-n}^{n}\Phi_{nm}(x,z,t)\,E^m\right], \tag{3-5}$$

$$\eta(x,t) = \sum_{n=1}^{\infty}\varepsilon^n\left[\sum_{m=-n}^{n}\eta_{nm}(x,t)\,E^m\right], \tag{3-6}$$

where ε is small constant equal to wave steepness and $E = \exp\{\mathrm{i}[\int^x k(x)dx - \omega t]\}$ represents harmonic function. n, m are integers and the complex conjugate part in the form of $\phi_{n,-m} = \tilde{\phi}_{nm}$, $\eta_{n,-m} = \tilde{\eta}_{nm}$, respectively.

To simplify the problem, we suppose the water depth h varies slowly with the wave propagating direction in the same order to wave steepness, $h'(x) = O(\varepsilon^2)$. We concentrate on the effect from topography change, so the variation of h should be reflected in solving process explicitly. Therefore, we introduce the variable transfer referring to Djordjevic and Redekopp (1978) as **Chapter 2**:

$$\tau = \varepsilon\left[\int^x \frac{dx}{c_g} - t\right], \qquad \xi = \varepsilon^2 x, \tag{3-7}$$

$$c_g = \frac{g}{2\omega_0}[\sigma + kh(1-\sigma^2)], \tag{3-8}$$

where c_g is group velocity. τ and ξ slowly vary on time and space, respectively. Substituting Eq.(3-5), (3-6) into (3-1) to (3-4), we can give the expression of Φ and η in the form of amplitude A of first harmonic in the first-order, which is an unknown complex. We here denote $\bar{A} = A + \varepsilon D$ instead of A including the second-order effects, where D is amplitude of first harmonic in second-order. Finally, the evolution equation of $\bar{A}$ is in following form:

$$\mathrm{i}\beta_h \bar{A} + \mathrm{i}\frac{\partial \bar{A}}{\partial \xi} + \beta_t \frac{\partial^2 \bar{A}}{\partial \tau^2} = \beta_n \left|\bar{A}\right|^2 \bar{A}, \tag{3-9}$$

where

$$\beta_h = \frac{(1-\sigma^2)(1-kh\sigma)}{\sigma + kh(1-\sigma^2)} \frac{d(kh)}{d\xi} = \frac{1}{2c_g} \frac{\mathrm{d}(c_g)}{\mathrm{d}\xi}, \tag{3-10}$$

$$\beta_t = -\frac{1}{2\omega_0 c_g} \left[1 - \frac{gh}{c_g^2}(1-\sigma^2)(1-kh\sigma)\right], \tag{3-11}$$

$$\begin{aligned}\beta_n = k^2\omega_0 &\left[\frac{1}{16}(9 - 10\sigma^2 + 9\sigma^4) - \frac{1}{2\sinh^2 2kh}\right] \\ &+ \left[\frac{\omega_0^3}{g}\frac{1}{2g}(\sigma^2 - 1) + \frac{k}{c_g}\right]\left(\frac{c_g^2}{c_g^2 - gh}\right)\left[\frac{g^2 k}{2\omega_0 c_g} + \frac{\omega_0^2}{4\sinh(kh)^2}\right].\end{aligned} \tag{3-12}$$

3.2.2 Numerical solution

Eq.(3-9) is in the form of partial differential equation and needed to be rewrite into an ordinary differential equation to be solved numerically. We assume the boundary is periodic in time following Zeng and Trulsen (2012), then Fourier transform can be applied to simply the dispersion term in time, and Eq.(3-9) becomes:

$$\frac{\mathrm{d}\bar{A}}{\mathrm{d}\xi} = -\mathrm{i}\beta_n \left|\bar{A}\right|^2 \bar{A} - \mathrm{i}\omega_\tau^2 \beta_t \bar{A} - \beta_h \bar{A} = f(\xi, \bar{A}), \tag{3-13}$$

where ω_τ comes from the Fourier transform about τ:

$$\hat{A}(\xi, \omega_\tau) = F\left[\bar{A}(\xi, \tau)\right]. \tag{3-14}$$

The fourth-order Runge-Kutta method is applied to solving Eq.(3-13) in the spatial evolution. On the step $n+1$, the solution of $\bar{A}_{n+1}$ can be derived from $\bar{A}_n$ on the last step n:

$$\bar{A}_{n+1} = \bar{A}_n + \frac{\mathrm{d}\xi_i}{6}(l_1 + l_2 + l_3 + l_4), \tag{3-15}$$

where $\mathrm{d}\xi_i$ is the calculation resolution on the spatial direction, and

$$l_1 = f(\xi_n, \bar{A}_n), \tag{3-16}$$

$$l_2 = f\left(\xi_n + \frac{\mathrm{d}\xi_i}{2}, \bar{A}_n + \frac{\mathrm{d}\xi_i}{2} l_1\right), \tag{3-17}$$

$$l_3 = f\left(\xi_n + \frac{\mathrm{d}\xi_i}{2}, \bar{A}_n + \frac{\mathrm{d}\xi_i}{2} l_2\right), \tag{3-18}$$

$$l_4 = f(\xi_n + \mathrm{d}\xi_i, \bar{A}_n + \mathrm{d}\xi_i l_3). \tag{3-19}$$

In this way, we deal with the solution of wave envelope $\bar{A}$ of Eq. (3-9) as an initial value problem moving from $\xi = \xi_0$. To give the initial condition, we suppose the Fourier amplitudes $\hat{A}_0(\xi_0, \omega_\tau)$ satisfy the initially Gaussian spectrum with randomized phase information:

$$\hat{A}_0(\xi_0, \omega_\tau) = a\sqrt{\frac{1}{\sqrt{2\pi}\sigma_\omega}} \exp\left(-\frac{(\omega_\tau - \omega_0)^2}{4\sigma_\omega^2} + \mathrm{i}\psi\right), \tag{3-20}$$

Where a represents amplitude scale, σ_ω is spectral bandwidth, ψ represents phase and uniformly distributes at $[0,2\pi]$. Initial BFI value is given by Eq. (1-3), and $\sigma_s = \sigma_\omega/\omega_0$ for dimensionless. In each step of spatial evolution, an array of amplitude $\bar{A}$ in time series will be decided, then free surface elevation η can be given in the second-order as Eq. (2-58). The process in generating the surface elevation from the amplitude varies due to different precision or hypotheses. Eq.(2-58) consists of free surface elevation of amplitude from the first-order to second-order and second harmonic. We integrate Eq.(2-58) from the offshore to onshore assuming periodic boundary condition in time. This is transverse process compared with ordinal treatment of the spectral wave modeling.

For a group of wave train, the distribution of surface elevation η is very important in extreme wave study. In the linear random wave train (i.e. Rayleigh distribution), probability density function of maximum surface elevation $\eta_{\max}$ is only decided by the number of sample, which can be estimated by the zero-up-crossing number N_0 in random wavefield. For narrowband wave trains, maximum wave height $H_{\max}$ usually is simply defined by twice maximum $\eta_{\max}$. From Mori and Janssen (2006), distribution of $H_{\max}$ is related to N_0 and kurtosis μ_4 by the fourth-order cumulant κ_{40} in Eq. (1-8). Therefore, our numerical work concentrate on the statistical parameters and spectrum shape of irregular wave. With a large ensemble size, the surface elevation at same stage will be generally closed to a zero-mean strict-sense stationary process, and its statistical parameters such as μ_4 only change with the initial

condition and spatial inhomogeneity in this study. It can also be applied in wave generation in laboratory to obtain irregular wave trains with required characteristics, e.g. Kashima and Mori (2019).

In the wave height analysis from the zero-up-cross method, frequency spectrum peakedness Q_p in Eq.(3-21) proposed by Goda (1970) can also be used for the measure of frequency dispersion:

$$Q_p = \frac{2\int_0^\infty fS(f)^2 df}{[\int_0^\infty S(f)df]^2}, \qquad (3-21)$$

where $S(f)$ is the frequency spectrum of waves, f represent frequency. The definition of Q_p is similar to the spectral bandwidth, but weighted on the share around peak frequency. In wave height statistic from zero-up-cross method, Q_p has a positive correlation with the maximum wave height distribution if we consider the high-order nonlinearity.

In the realization process, Mei and Benmoussa (1984) introduced a normalization to make all parameters become dimensionless. We apply a different normalization only for the variable $(\bar{A}, \xi, \omega_\tau, \tau)$ in programing as following:

$$A' = \frac{2\pi}{L_0}\bar{A}, \qquad \xi' = \frac{2\pi}{L_0}\xi, \qquad \omega' = \varepsilon\frac{L_T}{2\pi}\omega_\tau, \qquad \tau' = \frac{2\pi}{\varepsilon L_T}\tau, \qquad (3-22)$$

where L_T is the total time length at each step, L_0 is the initial wave length.

3.2.3 Model setup

For a narrowband wave train, we start our simulation from wave energy spectral in Gaussian shape by Eq.(3-20) with carrier frequency ω = 2.5s^{-1}, time length $L_T = 40T_0$, where T_0 is wave period. The initial shape of energy spectral is decided by value of BFI in Eq.(1-3). **Figure 3.2** gives the absolute Fourier Amplitude at BFI = 1, 0.75, 0.5, 0.25, where the wave steepness $\varepsilon = ka$ constantly at 0.1, and dimensionless spectral bandwidth σ_s varies from 0.141, 0.189, 0.283, 0.567, respectively. **Figure 3.2** shows that the larger BFI gives concentrated wave energy on the carrier wave frequency. This effect can be reflected in wave surface in time series. $\hat{A}_0$ in the initial condition from Eq. (3-20) consists of real and imaginary part, so $\bar{A}$ in spatial step is also complex. **Figure 3.3** gives the numerical value about the

evolution of real and imaginary part of $\bar{A}$ in time series at different spatial stages from a single sample at a constant water depth $kh = 7$, where we can see the contribution from real and imaginary part is at the same level but the their envelope don't coincide. We construct the surface elevation η at each step in this model from $\bar{A}$ by Eq. (2-58). **Figure 3.4** indicates the details of surface elevation η at initial point $\xi = \xi_0(x = x_0)$, from different spectra in **Figure 3.2** through the inverse Fourier transform as function of dimensionless time t/T_0. The wave train becomes more regular and the coherent wave period can be more easily distinguished in wave train with larger BFI. η consists of different composition, and **Figure 3.5** gives corresponding η to the $\bar{A}$ in **Figure 3.3** at different orders. Compared with the first-order $\eta(\varepsilon)$, the contribution from second-order term $\eta(\varepsilon^2)$ is very small, but $\eta(\varepsilon^2)$ significantly increases when extreme value occurs.

In Eq.(3-20) the wave phase ψ is set to be random at $[0,2\pi]$, which is able to give different initial wave trains for given BFI. From groups of wave data at different initial conditions, we utilize Monte Carlo simulation (i.e. random phase approximation) to estimate the ensemble averaged non-linear wave characteristics. To check the convergence of result in this model, we give **Figure 3.6** and **Figure 3.7** to show the mean value and standard deviation of kurtosis μ_4 with different ensemble size M. As the M increases, mean value of μ_4 gradually converges. In the numerical NLS model, the wave surface requires a distance from the initial point to become steady and usually it is about $10\sim15L_0$. From **Figure 3.6** and **Figure 3.7**, the result at $x \geq 15L_0$ becomes sufficiently convergent when $M \geq 250$, and we apply ensemble size M = 300 in the following result.

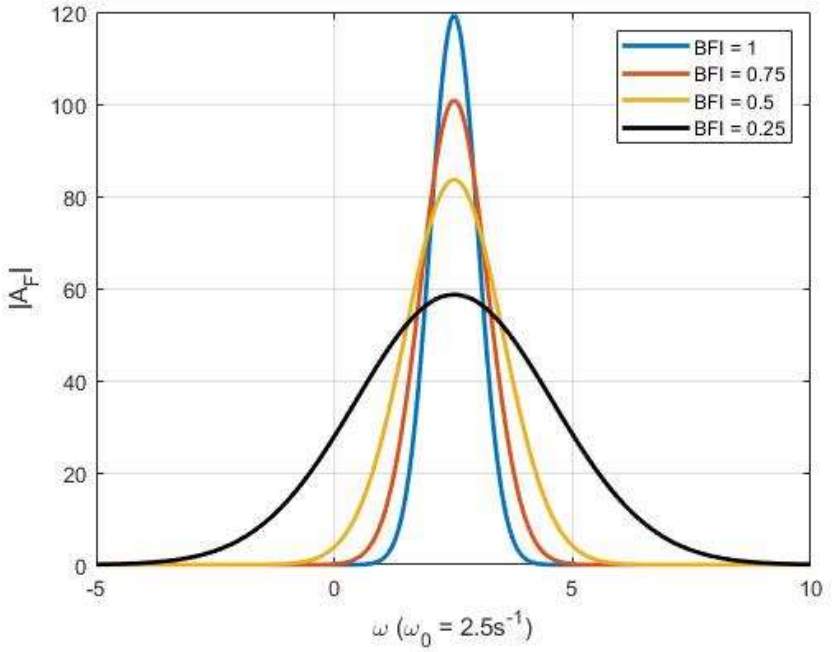

Figure 3.2 Fourier Amplitude from different initial BFI when $\varepsilon = 0.1$, $\sigma_s = 0.141, 0.189, 0.283, 0.567$

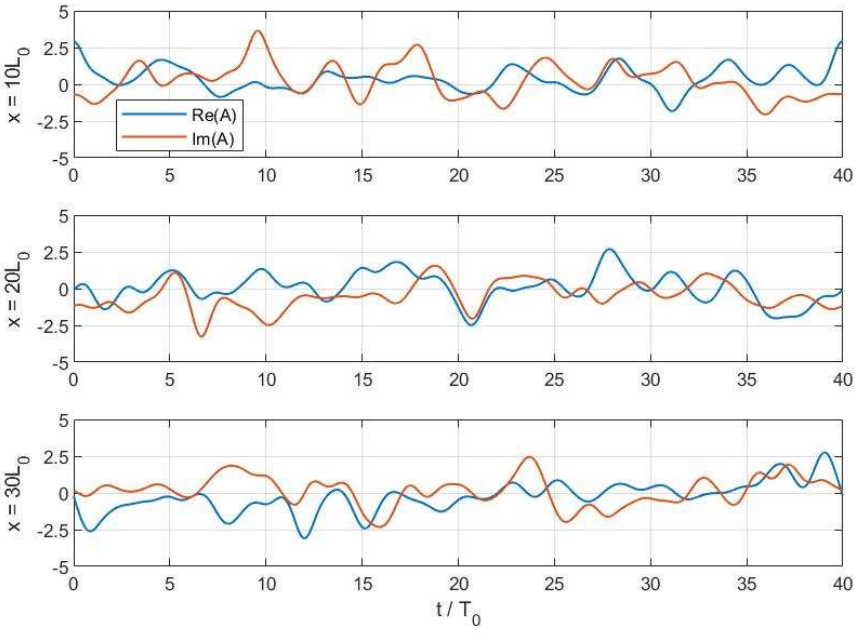

Figure 3.3 A sample of real and imaginary part of wave amplitude in envelope in time series from initial BFI = 0.75 at $x = 10L_0, 20L_0, 30L_0$ when $\varepsilon = 0.1$, $kh = 7$

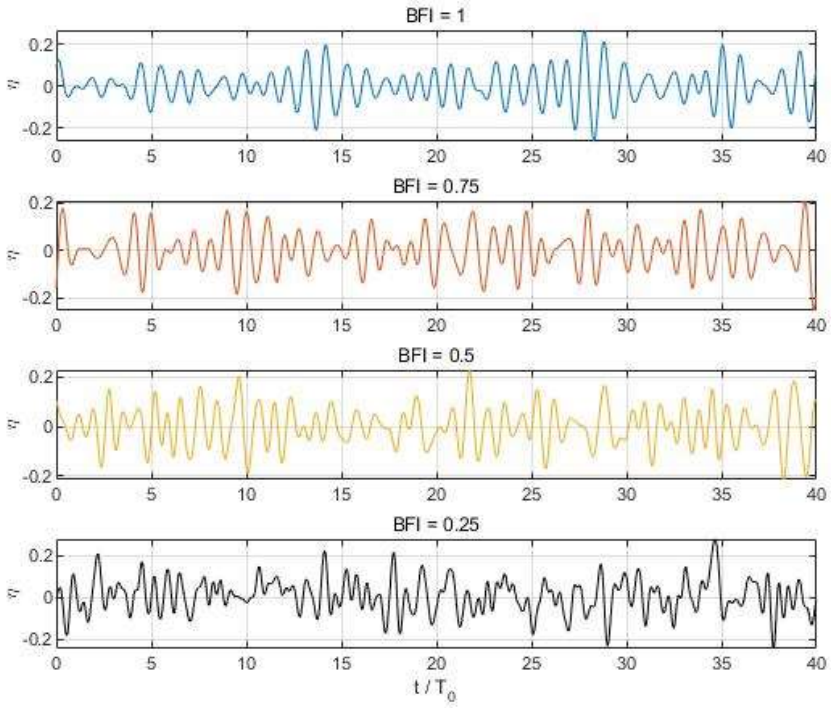

Figure 3.4 Samples of free surface elevation in time series from different initial BFI at $x = x_0$ when $\varepsilon = 0.1$

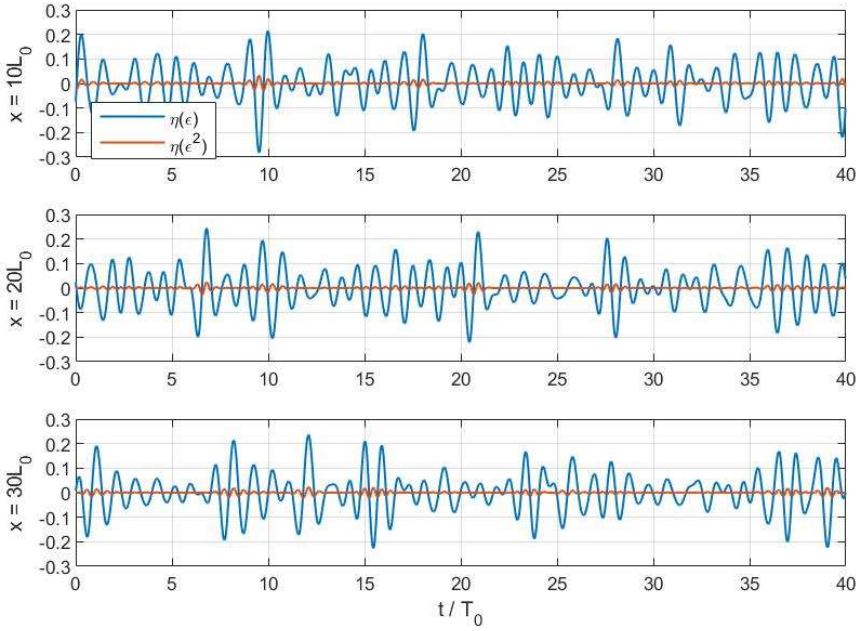

Figure 3.5 Samples of contribution on free surface elevation from the first and second-order in time series from initial BFI = 0.75 at $x = 10L_0, 20L_0, 30L_0$ when $\varepsilon = 0.1$, $kh = 7$

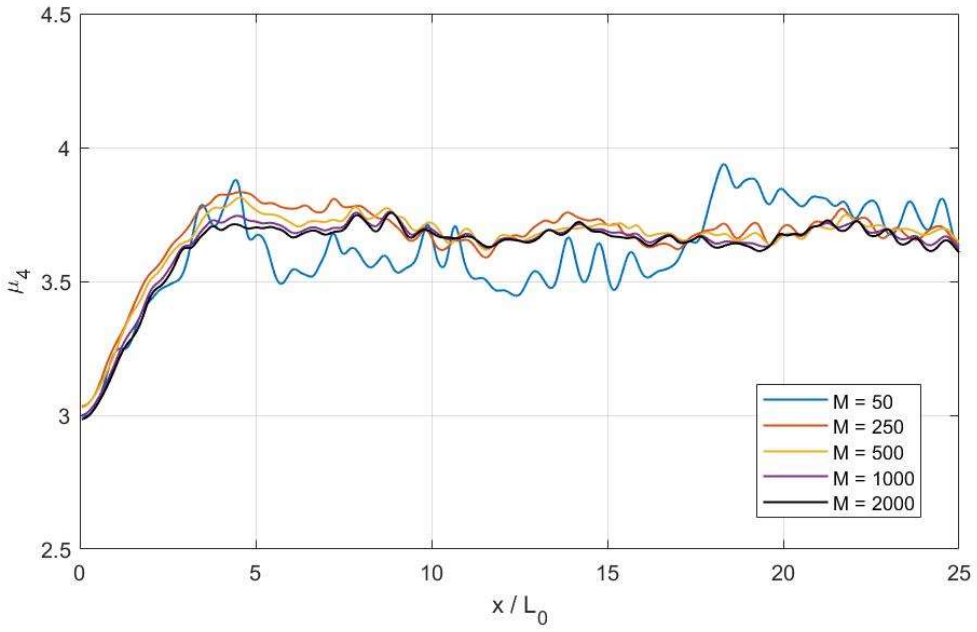

Figure 3.6 Spatial evolution of kurtosis from different ensemble size M when initial BFI = 0.75, kh = 4.0

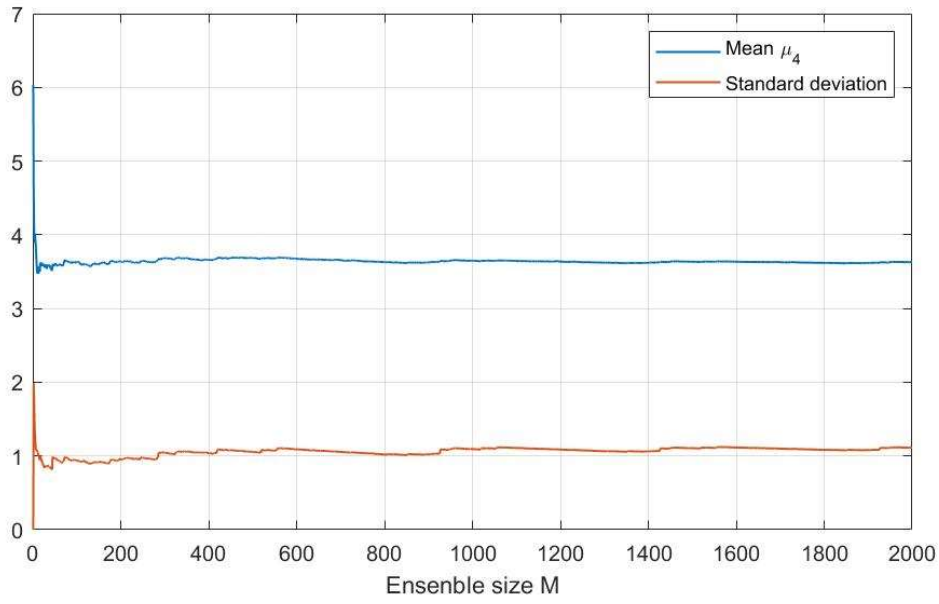

Figure 3.7 Variation of mean value and standard deviation of kurtosis with ensemble size M at $x = 25L_0$, initial BFI = 0.75, kh = 4.0

To figure out what role does the slope of bottom topography play in the high-order non-linear wave evolution, we assume water depth h only varies for x as described in **3.1**. We consider the flat bottom case and three different bottom slopes as shown in **Figure 3.8**. The wave train propagates from the left to right starting in flat region with enough deep-water depth to achieve a stabilized high-order non-linear condition. When wave train comes to the slope region, dimensionless water depth kh changes from kh = 7.0 to kh = 1.1 in all three types. With the hypothesis $h'(x) = O(\varepsilon^2)$, we assume the slope is very mild and $h'(x)$ = 0.05, 0.02, 0.01. When water depth kh reaches 1.1, it is enough shallow in mNLS equation and closed to limitation of our model due to the increasing water steepness ε, so we set water depth come back to flat. In **Figure 3.8,** the initial water depth h = 11 and initial wave length L_0 = 9.75 obtained by dispersion relation in Eq. (2-7), slope regions start at x = $15L_0$ and end up at x = $35L_0$, $65L_0$, $115L_0$ for different slope. In each spatial calculation step, $\mathrm{d}\xi_i$ = $2\times10^{-6}L_0$.

Figure 3.9 gives the changes in shoaling coefficient β_h, dispersion coefficient β_t and non-linear coefficient β_n in Eq.(3-9) in wave evolution for different bottom topography. Downward triangle in black represents starting point of slope, and upward triangle in different colors represent starting point of slope for different bottom topography (blue: slope = 0.05, red: slope = 0.02, yellow: slope = 0.01). Following figures continue to use them to represent slope region at *x*-axis. From Eq.(3-10), β_h = 0 when bottom is flat. As the water depth changes from deep to shallow, β_h first descends to minimum at kh = 1.785 (for slope = 0.05: x/L_0 = 32.5; slope = 0.02: x/L_0 = 58.5; slope = 0.01: x/L_0 = 101) and then rises to maximum at kh = 1.1 (for slope = 0.05: x/L_0 = 35; slope = 0.02: x/L_0 = 65; slope = 0.01: x/L_0 = 115) in the end of slope region. Extremum of β_h is decided by slope, and the maximum and absolute minimum will both be enlarged when $h'(x)$ rises. β_t, β_n are only decided by water depth kh, and smaller slope angle will make this process milder. In slope region, β_t first rises to maximum at the same water depth where β_h reaches minimum, and begins to decreases. β_n monotonically decreases with water depth decreasing, but absolute β_n first decreases to 0 at kh = 1.614 (for slope = 0.05: x/L_0 = 33.2; slope = 0.02: x/L_0 = 60; slope = 0.01: x/L_0 = 105) and then increases, which indicates the contribution from β_n in wave train nonlinearity may have a process of increasing first and then decreasing. What the variety from coefficients bring to wave evolution will be reflected in high-order moments, wave heights and wave height

distribution as following section.

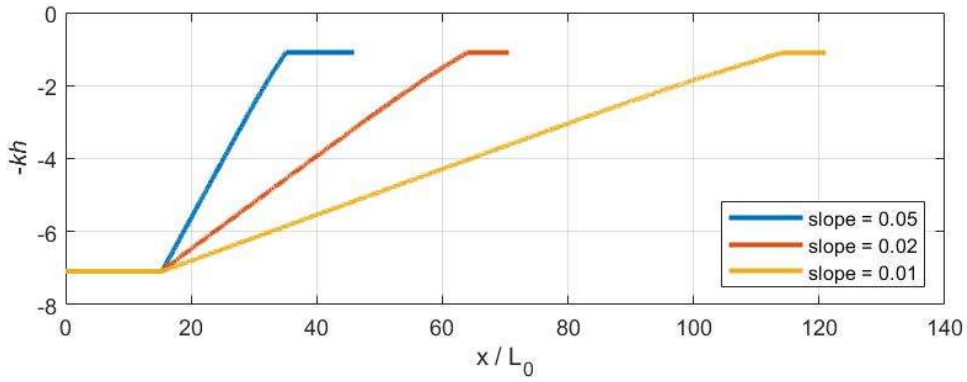

Figure 3.8 Schematic view of different bottom topography with kh = 7.0 – 1.1

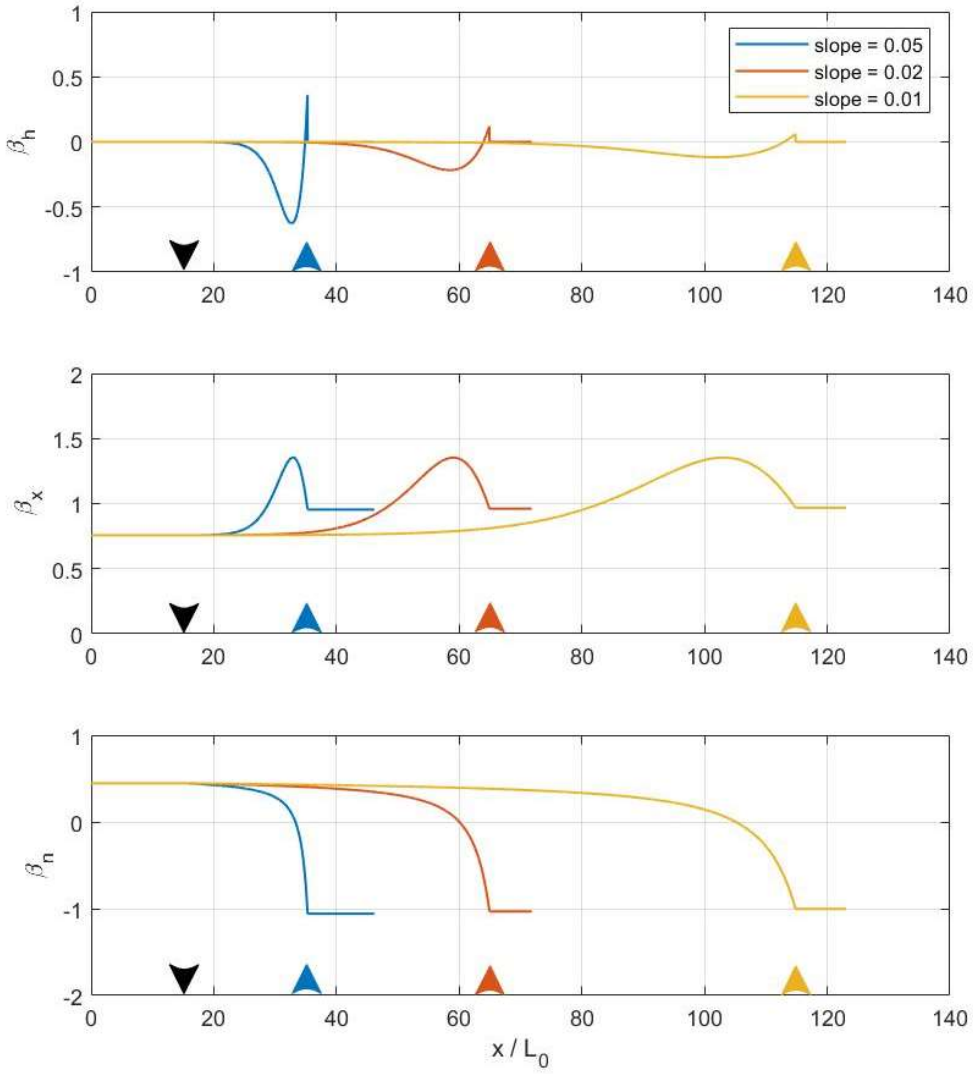

Figure 3.9 Coefficients in mNLS equation for different bottom topography

3.3 Evolution of modulated wave over a flat bottom

Firstly, we set β_h = 0 to give the numerical result over a flat bottom as the reference. When β_h = 0, Eq. (3-9) is in the form of standard NLS equation for unidirectional wave. In **Chapter 1**, we mentioned dimensionless moment kurtosis μ_4 and skewness μ_3 in surface elevation statistic. The Gaussian distribution suggests μ_4 = 3 and μ_3 = 0, but nonlinearity in wave evolution will give different expected values.

Figure 3.10 and **Figure 3.11** show the evolution of μ_4 and μ_3 in a flat bottom with different water depth kh at initial BFI = 0.75. Mean μ_4 monotonically decreases when water depth kh declines. In contrast, kh has little effect on μ_3 when $kh \geq 2$, and μ_3 will significantly increase in shallow water.

In **3.2.3**, we give the initial wave data with wave steepness ε = 0.1 and we change σ_s to give different initial BFI based on the dispersion on the frequency spectral. Wave steepness ε also plays an important role in the modulational instability, and the magnetic of ε represents the degree of the nonlinearity in wave train. Therefore, we also want to discuss the effect from different ε in the same initial BFI. For the uneven bottom topography in **Figure 3.8**, wave steepness starts from ε = 0.1 and increases to 0.13 at the end kh = 1.1 due to the wave shoaling effect, so we give μ_4 and μ_3 in both ε = 0.1 and ε = 0.13 in **Figure 3.10** and **Figure 3.11** to have a comparison. In flat bottom kh = 1.1, effect from ε on μ_4 is very small, but enlarging ε will significantly increases μ_3. **Figure 3.12** and **Figure 3.13** give the evolution of μ_4 and μ_3 in flat bottom with different wave steepness ε and the initial BFI is constant at 0.5, where the water depth is finite at kh = 4. As the ε increases from 0.05 to 0.2, μ_4 and μ_3 increases. The effect from the water steepness is more significant in μ_3 than μ_4, since μ_3 mainly reflect the second-order effect in bound wave theory.

Figure 3.14 and **Figure 3.15** show the comparison between μ_4 and μ_3 in different water depth with flat bottom. When kh = 4.0, kurtosis and skewness increase as the BFI becomes higher. However, it is contrast when kh = 1.1 that kurtosis and skewness at lower BFI will significantly increase. For modulated wave trains, the nonlinearity comes from the contribution

from two parts: four-wave interaction in the third-order (estimated by BFI) and second-order effect. In deep-water, wave trains is mainly determined by BFI and higher BFI leads to larger μ_4 and μ_3. When water depth becomes shallow, the four-wave interaction becomes weak and makes μ_4 and μ_3 decrease, but in a small kh the increase of wave steepness ε will increase μ_4 and μ_3 in different levels. For wave trains starting with low BFI in shallow water, the decrease of μ_4 and μ_3 caused by the third-order effect is small compared with the increase caused by the second-order effect, which leads to the converse behavior about BFI in deep and shallow water. It can also explain the critical depth for modulated wave in Benjamin (1967). μ_3 is more sensitive about the second-order effect so it significantly increases in shallow water.

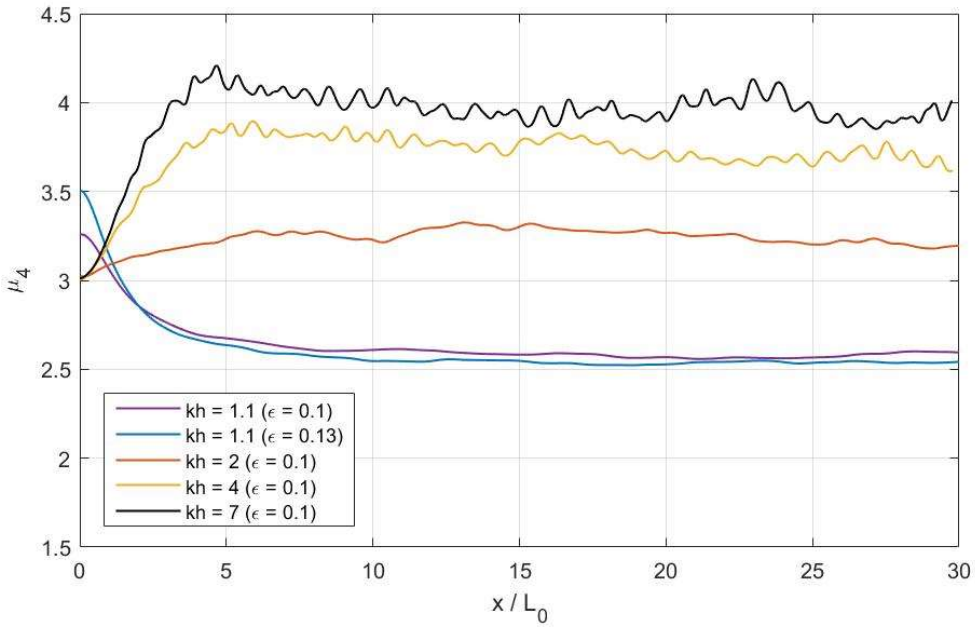

Figure 3.10 Spatial evolution of kurtosis in flat bottom, initial BFI = 0.75

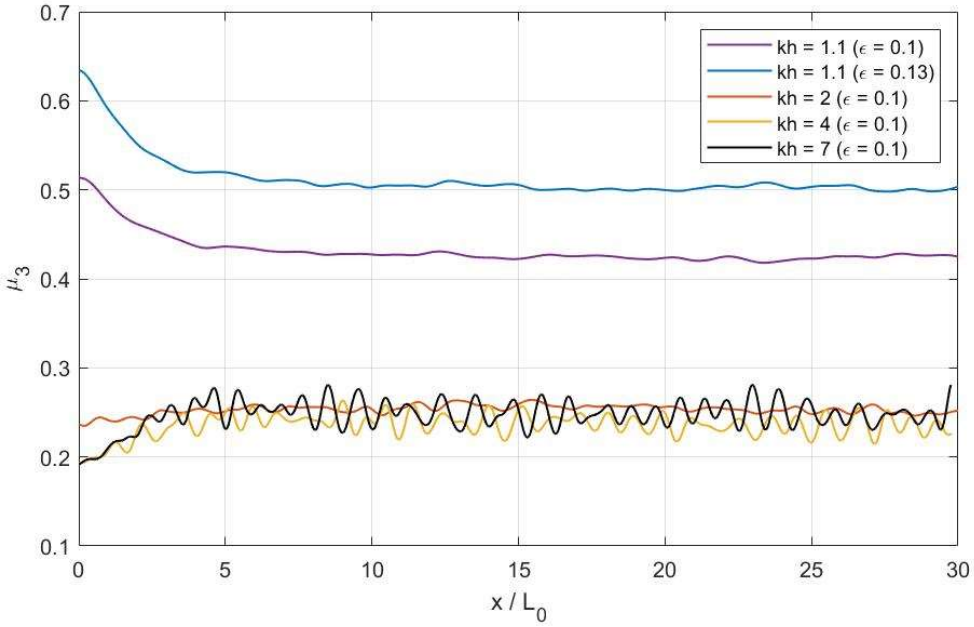

Figure 3.11 Spatial evolution of skewness in flat bottom, initial BFI = 0.75

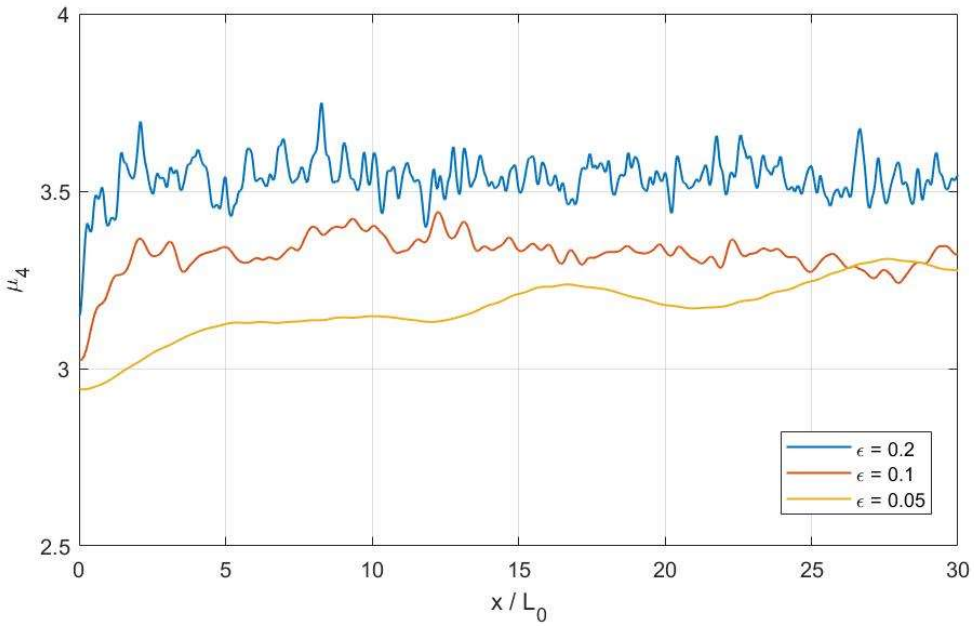

Figure 3.12 Spatial evolution of kurtosis in flat bottom, when initial BFI = 0.5, σ = 0.14, 0.28, 0.57, kh = 4.0

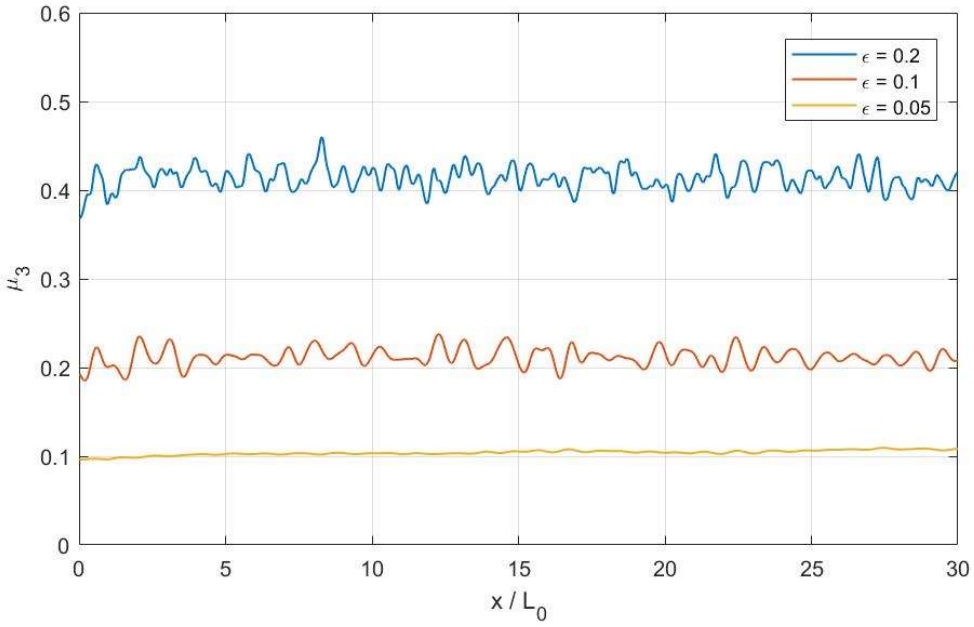

Figure 3.13 Spatial evolution of Skewness in flat bottom, when initial BFI = 0.5, σ = 0.14, 0.28, 0.57, kh = 4.0

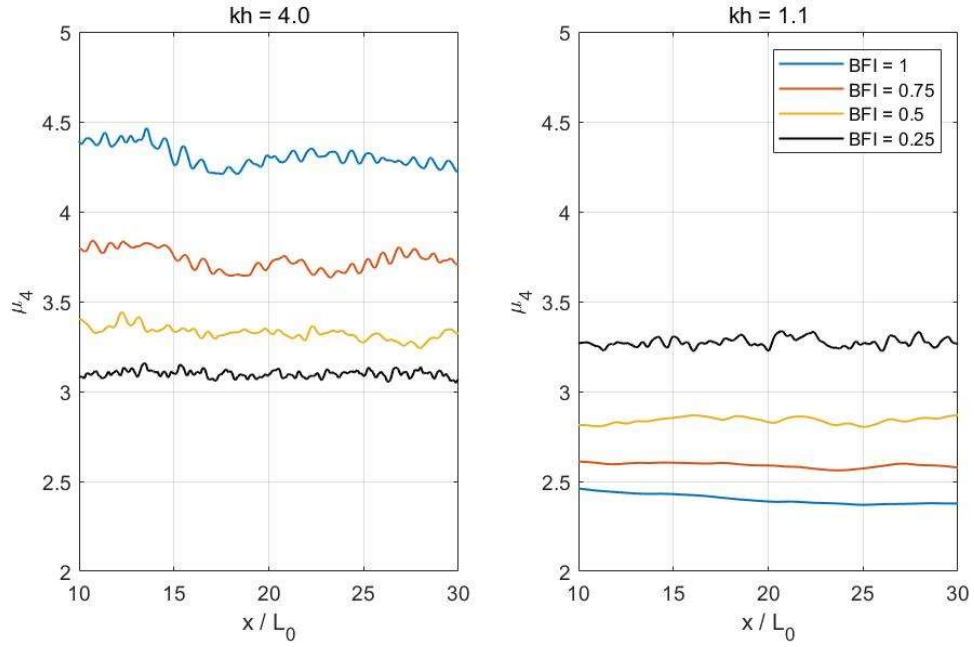

Figure 3.14 Spatial evolution of kurtosis in flat bottom with different initial BFI

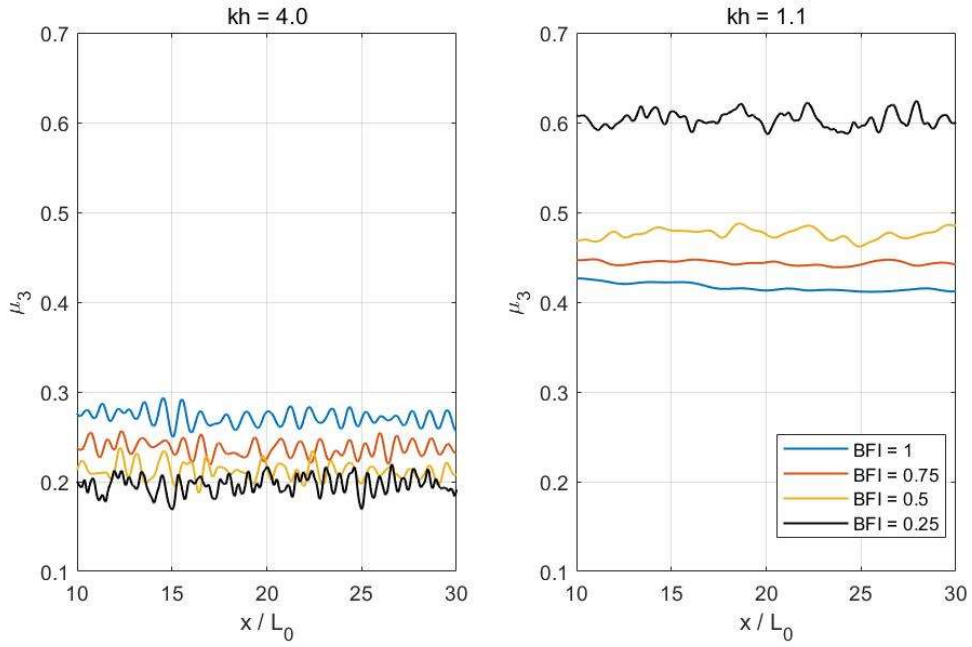

Figure 3.15 Spatial evolution of skewness in flat bottom with different initial BFI

3.4 Evolution of modulated wave over an uneven bottom

3.4.1 Evolution of the high-order nonlinearity

Here we start the discussion about the nonlinearity from the high-order statistical moment in different initial condition on an uneven bottom. As a validation, **Figure 3.16** shows the comparison between numerical result from this model and the experiment from Kashima and Mori (2019). We select the experimental data in the step bottom wave tank to have a comparison because wave breaking doesn't occur in this case as well as this numerical model. Wave maker gives initial condition that wave steepness ε = 0.066, BFI = 1.45 and Q_p = 4.7. The water depth starts from h = 0.5, kh = 2.077 and decreases to h = 0.2, kh = 1 with a slope 1/30. In **Figure 3.16**, both numerical result and experiment data show that μ_4 and μ_3 have similar evolution process: increase at the end of slope region, and immediately drops at flat bottom in shallow water. The numerical model seems to overestimate the value of μ_3, and it comes from the limitation of mild slope in this model that ε = 0.066 and slope 1/30 exceed the assumption $h'(x) = O(\varepsilon^2)$. Additionally, the numerical NLS model more applies to deep and finite water, and we find the result will be not reliable when h is too small. Here h = 0.2 is very closed to

the limit range. We make ε = 0.1 and kh = 7 – 1.1 in following numerical result as the setting in **3.2.3**.

In **Figure 3.17,** mean value of kurtosis μ_4 from Monte Carlo simulation from different bottom topography are in the comparison with μ_4^b and μ_4^* from Eq.(1-5) and Eq.(1-6). μ_4^b is given by wave steepness ε in result of slope = 0.01. **Figure 3.17** shows spatial evolution of kurtosis μ_4 for different initial BFI, while μ_4^b doesn't change with BFI because μ_4^b is a function only for ε in bound wave theory. The differences between μ_4^* and μ_4^b demonstrate the proportion of fourth-order cumulant in nonlinearity.

The mean value of μ_4 from numerical result is significantly affected by initial BFI. Enlarging initial BFI will lead to higher μ_4 in deep-water, but lower μ_4 in shallow water. In deep-water before slope region, μ_4 basically matches μ_4^* for different initial BFI, which provides a consistency with Mori and Janssen (2006) about the estimation of nonlinearity from four-wave interaction in deep-water. When slope angle is taken into consideration, μ_4 in slope region have a descending process from deep to shallow water. At the end of slope region, μ_4 has a slightly rebound due to wave shoaling, and the magnitude of this rebound will be enlarged by larger slope angle. However, when initial BFI is small (Initial BFI = 0.25), the four-wave interaction is weak in wave train and μ_4 becomes less affected by kh, and maximum μ_4 occurs in shallow water, which is consistent with the prediction of μ_4^b.

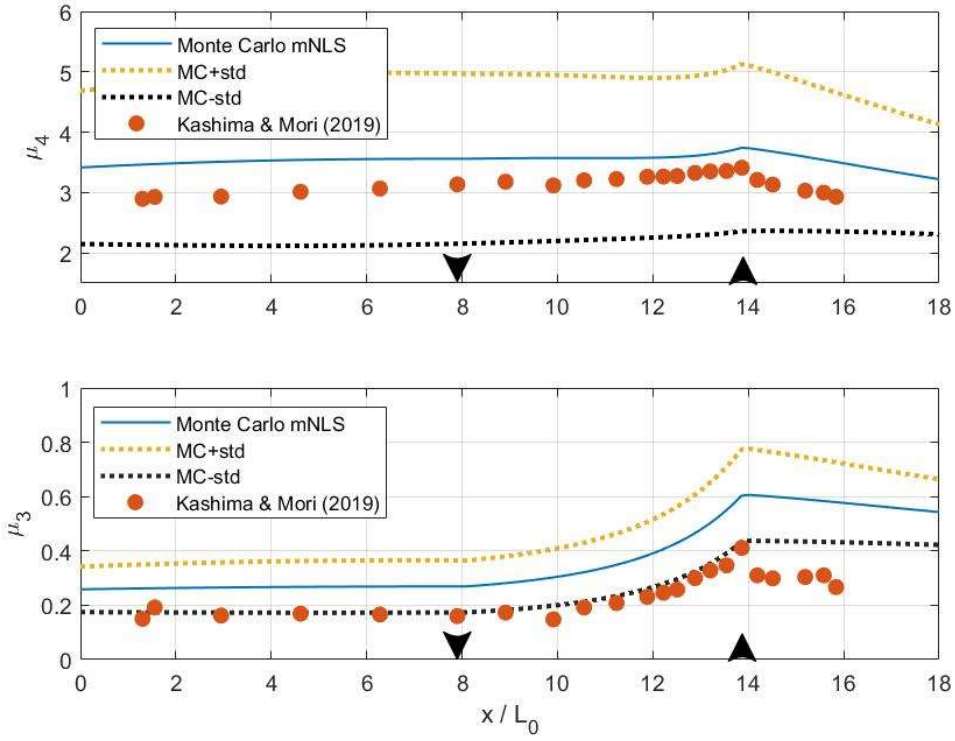

Figure 3.16 Spatial evolution of kurtosis and skewness in comparison with experiment data on the step bottom

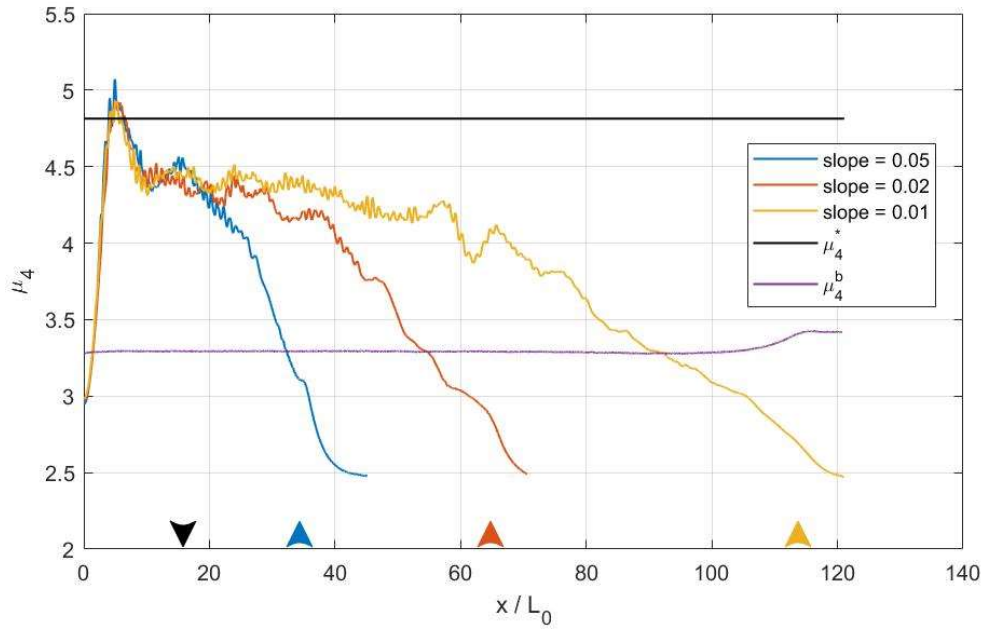

(a) Initial BFI = 1

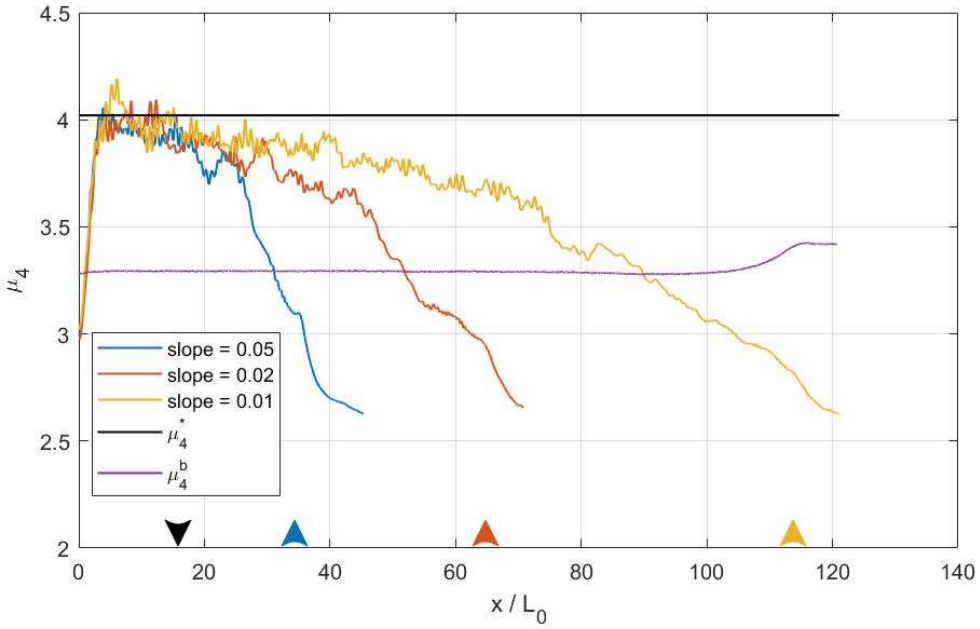

(b) Initial BFI = 0.75

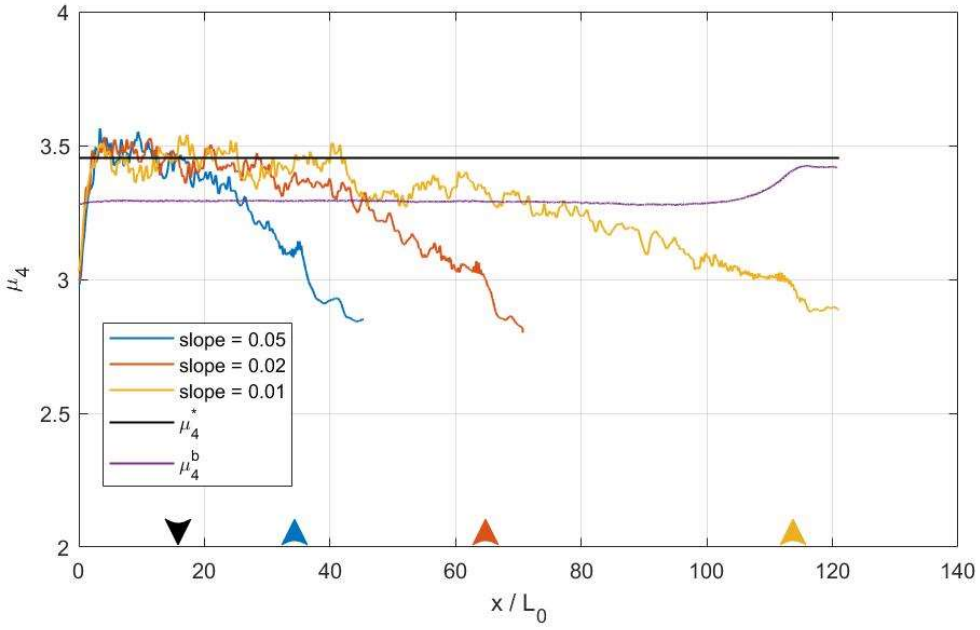

(c) Initial BFI = 0.5

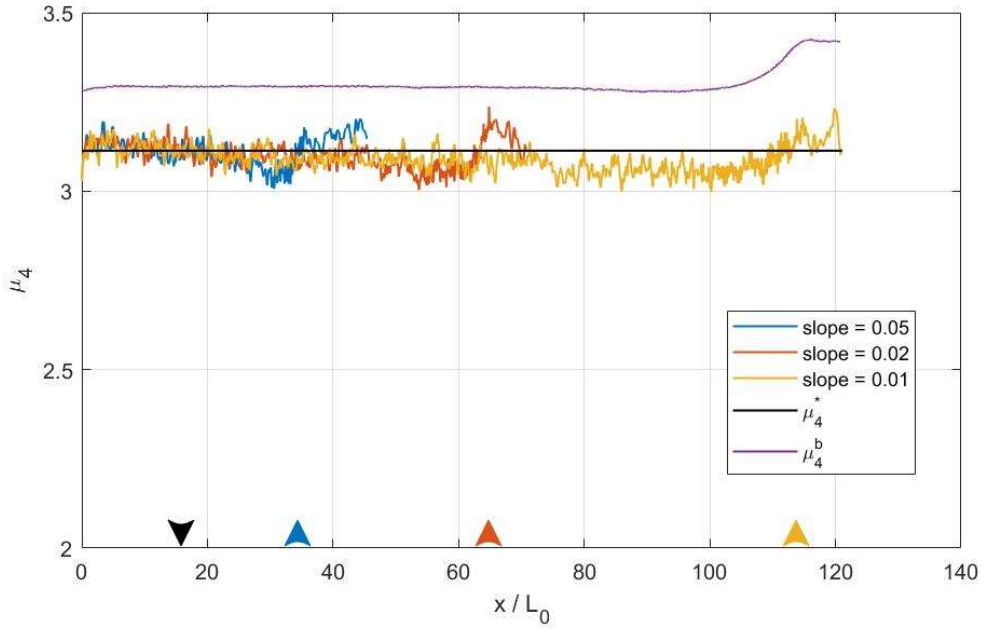

(d) Initial BFI = 0.25

Figure 3.17 Spatial evolution of kurtosis from different bottoms and initial BFI

Figure 3.18 shows the comparison between numerical result and theoretical value of skewness μ_3 in the same form of **Figure 3.17**. In the second-order random wave theory in Mori and Janssen (2006), μ_4 is given to be related to μ_3 in bound wave model by Eq.(1-5). However, can this relationship be established only when $kh \geq 2.5$ (for slope = 0.05: $x/L_0 \leq 30$; slope = 0.02: $x/L_0 \leq 53$; slope = 0.01: $x/L_0 \leq 90$). When $kh < 2.5$, μ_3 starts to increase as kh decreasing and μ_3 reaches maximum value at $kh = 1.1$(for slope = 0.05: $x/L_0 = 35$; slope = 0.02: $x/L_0 = 65$; slope = 0.01: $x/L_0 = 115$), the end of slope region. After water depth is stable at $kh = 1.1$, μ_3 decreases to a smaller value but still larger than deep-water. Compared with the rising magnitude of μ_3 as kh decreases in shallow water, this decline in deep-water is very small. Additionally, when initial BFI is large (BFI $\geq$ 0.5), steep slope will lead to a larger maximum of μ_3 at the end of slope region.

Different with μ_4 that, four-wave interaction is not major contributing factor in evolution of μ_3. Maximum μ_3 occurs in shallow water and wave shoaling plays an important role in the evolution of μ_3. In Eq.(3-10), wave shoaling effect is estimated by the slope angle and variation of wave number, and we find μ_3 reaches its maximum at the same position with maximum

shoaling coefficient β_h refer to **Figure 3.9**. **Figure 3.9** and **Figure 3.18** indicate, when wave trains come to shallow water, the non-linear effect from wave shoaling will reflect in μ_3, and steep slope angle will enlarge this effect. μ_3^b in bound wave model predict the rise of μ_3 in shallow water base on the increase of wave steepness in the second-order, but doesn't consider the contribution from slope angle.

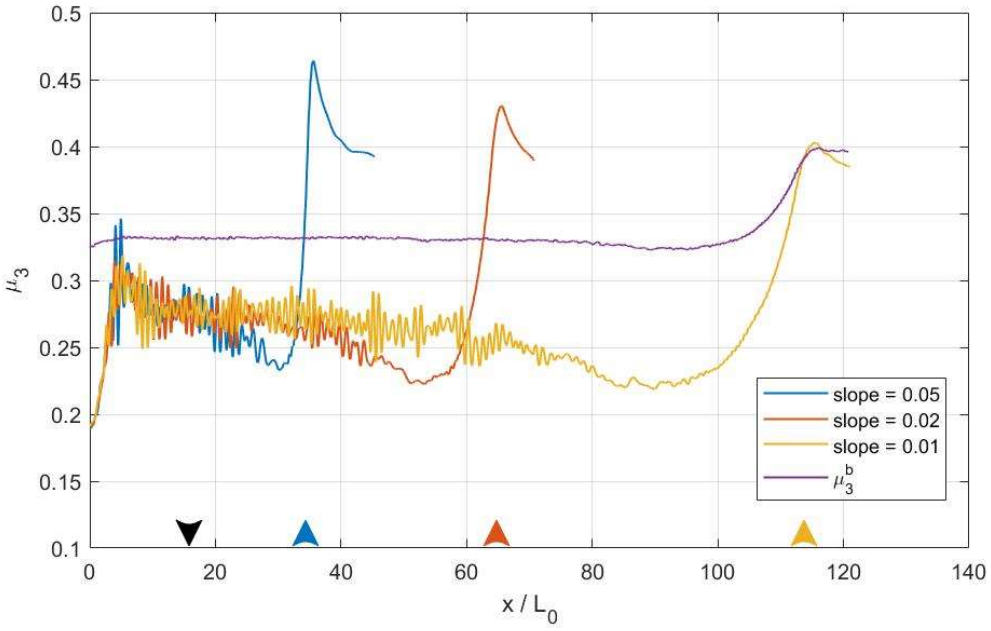

(a) Initial BFI = 1

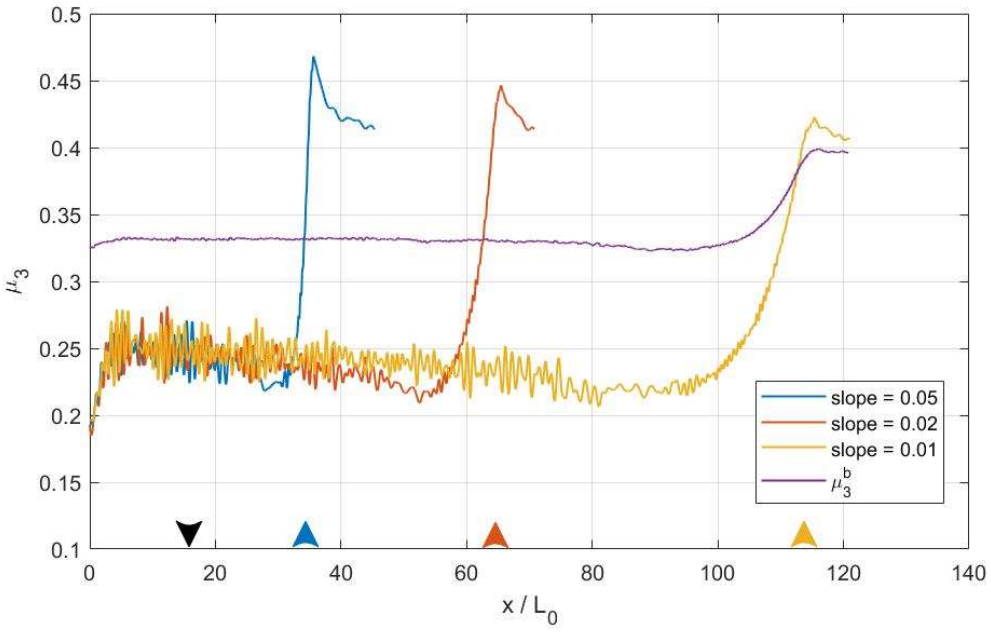

(b) Initial BFI = 0.75

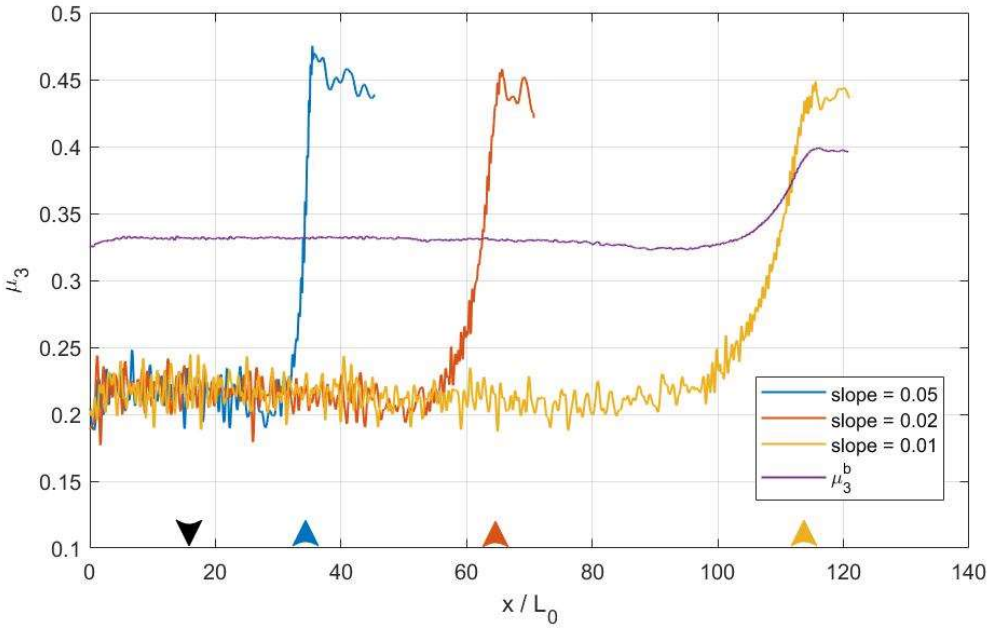

(c) Initial BFI = 0.5

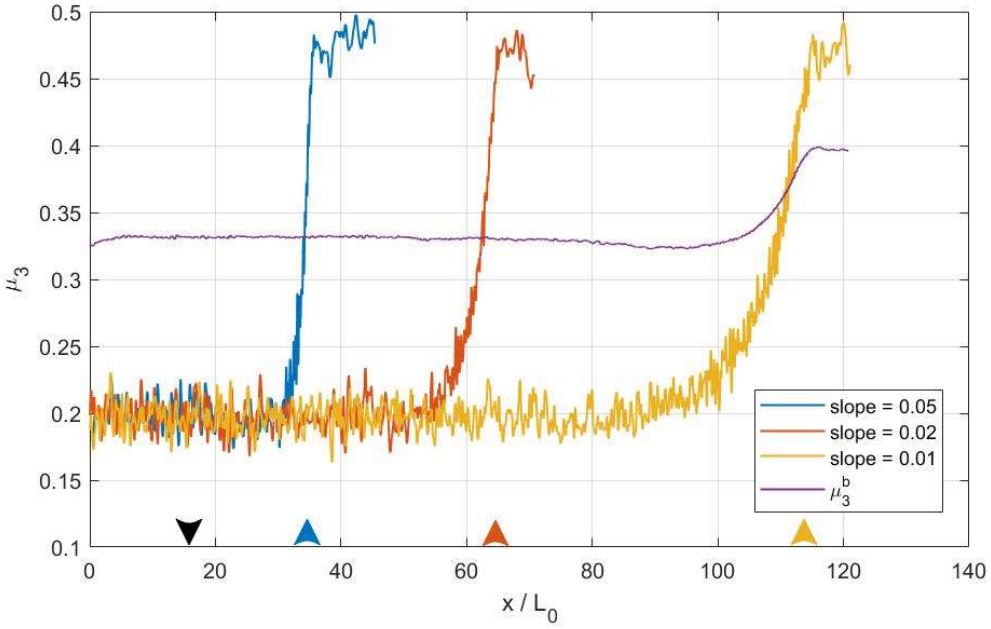

(d) Initial BFI = 0.25

Figure 3.18 Spatial evolution of skewness from different bottoms and initial BFI

Figure 3.19 gives the variation of Q_p from Eq. (3-21) for different bottom topography and initial BFI. Q_p is decided by BFI in a clear way since the definition of BFI is also related to the spectral bandwidth, and Q_p starts to be affected by water depth kh as BFI increasing. For large initial BFI at slope = 0.05, Q_p reaches maximum around 3.5 in the area $kh \approx$ 2.5 ~ 1.5 (x/L_0 = 30 ~33), and drops rapidly until the bottom becomes flat at kh = 1.1 (x/L_0 = 35). When slope = 0.02 and 0.01, maximum Q_p are basically the same with slope = 0.05 but the corresponding area are $kh \approx$ 2.8 ~ 1.5 (x/L_0 = 50 ~ 60) and $kh \approx$ 3 ~1.3 (x/L_0 = 80 ~ 105). Similar process can be observed in lower initial BFI but not very significant. Variation of Q_p with kh is similar but not the same with μ_3 and β_h. Compared with μ_3, Q_p is more sensitive to initial BFI, and the maximum value occurs ahead of the end of slope region, where μ_3 and β_h reaches maximum.

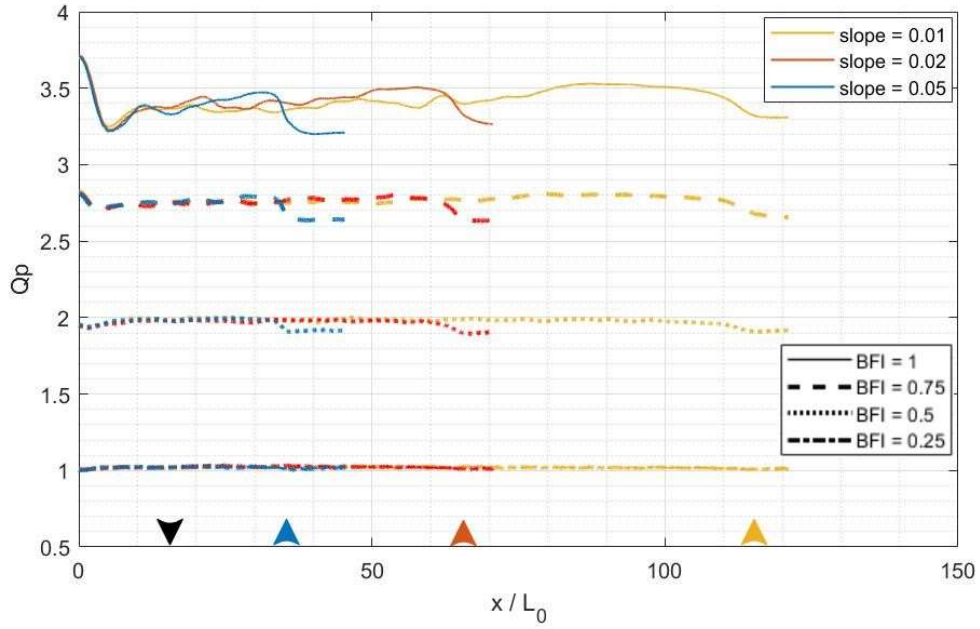

Figure 3.19 Spatial evolution of Qp from different bottoms and initial BFI

3.4.2 Statistics of extreme event in surface elevation

In **3.4.1**, we discuss the changes of wave spectral statistics due to the high-order nonlinearity in wave evolution with average value from the Monte Carlo simulation. Previous studies indicated that the increasing kurtosis accelerates occurrence probability of extreme waves in the train (e.g. Janssen, 2003; Mori and Janssen, 2006). Although the skewness contribution is strong for wave crest heights, the changes of kurtosis in extreme is dominative for total wave heights (crest to trough height) (e.g. Mori and Janssen, 2006; Mori et al., 2007; Kashima and Mori, 2019). We here examine the effects of high-order nonlinearity on the extreme wave height and crest height on the slope.

Figure 3.20 shows average value with their standard deviation for μ_4, μ_3 and maximum wave height $H_{\max}$ when initial BFI = 0.75. The $H_{\max}$ is sampled from a maximum value for each realization of 300 ensembles. We use $H_{\max}/\eta_{\mathrm{rms}}$ for dimensionless, and expected $H_{\max}$ is given by Mori and Janssen (2006) based on fourth-order cumulant κ_{40} from Eq.(1-8). The value of standard deviation expects how far result spread out from their average value, and it helps to estimate maximum value and wave train instability.

From deep to shallow water, envelope consist of mean and ± standard deviation of $H_{\max}$ first rises up and become stable in flat bottom, then declines as the water depth decreases in slope region, and finally stable at minimum in shallow water. Additionally, the width of this envelope of $H_{\max}$ also decreases with slope, which indicates wave train in deep-water is more unstable and unpredictable than shallow water. Similar with $H_{\max}$, width of envelope of μ_4, μ_3 also get narrow when water depth becomes shallow. Refer to Mori and Janssen (2006), expected $H_{\max}$ in purple line predicted by fourth-order cumulant κ_{40} matches numerical result well in deep-water, but overestimates $H_{\max}$ in shallow water after slope region.

At the end of slope region kh = 1.1(for slope = 0.05: x/L_0 = 35; slope = 0.02: x/L_0 = 65; slope = 0.01: x/L_0 = 114), μ_4 and μ_3 have a rebound due to wave shoaling as our discussion about **Figure 3.17** and **Figure 3.18**. In **Figure 3.20**, standard deviation of μ_4 and μ_3 have same process. Correspondingly, it also reflects in expected $H_{\max}$, and steep slope will enlarge this effect in the comparison of different topography. However, evolution of mean and standard deviation of $H_{\max}$ from numerical result varies smoothly from slope region to flat

bottom in shallow water, even μ_4 and μ_3 from numerical result suggest wave shoaling effect brings about the increase of nonlinearity and wave train instability. In both observation record and theoretical estimation, the occurrence probability of freak wave is on a very small scale, so standard deviation and mean value are not enough in the analysis of contribution of high-order nonlinearity from the slope to the extreme case.

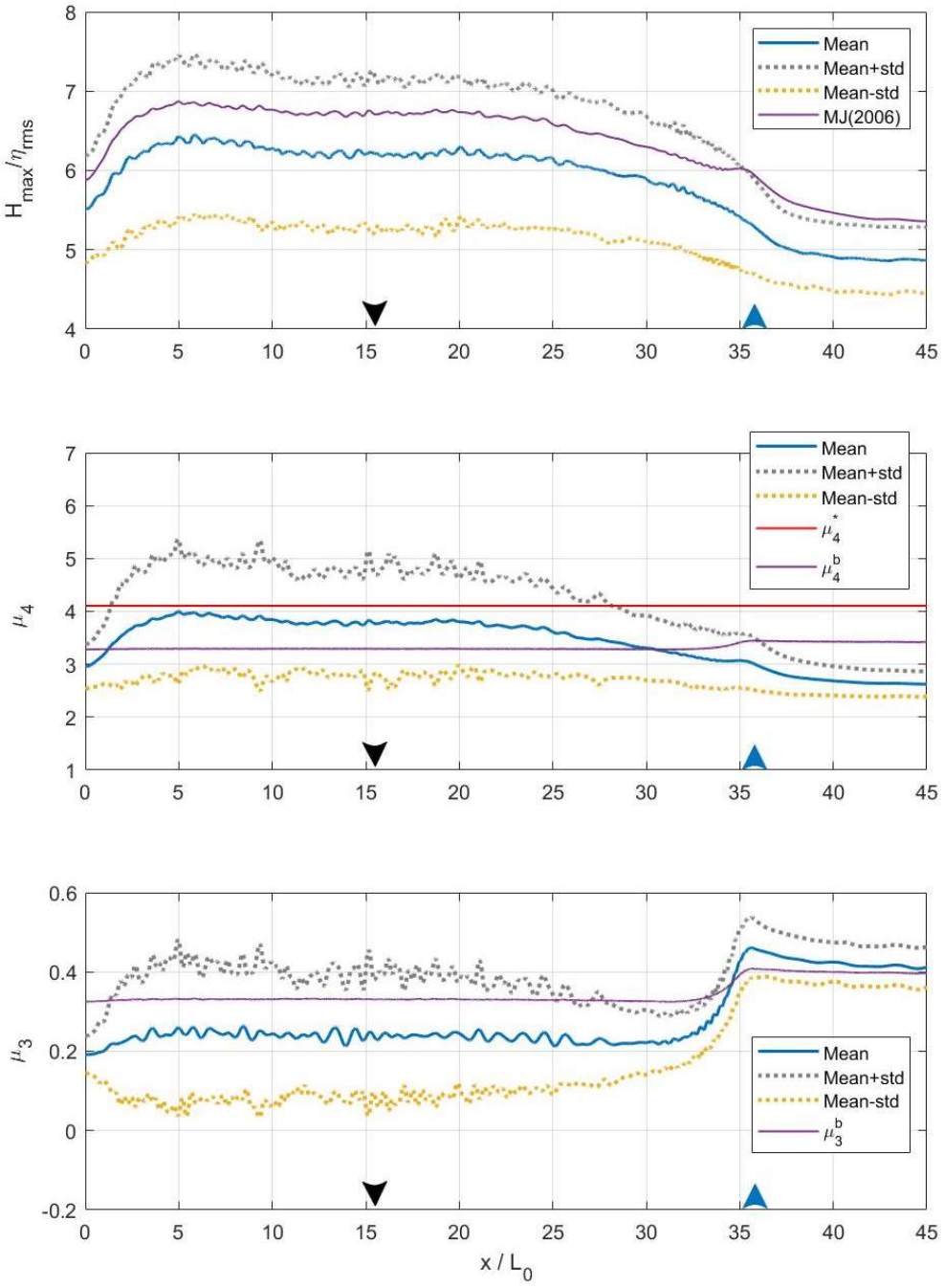

(a) slope = 0.05

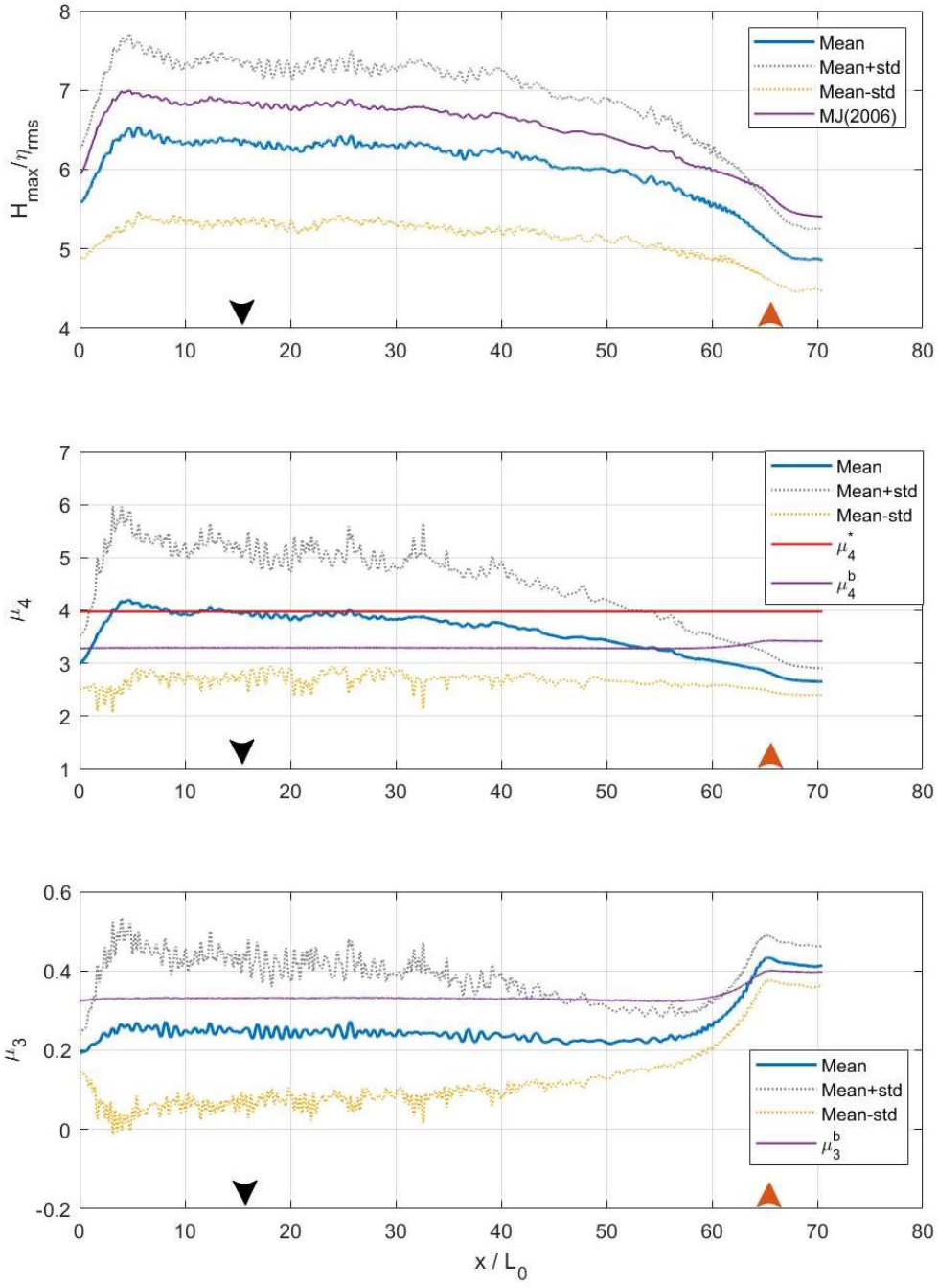
Mean
Mean+std
Mean-std
MJ(2006)
H_{max}/η_{rms}
μ_4
μ_4^*
μ_4^b
μ_3
μ_3^b
x / L_0

(b) slope = 0.02

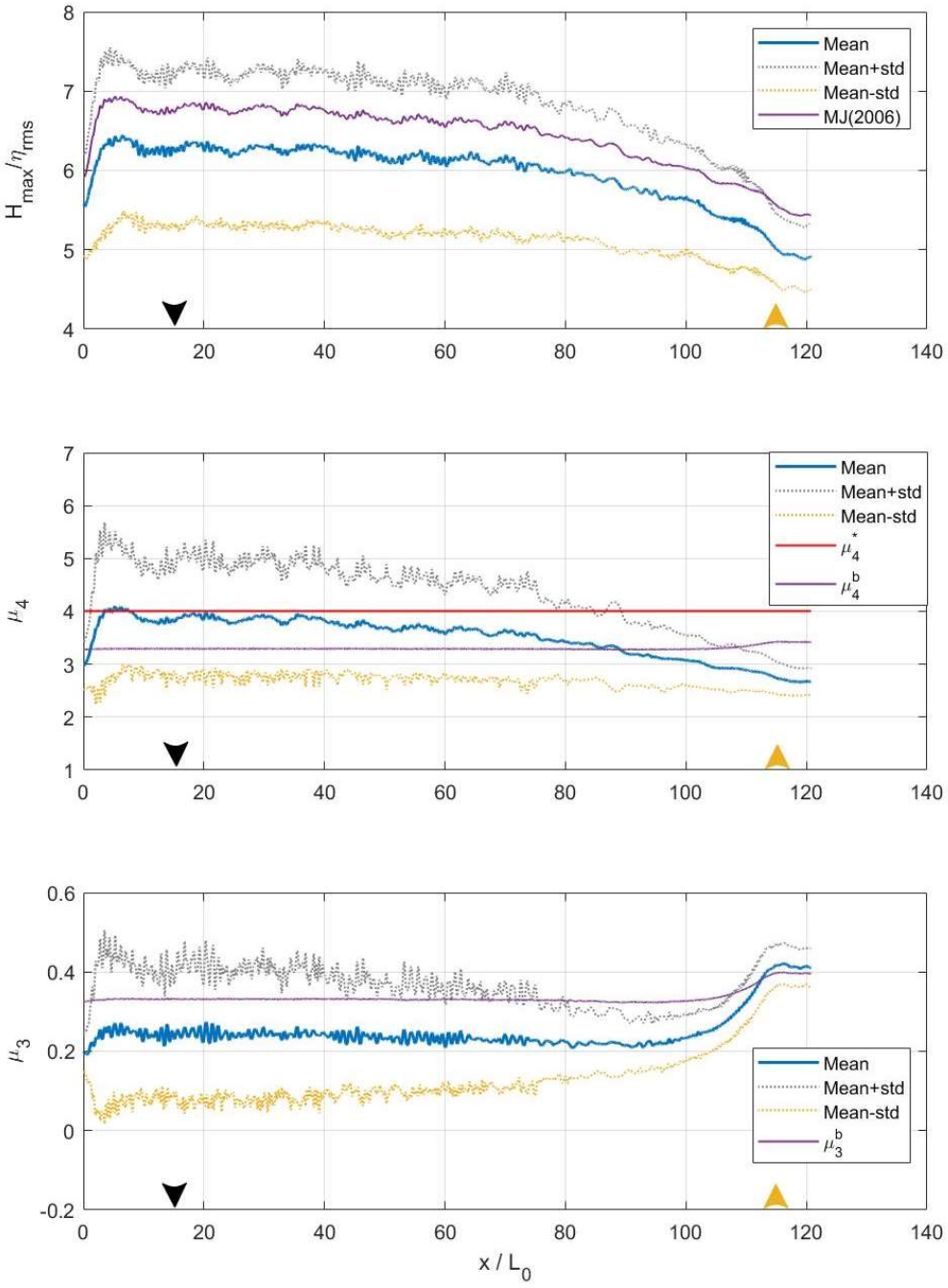

(c) slope = 0.01

Figure 3.20 Mean $H_{\max}$, μ_4 and μ_3 from different bottom topography with initial BFI = 0.75

To develop this discussion with more details and make extreme event more clear, we plot Cumulative Distribution Function (CDF) of maximum wave height $H_{\max}$ from numerical result by scatters in logarithmic coordinates in **Figure 3.21** (a). As a comparison, expected $H_{\max}$ in the Rayleigh distribution and Mori and Janssen (2006) from μ_4 are plotted in solid lines. Usually we define freak wave as the wave height exceeds the significant wave height $H_{1/3}$ by a factor of 2, and Goda (2000) shows the relation $H_{1/3}$ = 4.004 η_{rms} by the linear random wave theory. Therefore, result from $H_{\max}/\eta_{\mathrm{rms}} > 8$ can be used as a reference of the freak wave estimation.

For flat bottom topography, numerical result corresponds with Mori and Janssen (2006)'s result better than Rayleigh distribution when $kh > 2$. When kh = 1.1, numerical result has large deviation with both linear and non-linear suppose. In the comparison of different slope, we choose three typical sections of water depth kh: kh = 1.785, where shoaling coefficient β_h reaches its minimum and dispersion coefficient β_x reaches its maximum; kh = 1.363, where $\mu_4 \approx 3$, a neutral condition that linear and non-linear theories have same result; kh = 1.1, at the end of slope region, where shoaling coefficient β_h and μ_3 reaches its maximum. Contribution from four-wave interaction to wave height distribution can reflect in the deviation between two theoretical curves in figures. When $\mu_4 > 3$, occurrence probability of extreme wave height predicted by Mori and Janssen (2006) is higher than Rayleigh distribution; when $\mu_4 < 3$, Mori and Janssen (2006)'s result is significantly lower than Rayleigh distribution in flat bottom.

As the water depth kh becomes smaller, the difference from slope generally apparent: steep slope lead to higher exceeding probability of large $H_{\max}$ specifically in shallow water. When kh = 1.785, the occurrence probability of large $H_{\max}/\eta_{\mathrm{rms}} > 8$ for steep slope (slope $h'(x)$ = 0.05) is 10 times larger than gentle slope (slope $h'(x)$ = 0.02), and it becomes 0 in very mild slope (slope $h'(x)$ = 0.01). This phenomenon can also be found in numerical result in Zeng and Trulsen (2012), and experimental data from Kashima and Mori (2019) and Trulsen et al. (2020). In kh = 1.363 and kh = 1.1, occurrence probability of extreme wave height is significantly lower than both two theoretical predictions, and effect from end of slope region

continues to lead to higher exceeding probability of large value in steep slope.

We also give analysis about extreme crest height, since it is very important in estimation of wave pressure and maritime structure design. In **Figure 3.21** (b), we give CDF of $\eta_{\max}$ distribution in the same form of $H_{\max}$. In Rayleigh distribution and Mori and Janssen (2006)'s result, maximum wave height $H_{\max}$ is assumed to be twice maximum $\eta_{\max}$. In numerical result of this study, wave height H is obtained from wave envelop and mostly decided by wave amplitude A. Surface elevation η in Eq.(2-58) considers the contribution from second-order and second harmonic in wave train, so the CDF of $\eta_{\max}$ is not exactly the same with $H_{\max}$. If Rayleigh distribution is taken as standard, we find the CDF curve of $\eta_{\max}$ for large value significantly exceed Rayleigh distribution than $H_{\max}$, which indicates the exceeding probability of $\eta_{\max}$ in large value is higher than $H_{\max}$. In flat bottom, this deviation becomes very obvious, especially in deep-water. From result of different slope in same water depth, steep slope brings about the increase of extreme value occurrence probability in a similar way with $H_{\max}$, and result in slope = 0.05 exceeds Rayleigh distribution when $\eta_{\max}/\eta_{\rm rms} > 4$.

As a supplement to the CDF in **Figure 3.21**, **Figure 3.22** give Probability Density Function (PDF) of $H_{\max}$ and $\eta_{\max}$ in form of bar graph correspondingly. Expected distribution in the Rayleigh distribution and Mori and Janssen (2006) are used as reference again. In CDF we concentrate on extreme large case, and PDF can provide more details and help to estimate peak probability. **Figure 3.22** (a) shows peak of PDF is mainly decided by water depth through μ_4. For given water depth, peak of PDF from different bottom topography almost have no change, which is corresponding to the result in **Figure 3.20** that the expected $H_{\max}$ is not effected by wave shoaling effect. Compared with $H_{\max}$ in **Figure 3.22** (a), $\eta_{\max}$ in **Figure 3.22** (b) have more significant deviation with the Rayleigh distribution. **Figure 3.21** (b) shows CDF of $\eta_{\max}$ far exceeds Rayleigh distribution for large value when slope = 0.05, which suggests the non-linear effect brought by wave shoaling and slope significantly enlarge the occurrence probability of extreme event. Deviation between maximum wave height and extreme crest height also points out, occurrence probability of extreme event will be promoted if second-order term is taken into consideration in freak wave analysis.

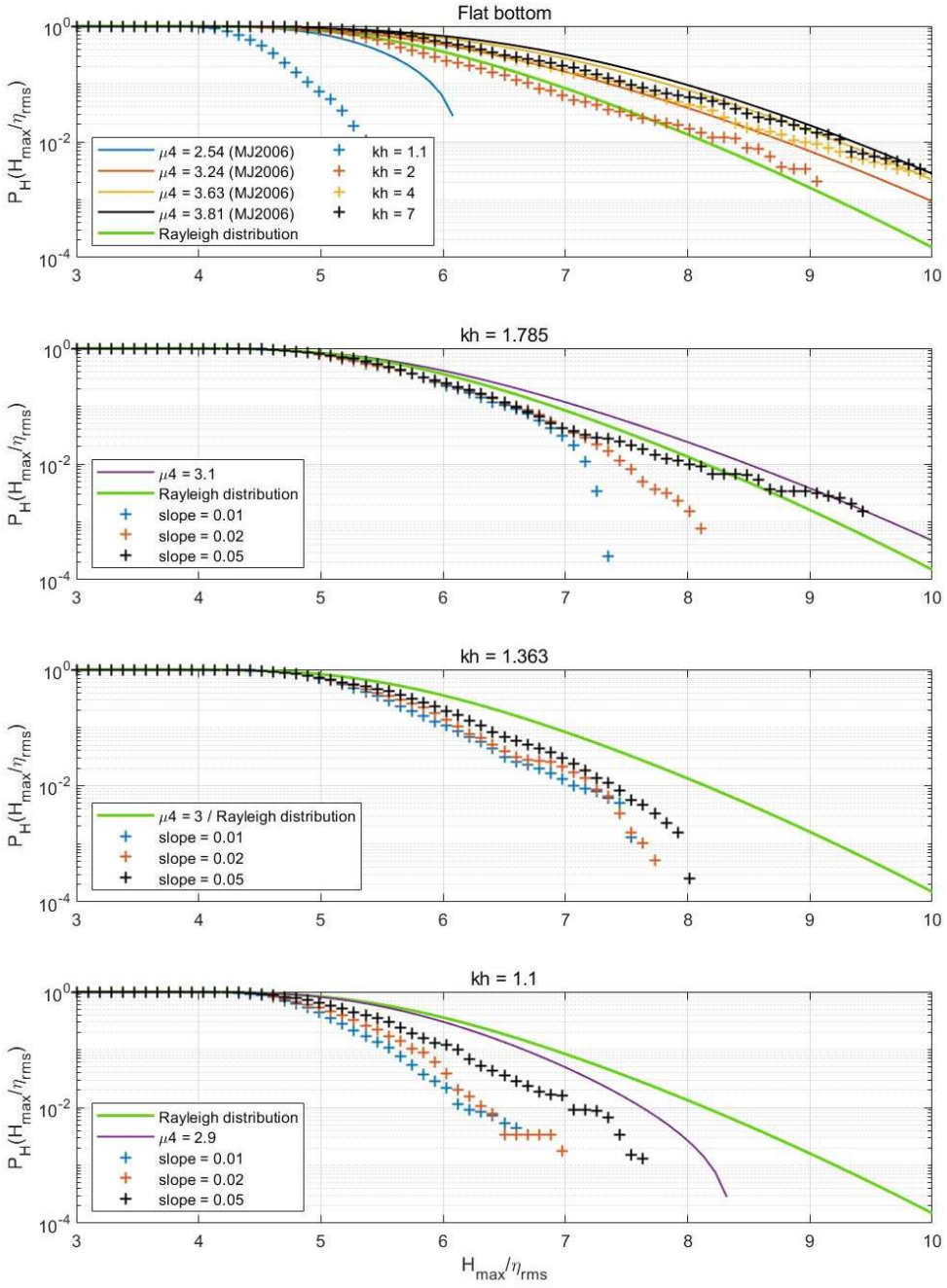

(a) Maximum wave height $H_{\max}$

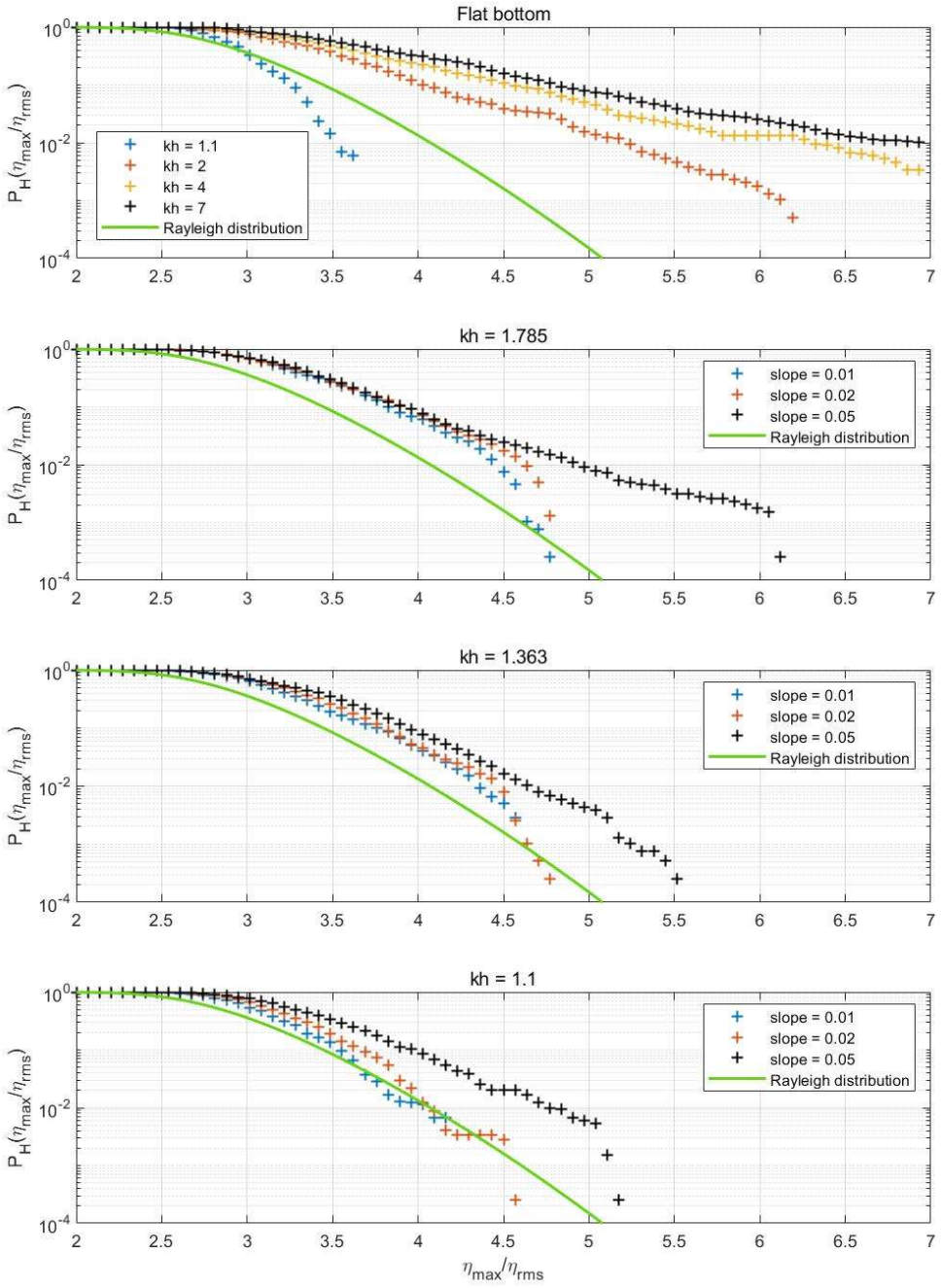

(b) Maximum free surface elevation $\eta_{\max}$

Figure 3.21 Exceedance probability of wave height and free surface elevation distribution, initial BFI = 0.75

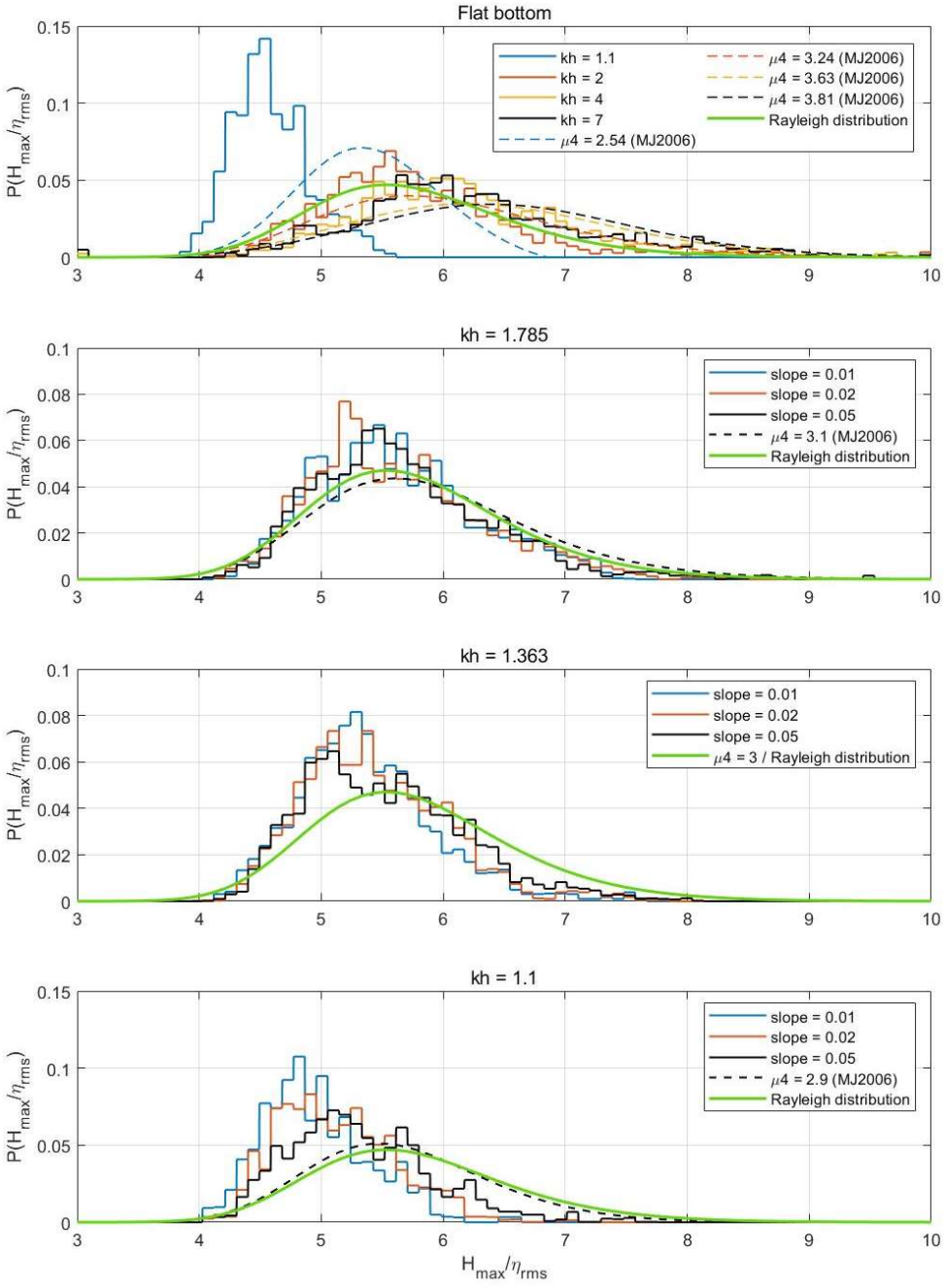

(a) Maximum wave height $H_{\max}$

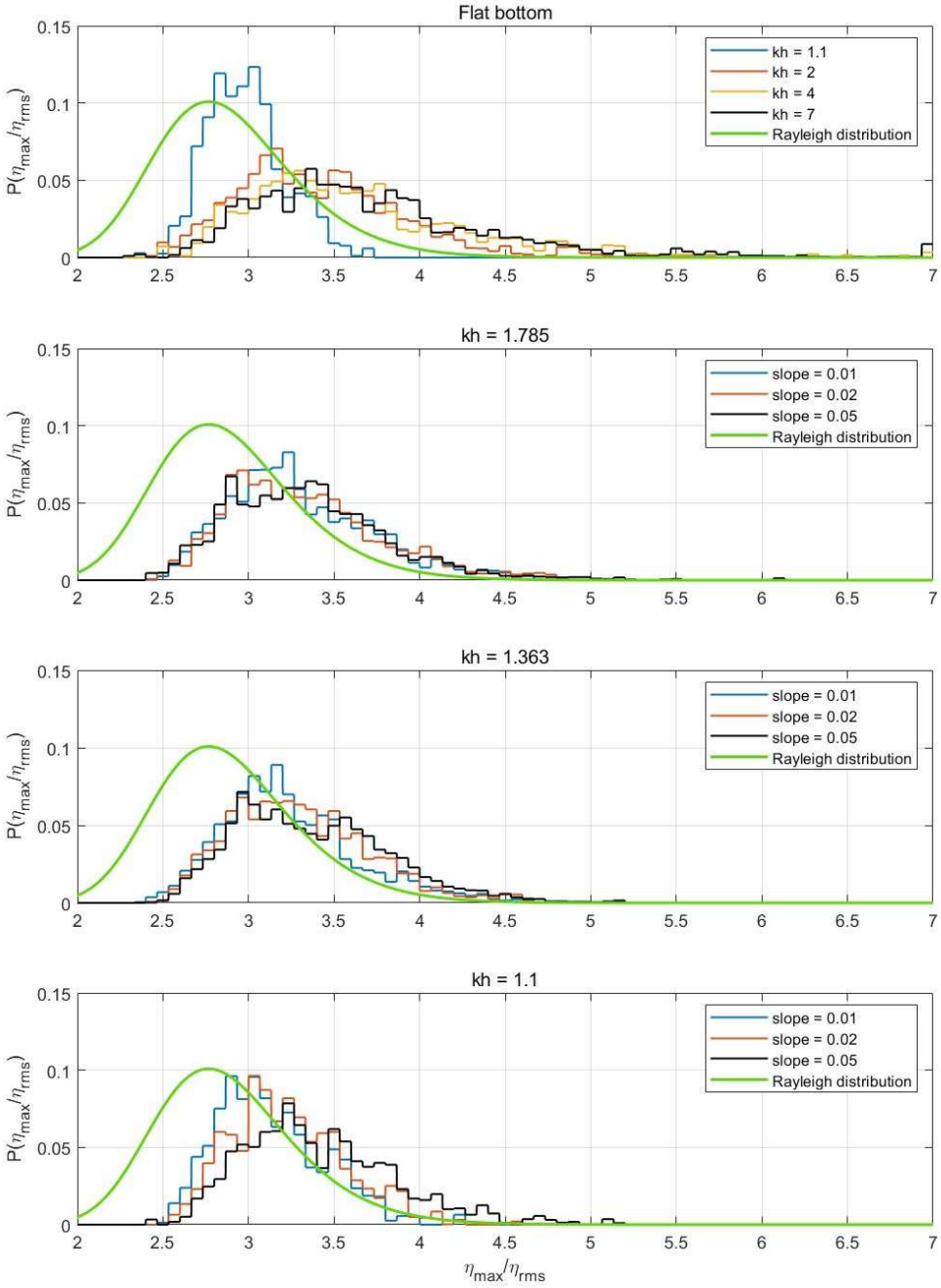

(b) Maximum free surface elevation $\eta_{\max}$

Figure 3.22 Probability Density Function of wave height and free surface elevation distribution, initial BFI = 0.75

3.5 Summary

The nonlinearity analysis of high-order wave evolution is considered as effective approach in freak wave study. Quasi-resonant four-wave interaction has been proved to be related maximum wave distribution, which can be reflected in numerical result from NLS equation. Based on Monte Carlo simulation about 1-D NLS equation with bottom topography change by pseudo spectral method, we discuss the evolution process of wave moment and wave height distribution for narrowband unidirectional wave train. The result indicates:

A) Dimensionless fourth moment kurtosis reflects the nonlinearity in wave train from fourth-order cumulant, and it monotonically decreases from deep-water depth to shallow, or smaller initial BFI.

B) Dimensionless third moment skewness is significantly affected by second-order term from wave steepness and shoaling effect. Steep slope leads to higher skewness, especially for large initial BFI.

C) Maximum wave height distribution is mainly decided by kurtosis, and steep slope will increase occurrence probability of extreme value in shallow water.

D) Due to notable deviation in extreme value estimation, distribution of extreme crest height can reflect the non-linear effect more than wave height. Wave height cannot be simply considered as twice surface elevation in non-linear analysis.

Chapter 4

Numerical Model of Two-Dimensional Directional Modulated Wave Train

4.1 Introduction

For a unidirectional modulated wave train, the occurrence of a freak wave is well predicted by the non-linear wave model about four-wave interaction, which is verified by the wave tank experiment (Mori et al., 2007; Kashima & Mori, 2019; etc.). Numerical work in **Chapter 3** supplemented the freak wave analysis with the consideration of spatial inhomogeneity from bottom topography.

However, when directional behaviors are taken into consideration in a 2D wavefield, recent work pointed out that four-wave interaction decreases due to the directional dispersion effect. The maximum wave height in a directional wavefield decreases compared with the unidirectional wave in the numerical simulation through the mNLS equation in Gramstad and Trulsen (2007). The enhancement of kurtosis is significantly suppressed by the increase of directional spread in the directional wave experiments in Waseda (2006), Onorato et al. (2009a), and Onorato et al. (2009b). Based on the contribution from the directional bandwidth in the directional spectrum, Mori et al. (2011) gave the theoretical estimation of kurtosis for directional sea states, and the occurrence probability of freak wave can be predicted by the fourth-order cumulant and directional spread. The dispersion from the directional effect on four-wave interaction is reflected in Eq. (1-9).

In order to further investigate the non-linear modulated wave evolution in an uneven bottom, this study aims to expand the wave evolution model for unidirectional wave train in

Chapter 3 into a 2D wavefield. The 2D mNLS equation for the uneven bottom in **2.3.2** is applied in the numerical simulation. In a 2D wave basin, we consider the directional dispersion effect as part of the initial value problem and improve the setting of bottom topography in the wave evolution. Monte-Carlo simulation is conducted to give the evolution of nonlinearity and the distribution of extreme events in two-dimensional space-time (2D+T).

4.2 Methodology

4.2.1 2D mNLS equation for an uneven bottom

For a two-dimensional flow field, we continue to assume the flow is irrotational, inviscid, and incompressible with a free water surface. A coordinate system (x, y, z) is defined with origin O as shown in **Figure 4.1**. Plane Oxy is defined along the quiescent water surface, and z axis is defined vertically upward direction, opposite to gravity acceleration g. An incident directional random wave train comes from an external field, and its principal wave direction is along the x axis. The bottom $z = h(x, y)$ mainly varies in the principal direction in the region between dashed line A and B. Velocity potential Φ and free surface elevation η are defined as $\Phi = \Phi(x, y, z, t), \eta = \eta(x, y, t)$ where t represents time.

To simplify the problem and concentrate on the inhomogeneity in a carrier wave propagating direction, we assume the water depth h varies slowly on the wave propagating direction: $h'(x) \sim O(\varepsilon^2)$ and $h'(y) = 0$ where ε is a small constant equaling to the wave steepness. The governing equations and boundary conditions are the same as Eq. (2-1) to Eq. (2-6), and the dispersion relation of ω_0, k, h on the principal wave direction is given in Eq. (2-7). We apply the variable substitution in **2.3.2** from (x, y, t) into (ξ, ζ, τ) for an uneven bottom, and give the evolution equation of envelope $\bar{A}(\xi, \zeta, \tau)$ for a very mild slope in the form of:

$$\mathrm{i}\beta_h \bar{A} + \mathrm{i}\frac{\partial \bar{A}}{\partial \xi} + \beta_t \frac{\partial^2 \bar{A}}{\partial \tau^2} + \beta_y \frac{\partial^2 \bar{A}}{\partial \zeta} = \beta_n \left|\bar{A}\right|^2 \bar{A}, \qquad (4-1)$$

where

$$\beta_h = \frac{(1-\sigma^2)(1-kh\sigma)}{\sigma + kh(1-\sigma^2)} \frac{d(kh)}{d\xi} = \frac{1}{2c_g} \frac{\mathrm{d}(c_g)}{\mathrm{d}\xi}, \qquad (4-2)$$

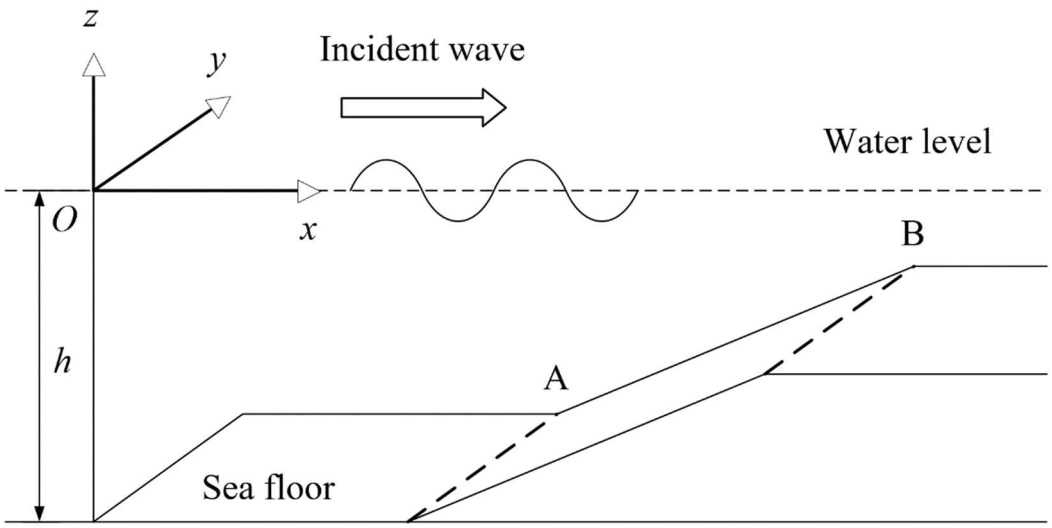

Figure 4.1 Sketch of the wave propagating over an uneven bottom in a 2D wavefield

$$\beta_t = -\frac{1}{2\omega_0 c_g}\left[1-\frac{gh}{c_g^2}(1-\sigma^2)(1-kh\sigma)\right], \tag{4-3}$$

$$\beta_y = \frac{1}{2k}\frac{\partial\omega}{\partial k} \equiv \frac{c_g}{2k}, \tag{4-4}$$

$$\beta_n = k^2\omega_0\left[\frac{1}{16}(9-10\sigma^2+9\sigma^4)-\frac{1}{2\sinh^2 2kh}\right] + \left[\frac{\omega_0^3}{g}\frac{1}{2g}(\sigma^2-1)+\frac{k}{c_g}\right]\left(\frac{c_g^2}{c_g^2-gh}\right)\left[\frac{g^2k}{2\omega_0 c_g}+\frac{\omega_0^2}{4\sinh(kh)^2}\right]. \tag{4-5}$$

4.2.2 Numerical solution and directional effect

In **3.2**, we give the numerical solution of the mNLS equation for the unidirectional wave train. For a 2D problem, we need to eliminate the additional second-order partial differential term of ζ. Based on the periodicity on time and space for a 2D wavefield, the 2D Fourier transform is applied to transform Eq. (4-1) into an ordinary differential equation:

$$\frac{\mathrm{d}\bar{A}}{\mathrm{d}\xi} = -\mathrm{i}\beta_n\left|\bar{A}\right|^2\bar{A} - \mathrm{i}\beta_t\omega_\tau^2\bar{A} - \mathrm{i}\beta_y k_\zeta^2\bar{A} - \beta_h\bar{A}, \tag{4-6}$$

where we take the Fourier transformation twice for τ and ζ on time and lateral length, and ω_τ and k_ζ represent corresponding variables about the frequency and the lateral wave number in the Fourier transform:

$$\dot{A}(\omega_\tau, \xi, \zeta) = F\left[\bar{A}(\tau, \xi, \zeta)\right], \tag{4-7}$$

$$\ddot{A}(\omega_\tau, \xi, k_\zeta) = F\left[\dot{A}(\omega_\tau, \xi, \zeta)\right]. \tag{4-8}$$

Through the spatial evolution of ξ in Eq. (4-6), wave envelope can be numerically simulated from an initial condition at $\xi = \xi_0$ as **3.2.2**. We assume the initial Fourier amplitude $\ddot{A}(\omega_\tau, \xi_0, k_\zeta)$ satisfies the 2D Gaussian shape directional spectral:

$$\ddot{A}(\omega_\tau, \xi_0, k_\zeta) = \ddot{A}(\omega_\tau, \xi_0, \theta_\zeta)$$

$$= \frac{a}{2\pi\sigma_\omega\sigma_\theta}\exp\left\{-\frac{1}{2}\left[\left(\frac{\omega_\tau - \omega_0}{\sigma_\omega}\right)^2 + \left(\frac{\theta_\zeta - \theta_0}{\sigma_\theta}\right)^2\right] + \psi\right\}, \tag{4-9}$$

$$\sigma_\omega = \omega_0 * \sigma_s, \tag{4-10}$$

Where a represents amplitude scale, θ_ζ = arctan $(\frac{k_\zeta}{k_0})$ represents the direction of a single wave with the lateral wave number k_ζ, k_0 and ω_0 are carrier wave number and frequency, σ_ω is frequency spectral width and $\sigma_\omega = \omega_0 * \sigma_s$, σ_θ is dimensionless directional width, ψ is the phase randomly distributed at $[0,2\pi]$. θ_0 is the principal wave direction, and here we set θ_0 is fixed at $\theta_0 = 0$. Referring to Eq. (1-3), the initial BFI value is decided by the ratio between ε and σ_s.

Based on the above settings, we deal with the wave simulation as an initial value problem in **Chapter 3**. The difference is that the initial value is in the 2D matrix for time t and spatial distribution on lateral length y. On principal wave propagation direction, we can solve the wave envelope A at each spatial step on x through Eq. (4-6), and give the wave surface elevation η by Eq. (2-58).

This numerical model also allows us to consider the oblique wave case with a small oblique angle. If we assume the principal wave propagation direction θ_0 satisfies

$$\tan\theta_0 = \frac{k_y}{k_x}, \tag{4-11}$$

where k_x is the component of carrier wave number k_0 on x direction, and k_y is the component on y direction, and

$$k_0 = \sqrt{k_x^2 + k_y^2}, \tag{4-12}$$

then $k_0 \approx k_x$ when $\tan\theta_0 \sim O(\varepsilon)$. We can approximately think the evolution of $\bar{A}$ can still

be described by Eq. (4-1), and the wave surface elevation is given by:

$$\eta(x,y,t) = \varepsilon \mathrm{Re}\left[\frac{1}{2}\bar{A}\exp\left(\mathrm{i}((k_x x + k_y y) - \omega_0 t)\right)\right] + \varepsilon^2 \mathrm{Re}\left[\frac{k\cosh kh}{8\sinh^3 kh}(2\cosh^2 kh + 1)\bar{A}^2 \exp\left(2\mathrm{i}((k_x x + k_y y - \omega_0 t)\right)\right]. \quad (4-13)$$

The effect from the small oblique angle also gives minor changes in the result. However, our simulation concentrates on a very long scale from offshore to onshore. The small oblique angle may lead to a different shape of wave envelope after long-distance evolution.

In **3.2.2,** we introduced the frequency spectrum peakedness Q_p for the zero-up-cross method as an estimation of spectral bandwidth. Q_p in Eq. (3-21) is defined from frequency spectrum, and the discussion in **Chapter 3** concentrates on the variation in the initial condition from different shapes of the frequency spectrum. For a 2D wavefield, the directional dispersion effect also contributes to the initial condition, so we give the Q_p from the surface elevation distributed on the lateral direction:

$$Q_p = \frac{2\int_0^\infty k_\zeta S(k_\zeta)^2 dk_\zeta}{[\int_0^\infty S(k_\zeta) dk_\zeta]^2}, \quad (4-14)$$

where $S(k_\zeta)$ is the wave spectrum about lateral wave number k_ζ. Q_p in Eq. (4-14) gives the estimation of the width of the directional spectral peak and the evolution of Q_p can be a reference of the degree of directional dispersion in the 2D wavefield.

4.2.3 Model setup

Based on the 1D mNLS model for the unidirectional wave train, we expand the modulated wave evolution model into 2D through the numerical solution in **4.2.2**. The expansion of dimension not only increases the consideration of the nonlinearity on one more direction, but also brings about the complexity in the numerical calculation process.

With the 2D Gaussian shape directional spectral in Eq. (4-9) and inverse Fourier transform, we give the initial envelope $\bar{A}(\tau, \xi_0, \zeta)$ in the matrix of time series and spatial distribution on the lateral direction. As a pseudo spectral method, discrete Fourier transform requires a sufficient length of the target variable to make sure the result keeps enough information in the evolution. On the other hand, Fourier transform for a 2D matrix requires a large amount of time

in calculation compared with the 1D model, which is a critical problem since we apply Monte Carlo method simulation. We need to give an appropriate set of initial parameters to hold on to the accuracy and computational efficiency.

Firstly, we adjust the output resolution in the result to find an optimistic output interval. To ensure the accuracy in the fourth-order Runge-Kutta method, we make the calculation step is constant at $\mathrm{d}\xi = 2\times10^{-5}L_0$ where L_0 is carrier wavelength, and slightly sacrifice the resolution on the lateral direction. We make the wave steepness $\varepsilon = 0.1$, total lateral length $L_y = 25L_0$ temporarily, and give time-series setting the same as **3.2.3**: the carrier frequency $\omega = 2.5\mathrm{s}^{-1}$, and dimensionless spectral bandwidth σ_s varies to give different initial BFI. In **Figure 4.2** and **Figure 4.3**, we give the kurtosis μ_4 and skewness μ_3 from a single sample starting from the same condition at different resolution at BFI = 0.4, $\sigma_\theta = 0.3$, and water depth $kh = 5$. μ_4 and μ_3 in the 2D wavefield is gained from the surface elevation at a fixed point in time series. We consider 8 kinds of lateral resolution from (a) ~ (h): $\mathrm{d}y = 0.0057L_0$, $0.017L_0$, $0.028L_0$, $0.057L_0$, $0.143L_0$, $0.28L_0$, $0.85L_0$, $1.43L_0$, and output the longitudinal result in the same resolution with the lateral. As the resolution becomes rough in **Figure 4.2**, the information keeps complete until **Figure 4.2 (e)**, and **Figure 4.2 (f)** basically keeps key information which is enough for further discussion. In **Figure 4.3**, we can give a similar conclusion for skewness, and we get an approximate range of optimistic $\mathrm{d}y$ around $0.3L_0$.

To further explore the optimistic $\mathrm{d}y$ for a more accurate value and decide the total lateral length L_y, we examine the correlation length by the auto-correlation and cross-correlation function. For a domain in strict-sense stationary (SSS), the statistical properties keep invariant to any shift at any order. In this study, the surface elevation at constant water depth will be generally closed to a zero-mean SSS process when the Monte Carlo simulation for random wave phase has enough ensemble size. Based on the classical surface model in Franceschetti and Riccio (2006), we need to ensure the L_y is longer than the correlation length, then the distribution of surface elevation on the lateral direction can satisfy the zero-mean SSS process. In **Figure 4.3**, we give the normalized auto-correlation coefficient of the surface elevation η at $t = 40T_0$ in the sequence of y on different spatial step $x = 10L_0$, $20L_0$, $30L_0$ with different L_y and $\mathrm{d}y$. At $y = 0$, the auto-correlation coefficient is 1 since it's totally related to itself. As the calculation moves from $x = 10L_0$ to $30L_0$ on the propagation direction, the

difference caused by different $\mathrm{d}y$ gradually accumulates in the result from L_y = $10L_0$ and $20L_0$. In the L_y = $30L_0$, the auto-correlation curve is basically under 0.5, and the result for different $\mathrm{d}y$ is almost the same, which implies L_y = $30L_0$ is long enough in the simulation. In **Figure 4.4**, we give the normalized cross-correlation coefficient of the surface elevation η in different sequences at different $\mathrm{d}y$ with L_y = $30L_0$. Three columns on the left are in time series, and we select $\eta(t)$ at $y = 0$ as the first sequence and $\eta(t)$ at $y = D_y$ as the other sequence at x = 0, $20L_0$, $30L_0$ to give their normalized cross-correlation. The first column from the right is in spatial series, and we select $\eta(x)$ at $y = 0$ as the first sequence and $\eta(x)$ at $y = D_y$ as the other sequence at t = $40T_0$ to give their normalized cross-correlation. The results are basically lower than 0.25, which means the correlation between the two sequences is weak enough. To make the calculation efficient, we choose $L_y = 30L_0$ and $d_y = 0.5L_0$ in Monte Carlo simulation.

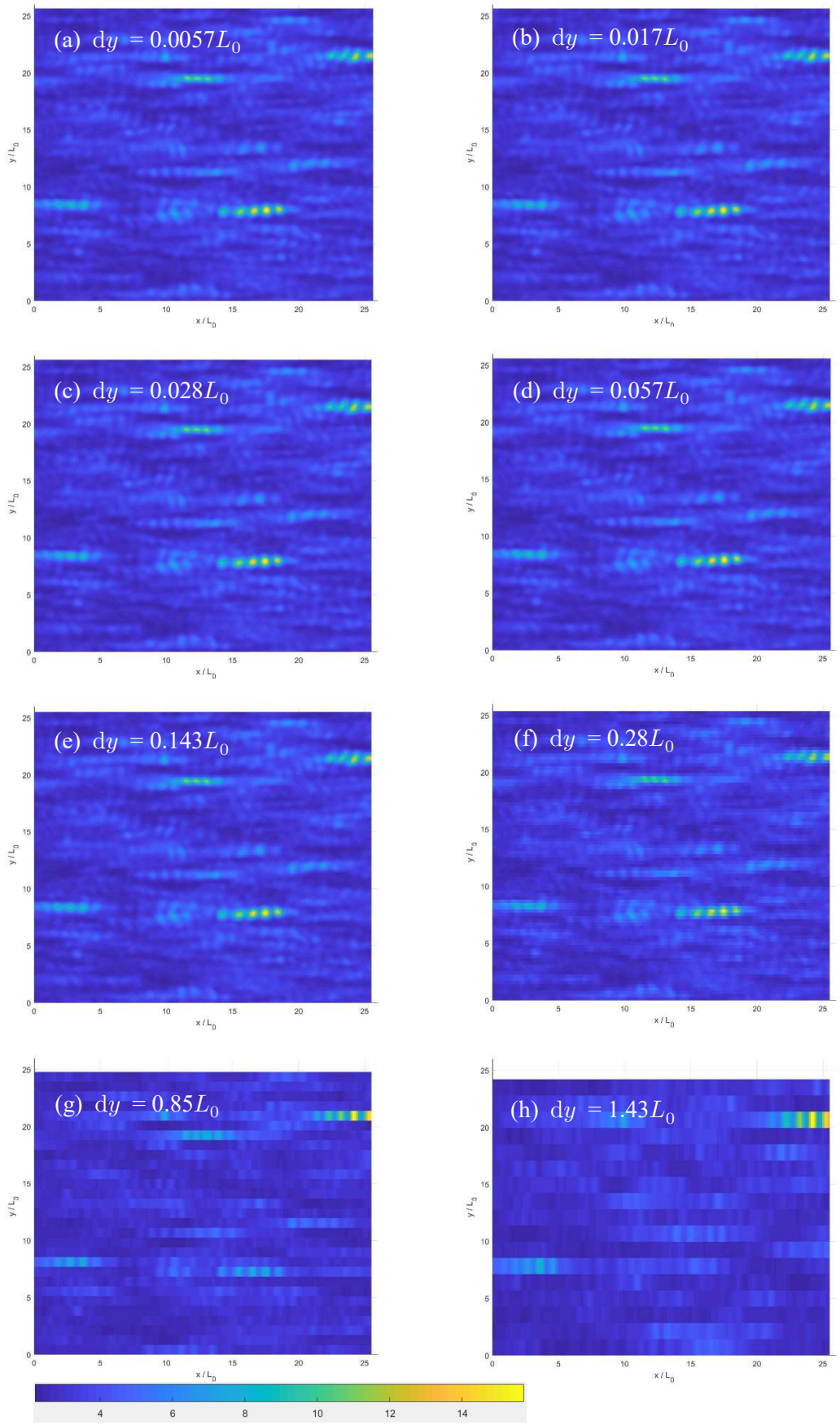

Figure 4.2 Kurtosis from same sample at different resolution at BFI = 0.4, σ_θ = 0.3, kh =5

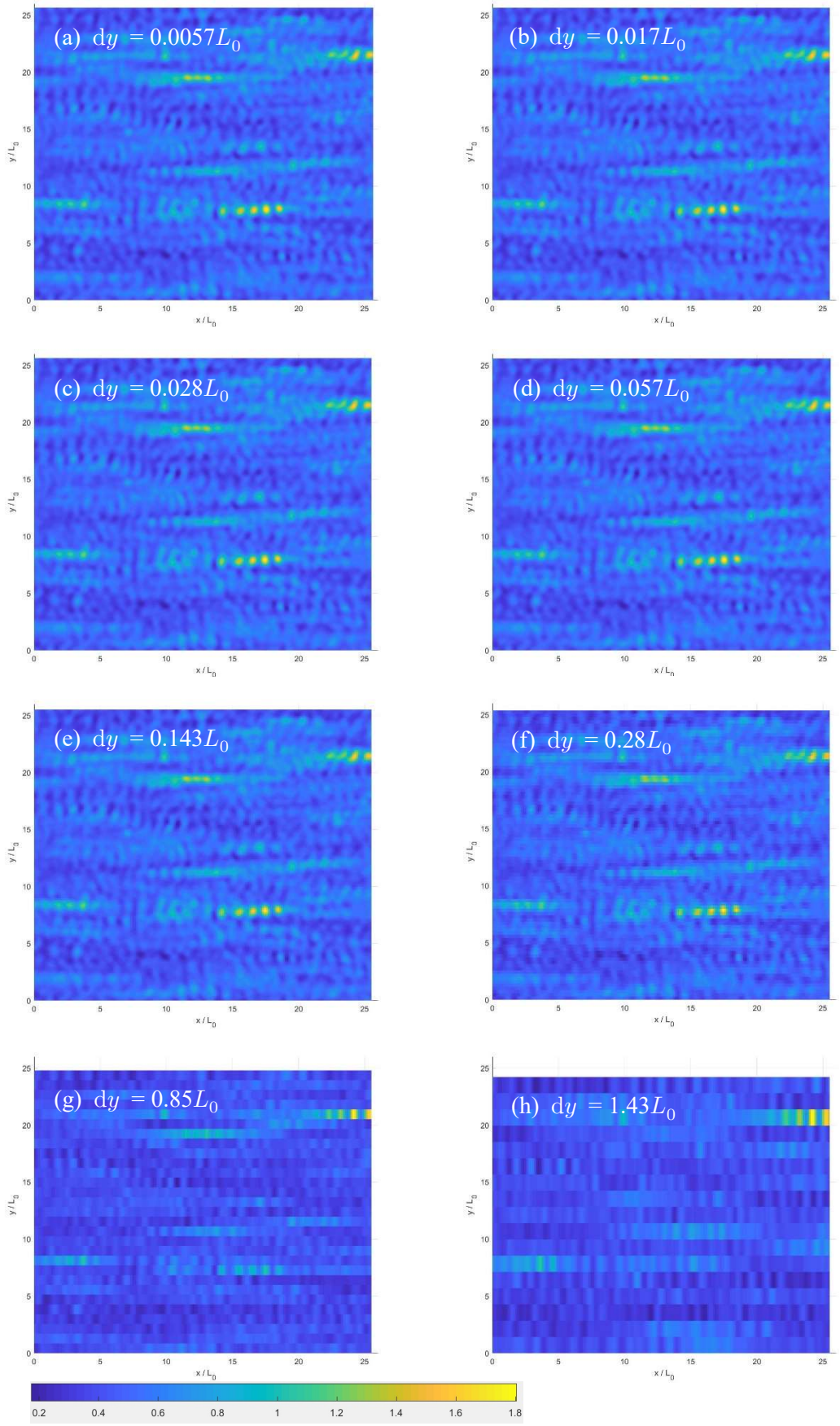

Figure 4.3 Skewness from same sample at different resolution at BFI = 0.4,$\sigma_\theta = 0.3$,$kh = 5$

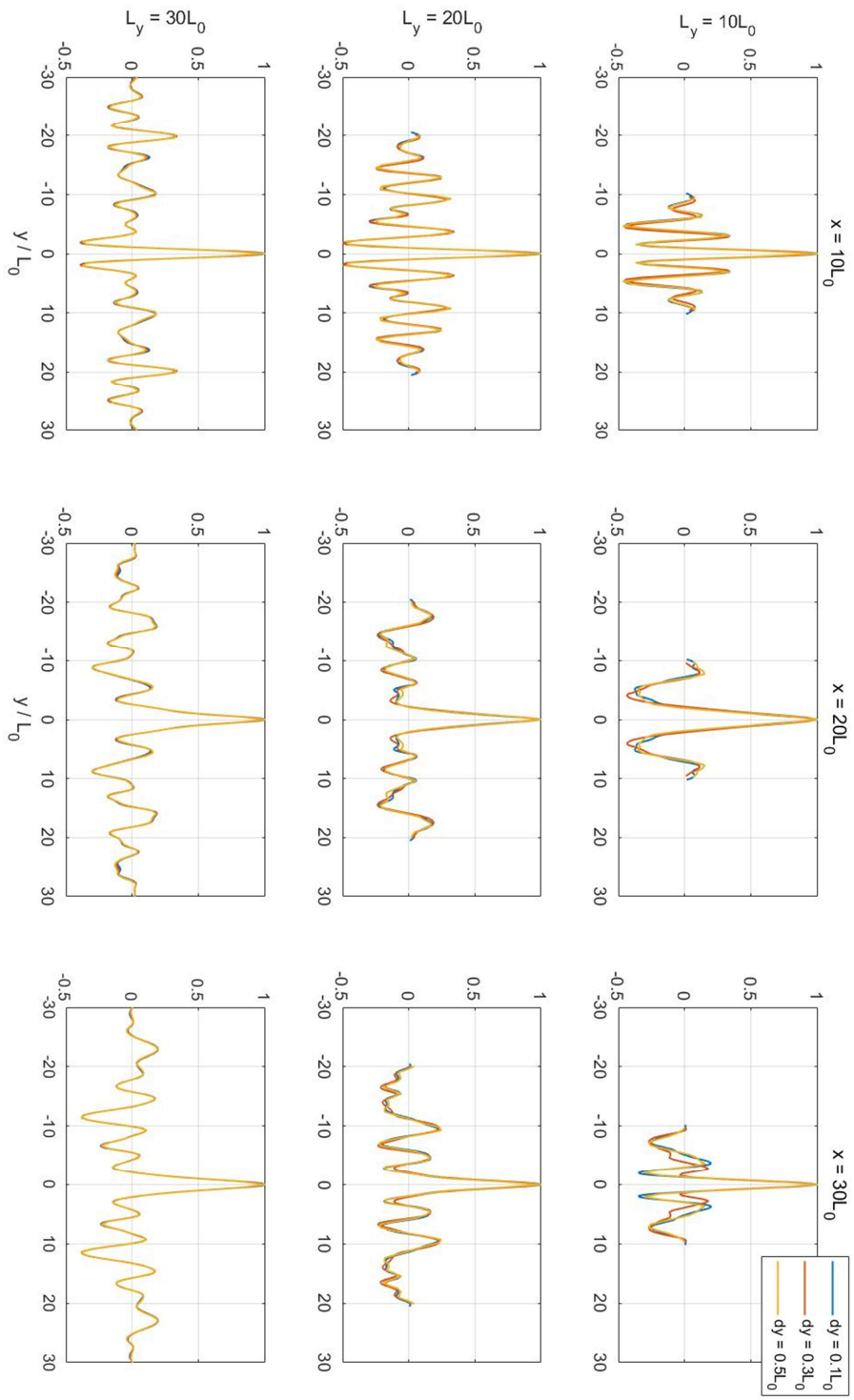

Figure 4.4 Normalized auto-correlation of the surface elevation in the sequence of y on different spatial step with different model setting at $t = 40T_0$

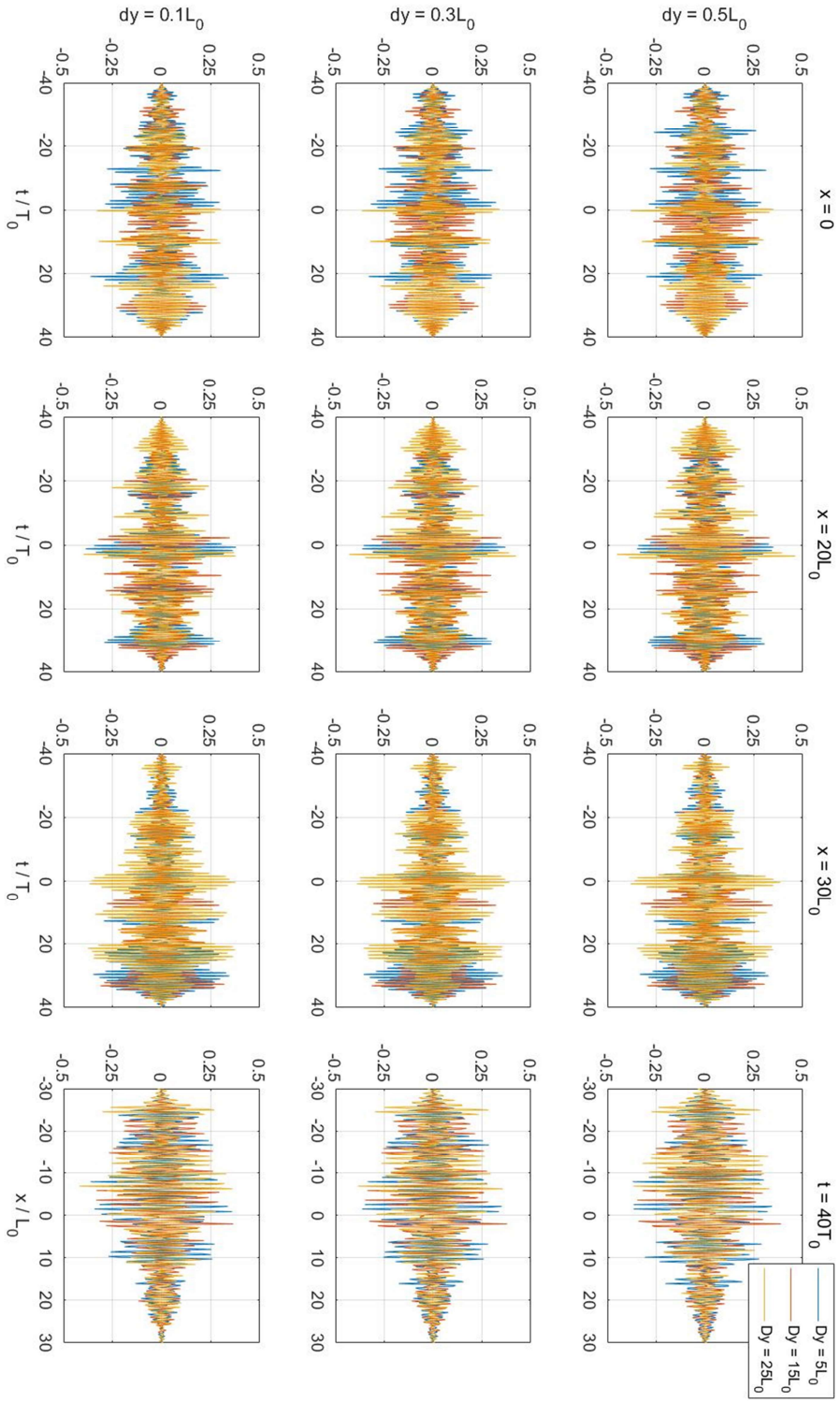

Figure 4.5 Normalized cross-correlation between surface elevation at $y = 0$ and $y = D_y$ in time and spatial series at different sections with different model setting

After finishing the initial setting of the computing environment, we examine the convergence of the Monte Carlo simulation. The same with **3.2.3**, we take the kurtosis μ_4 of surface elevation η as the index and give the average μ_4 of a 2D wavefield from different ensemble sizes M. For an SSS process, the variation in statistical parameter μ_4 from different samples only comes from the random initial phase ψ, and this difference will decrease to zero in the mean value when the ensemble size is large enough. In other words, the mean μ_4 and μ_3 don't change on the lateral direction and only change with the bottom topography. Therefore, the result from the Monte Carlo simulation in this Chapter will be given in 2 forms: 2D distribution in the wavefield (e.g. Figure **4.2** & **4.3**); 1D distribution along the x axis (principal wave direction when $\theta_0 = 0$), where we take the mean value of the lateral direction result and plot them in 1D. In **Figure 4.6**, we give the spatial evolution of μ_4 from different ensemble size M at a 2D flat bottom with kh = 5, initial BFI = 0.4 and σ_θ = 0.5. The result shows, μ_4 is closed to be convergent when $M \geq$ 200, and the improvement from enlarging M is not obvious when $M \geq$ 300. In **Figure 4.7**, we give the variation of mean value and standard deviation of μ_4 with ensemble size M at (x, y) = (20L_0, 15L_0) with kh = 5, initial BFI = 0.4 and σ_θ = 0.5. When $M \geq$ 200, the mean value and standard deviation both become convergent enough. Corresponding results in 2D are given in **Figure 4.8**. In a 2D area, a totally convergent mean value of μ_4 requires a very large ensemble size M, but we think the approximate range of the distribution of μ_4 in $M \geq$ 300 is enough for the following discussion. Therefore, the ensemble size M in Monte Carlo result and statistical analysis in the following part is 300.

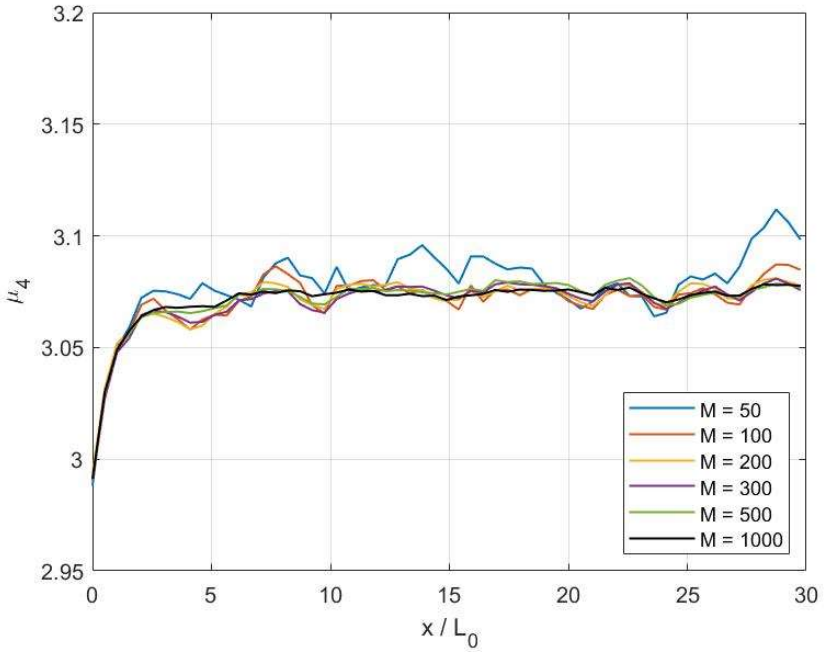

Figure 4.6 Spatial evolution of kurtosis of surface elevation from different ensemble size M at a 2D flat bottom with kh = 5, initial BFI = 0.4 and σ_θ = 0.5

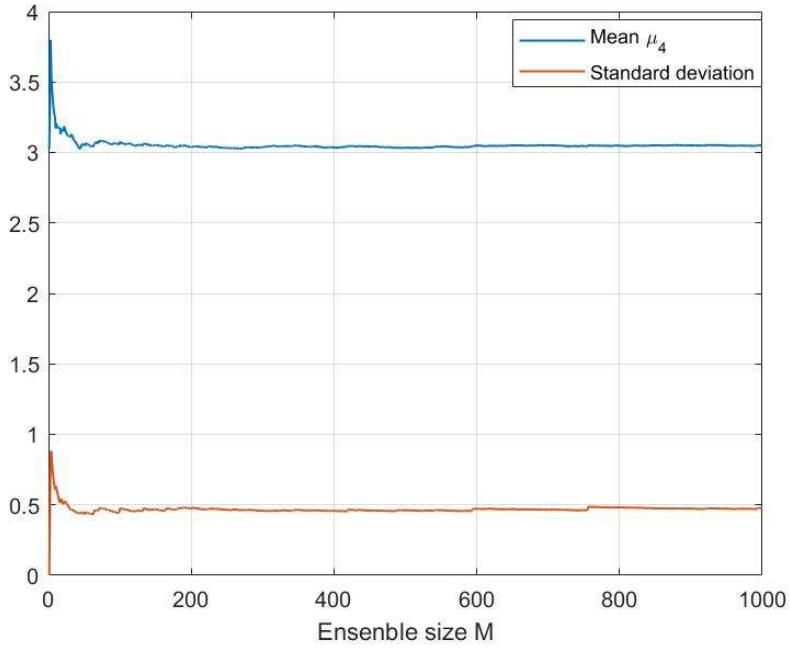

Figure 4.7 Variation of mean value and standard deviation of kurtosis with ensemble size M at (x, y) = ($20L_0$, $15L_0$) with kh = 5, initial BFI = 0.4 and σ_θ = 0.5

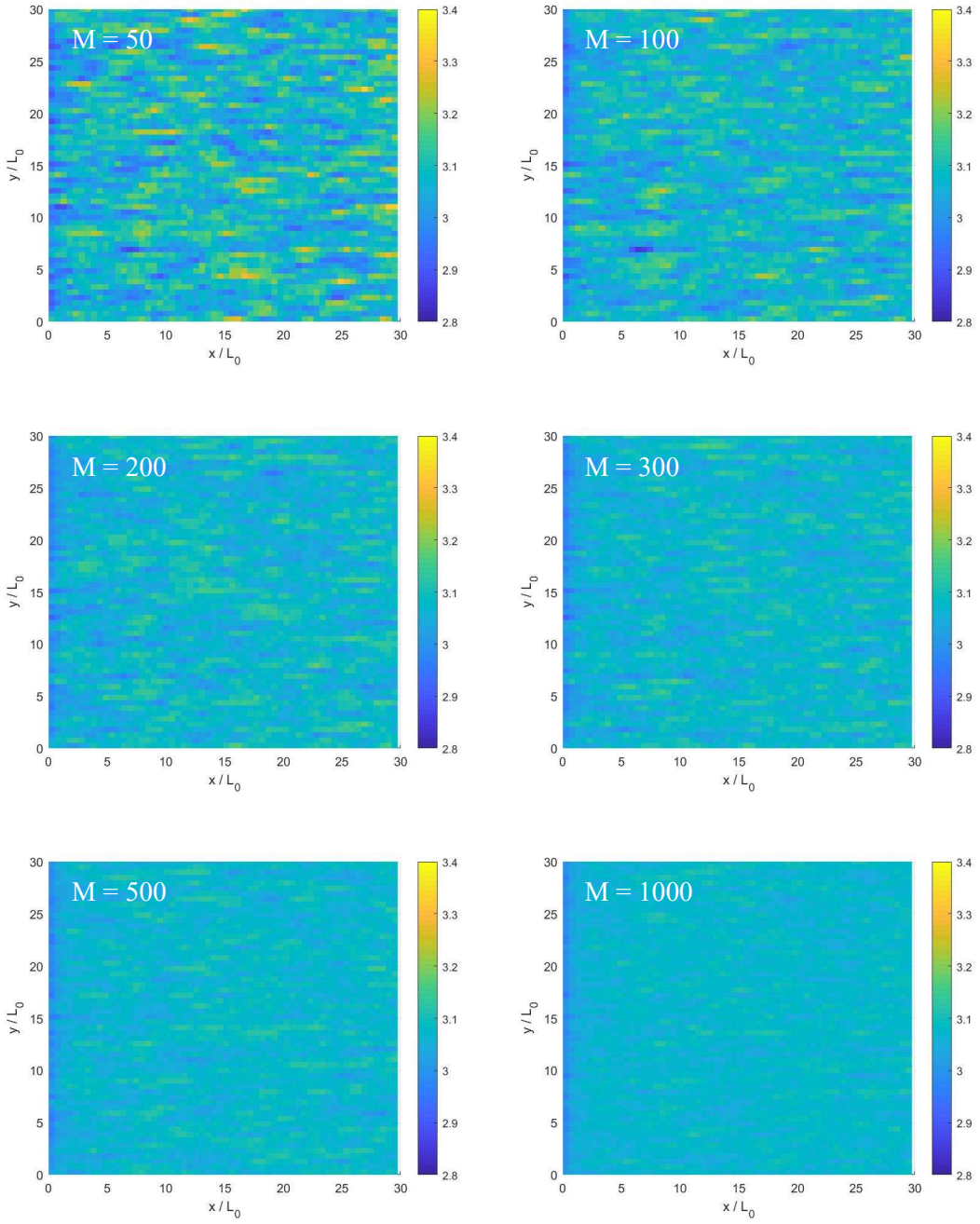

Figure 4.8 Kurtosis of surface elevation from different ensemble size M at a 2D flat bottom with kh = 5, initial BFI = 0.4 and σ_θ = 0.5

4.3 Numerical result

4.3.1 Evolution of modulated wave over a 2D flat bottom

Firstly, we consider the wave evolution over a flat bottom to investigate the effect from initial conditions. From the initial condition given in Eq. (4-9), the shape of the initial directional spectrum is decided by the dimensionless spread σ_θ and the frequency spectral width σ_ω. In **Chapter 3**, the effect from σ_ω has been discussed from the unidirectional wave train with different initial BFI. For a 2D wavefield, the dimensionless spread σ_θ in different sea states varied from 0.15 to 0.5 from the research about observation and wave age (Ewans, 1998; Forristall and Ewans, 1998; Banner and Young, 1994). Yuen and Lake (1982) indicated a limitation of the 2D NLS wave model that the instability of wave train continually increases in a certain interval, which reflects in our numerical model that the result is unable to reach convergence in Monte Carlo simulation when $\sigma_\theta \leq 0.25$. Therefore, we set the σ_θ = 0.3, 0.4, 0.5 in the following comparison for different directional spread, and we make the wave steepness ε = 0.1 the same as the unidirectional wave train study.

In **Figure 4.9**, we give the real surface elevation η at $t = 40T_0$ from three samples with different directional spread σ_θ and initial BFI = 1, kh = 5. With a large initial BFI, the wave train becomes regular and the coherent wave envelope can be easily distinguished by the crest and trough. In **Figure 4.10**, we give the vertical upper view of **Figure 4.9**, and the effect from the directional spread σ_θ reflects in the coherent envelope. As the σ_θ increases, the direction of propagation becomes more divergent, which makes the lateral envelope appear to be discontinuous. **Figure 4.11** and **Figure 4.12** show the surface elevation with initial BFI = 0.4 in the same form. In a lower initial BFI, the coherence and continuity of the wave envelope become more irregular and dispersed, and the directional spread reflects in the lateral direction of the envelope. In the following result, we make the initial BFI = 0.4 and concentrate the effect from different σ_θ.

Figure 4.13 and **Figure 4.14** give the mean value of kurtosis and skewness from different water depth and σ_θ in Monte Carlo simulation at initial BFI = 0.4 in 2D. The left column is

the result at σ_θ = 0.3, and the right is σ_θ = 0.5. As the water depth kh decreases from kh = 5 to kh = 1.1, kurtosis μ_4 decreases when σ_θ = 0.3 but increases when σ_θ = 0.5. It also reflects in the result at the same kh and different σ_θ: for kh = 5 and kh = 3, the μ_4 in σ_θ = 0.3 is larger than σ_θ = 0.5, but the situation becomes the opposite when kh = 1.1. The cause of this phenomenon can be traced back to the conclusion in the unidirectional wave. In deep and mediate water depth, wave trains with higher BFI will show larger μ_4; in shallow water depth, the contribution from higher BFI tends to make μ_4 smaller, but the increasing trend of μ_4 caused by the second-order effect from the bound wave is more significant. From Eq. (1-9), the increase of the directional spread σ_θ can be understood as the decrease of BFI to some extent. Therefore, σ_θ also gives different effect on μ_4 through four-wave interaction depending on water depth. A similar result can be seen in skewness μ_3 in **Figure 4.14**. μ_3 mainly reflects the second-order effect, so the increase in shallow water depth is more significant, and the contribution from σ_θ is relatively weak.

In **Figure 4.15** and **Figure 4.16**, we give a comparison between the unidirectional wave train and the 2D wavefield. With the same numerical environment in **3.3**, we give the Monte Carlo result with initial BFI = 0.5 for a flat bottom kh = 7 to discuss the effect from the directional spread σ_θ on the principal wave direction. The result in the unidirectional wave train can be regarded as σ_θ = 0. As the σ_θ increases, both kurtosis μ_4 and skewness μ_3 decrease. For the 2D propagation in a directional wavefield, both short-time and long-time behavior of κ_{40} for a narrowband wave train is related to the directional width and frequency width (Janssen and Bidlot, 2009). In freak wave forecasting, we are also interested in the kurtosis distribution at the intermediate stages. Mori et al. (2011) conducted an asymptotic analysis of κ_{40}, BFI and σ_θ by numerical simulation, and give Eq.(1-9) with empirical coefficient α. **Table 4.1** shows the ensemble-averaged result of the expected maximum κ_{40} and mean κ_{40} at $x \in [20L_0, 30L_0]$ from Monte Carlo simulation of the wave model in this study, and gives the empirical coefficient $\alpha_{\max}$ and α_{mean} by Eq.(1-9) for maximum κ_{40} and mean κ_{40}, respectively. Due to different calculation conditions, we give different $\alpha_{\max}$ with Mori et al. (2011) (α_1 = 0.0169), and the expected maximum κ_{40} is significantly larger than their prediction. Nevertheless, the result from kh = 7 shows that the increase of σ_θ and decrease of BFI lead to the decrease of both maximum and mean κ_{40}, but the change in

empirical coefficient α represents the κ_{40} is not strictly inversely proportional to σ_θ as Eq.(1-9), and the case from different initial BFI will ask for a different α. The α_{mean} for mean κ_{40} at kh = 7 is better than α_{max} to describe the instability of wavefield, and its value is around 0.09~0.14. When the water depth becomes shallow (kh = 5, 3, 1.1), Eq.(1-9) is no longer applicable and α_{mean} and α_{max} significantly decrease. For kh = 1.1, the increase of σ_θ leads to the increase of κ_{40} and α_{mean} seems anomalous. The behavior of κ_{40} further indicates that the surface instability in medium and shallow water can not be predicted by the four-wave interaction as in deep-water. The contribution from water depth becomes important, especially in shallow water, and the simulation over a changing depth can reveal this process in a more effective way.

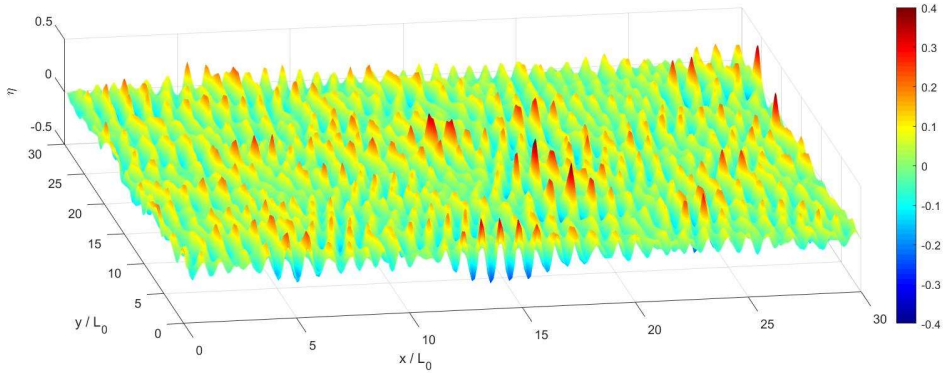

(a) $\sigma_\theta = 0.3$

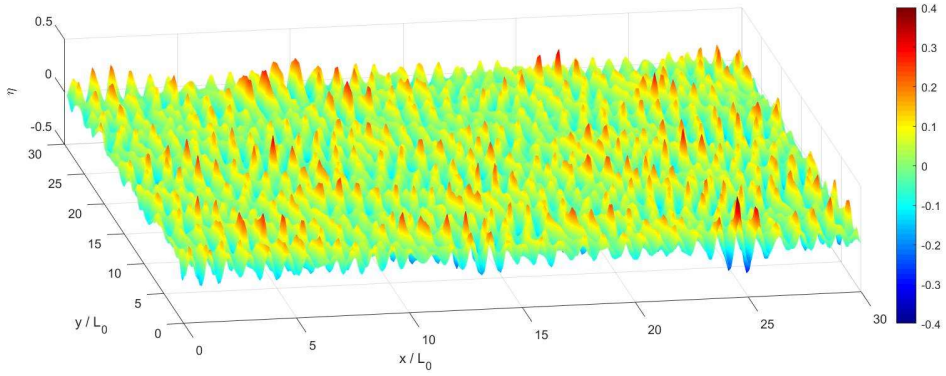

(b) $\sigma_\theta = 0.4$

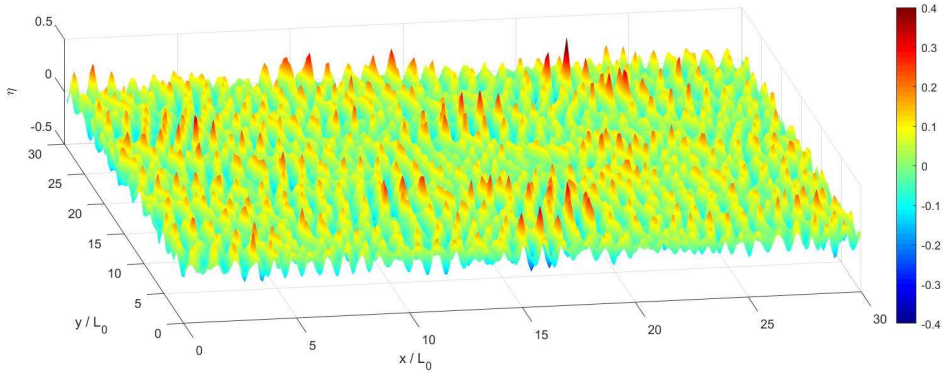

(c) $\sigma_\theta = 0.5$

Figure 4.9 Surface elevation η from single sample at $t = 40T_0$ from different directional spread σ_θ with initial BFI = 1, $kh = 5$

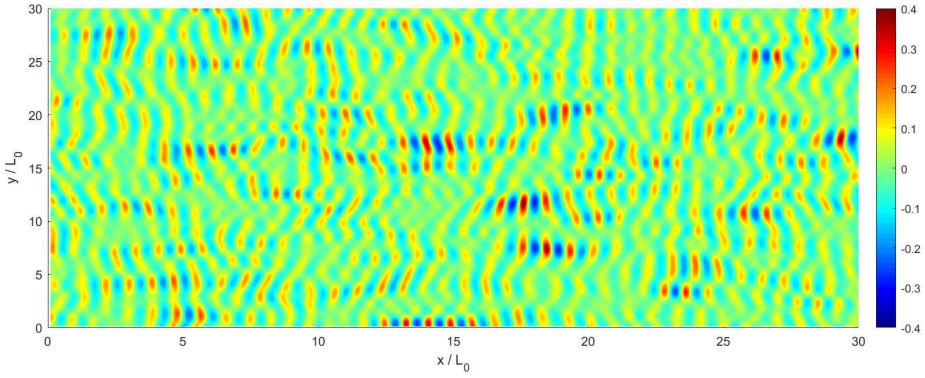

(a) $\sigma_\theta = 0.3$

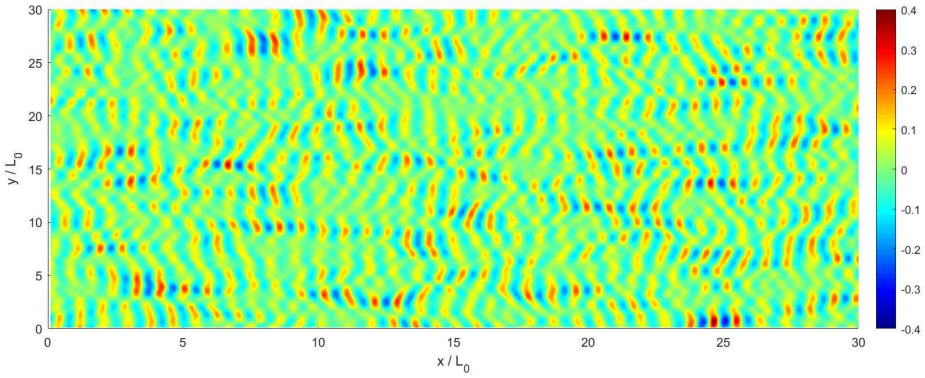

(b) $\sigma_\theta = 0.4$

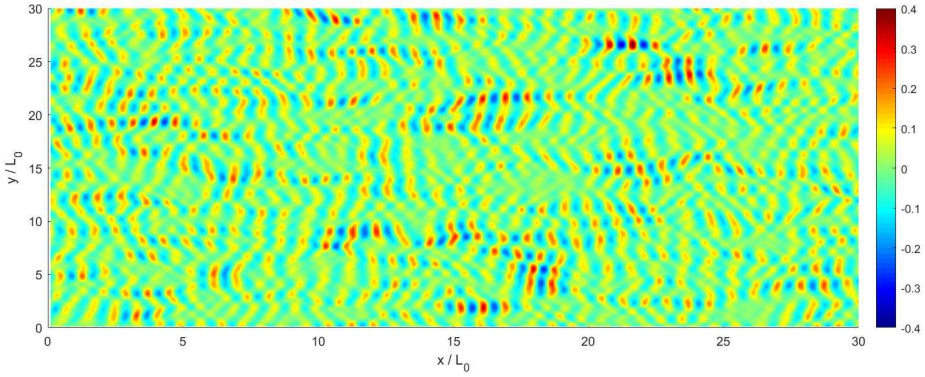

(c) $\sigma_\theta = 0.5$

Figure 4.10 View from above: surface elevation η in **Figure 4.9** at $t = 40T_0$ from different directional spread σ_θ with initial BFI = 1, $kh = 5$

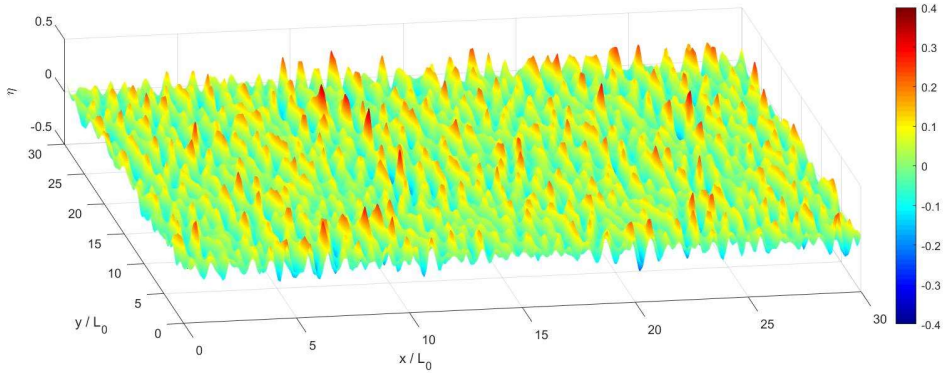

(a) $\sigma_\theta = 0.3$

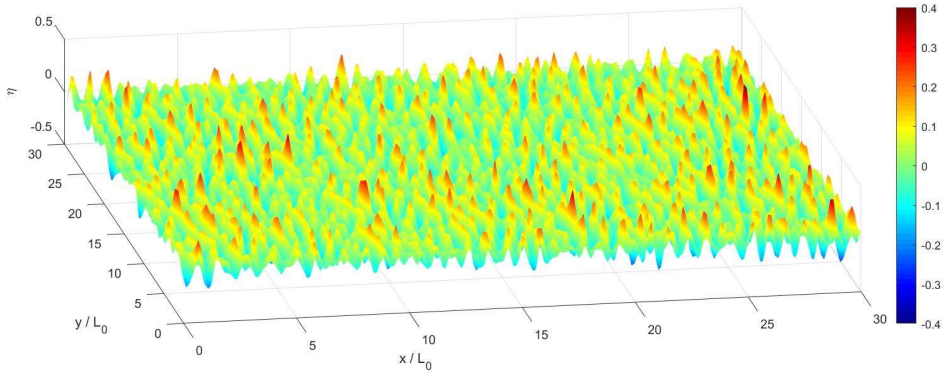

(b) $\sigma_\theta = 0.4$

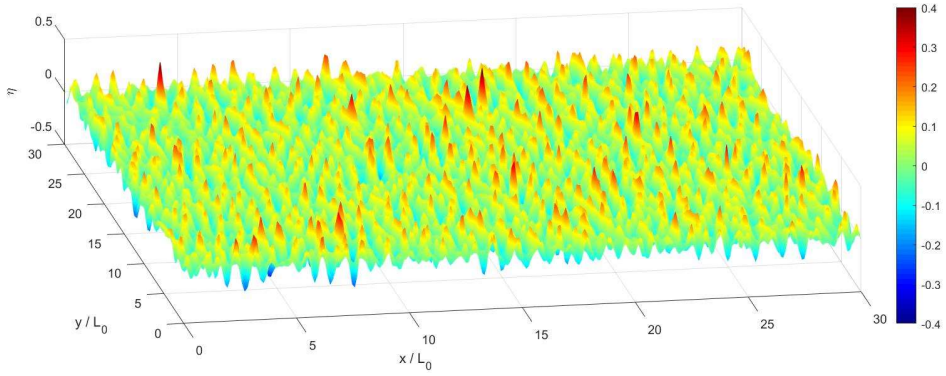

(c) $\sigma_\theta = 0.5$

Figure 4.11 Surface elevation η from single sample at $t = 40T_0$ from different directional spread σ_θ with initial BFI = 0.4, $kh = 5$

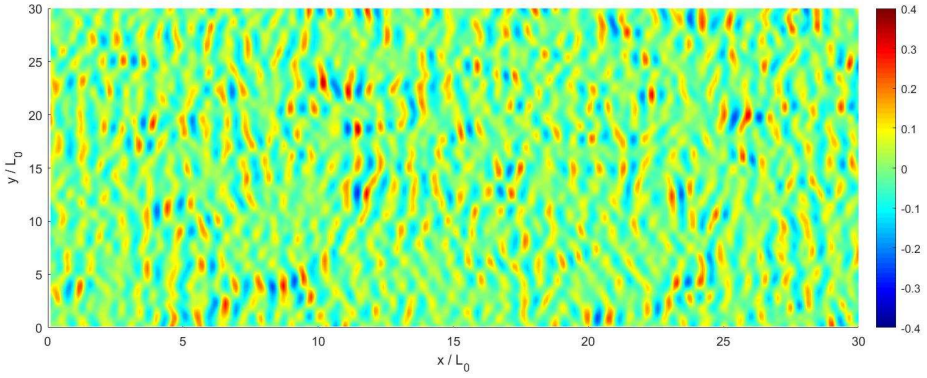

(a) $\sigma_\theta = 0.3$

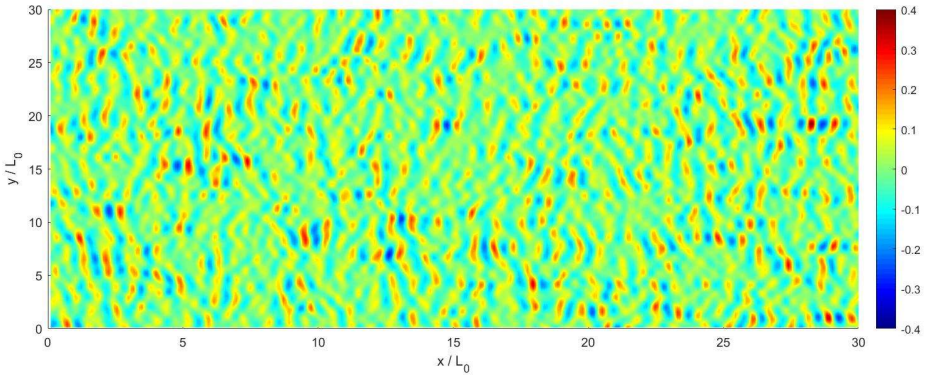

(b) $\sigma_\theta = 0.4$

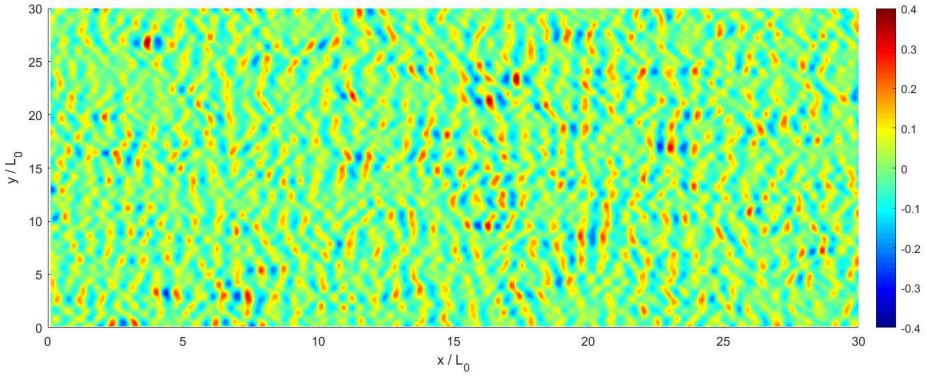

(c) $\sigma_\theta = 0.5$

Figure 4.12 View from above: surface elevation η in **Figure 4.11** at $t = 40T_0$ from different directional spread σ_θ with initial BFI = 0.4, $kh = 5$

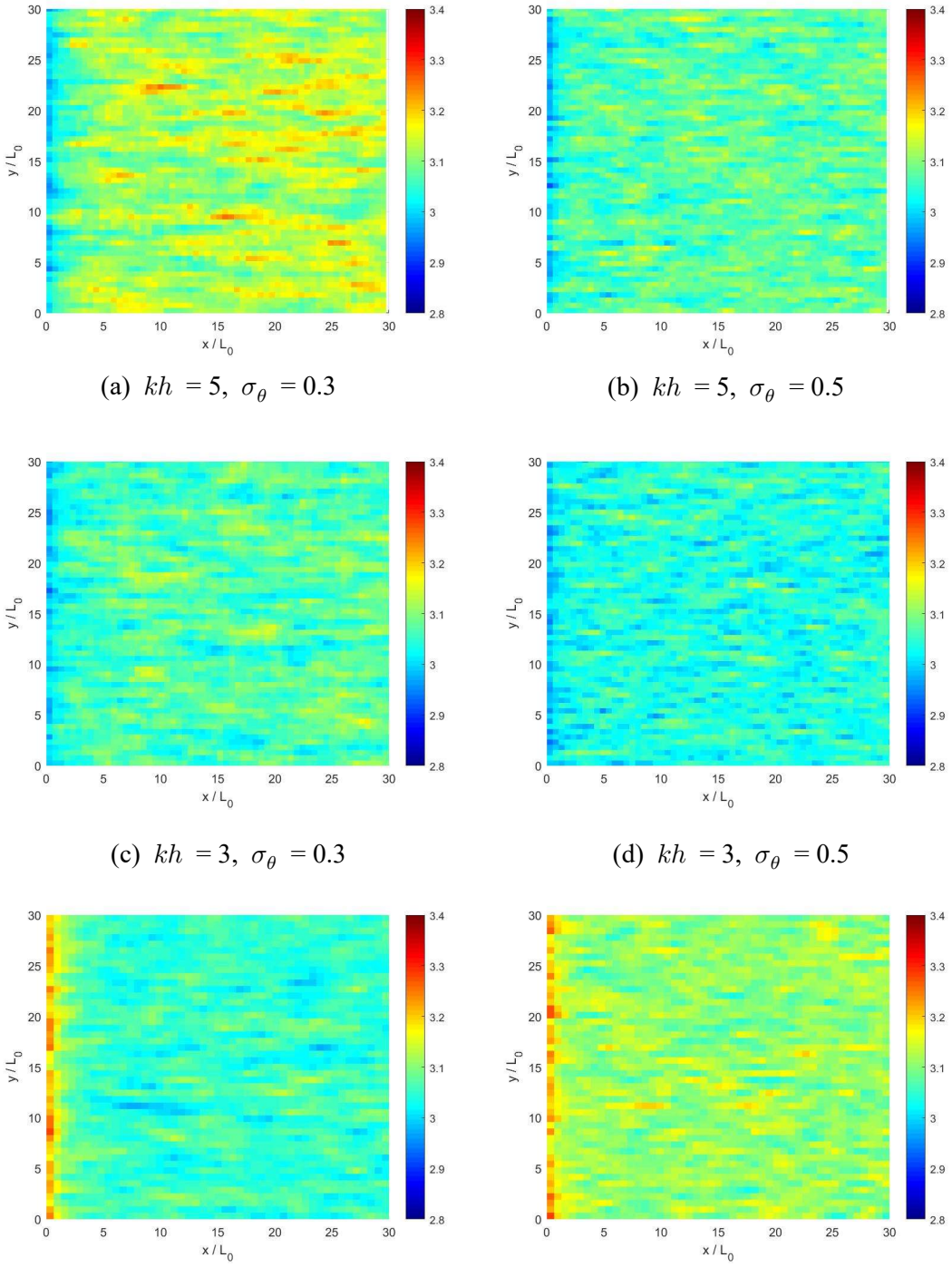

(a) $kh = 5,\ \sigma_\theta = 0.3$ (b) $kh = 5,\ \sigma_\theta = 0.5$

(c) $kh = 3,\ \sigma_\theta = 0.3$ (d) $kh = 3,\ \sigma_\theta = 0.5$

(e) $kh = 1.1,\ \sigma_\theta = 0.3$ (f) $kh = 1.1,\ \sigma_\theta = 0.5$

Figure 4.13 Mean kurtosis of surface elevation in the 2D wavefield at different directional spread and water depth with initial BFI = 0.4

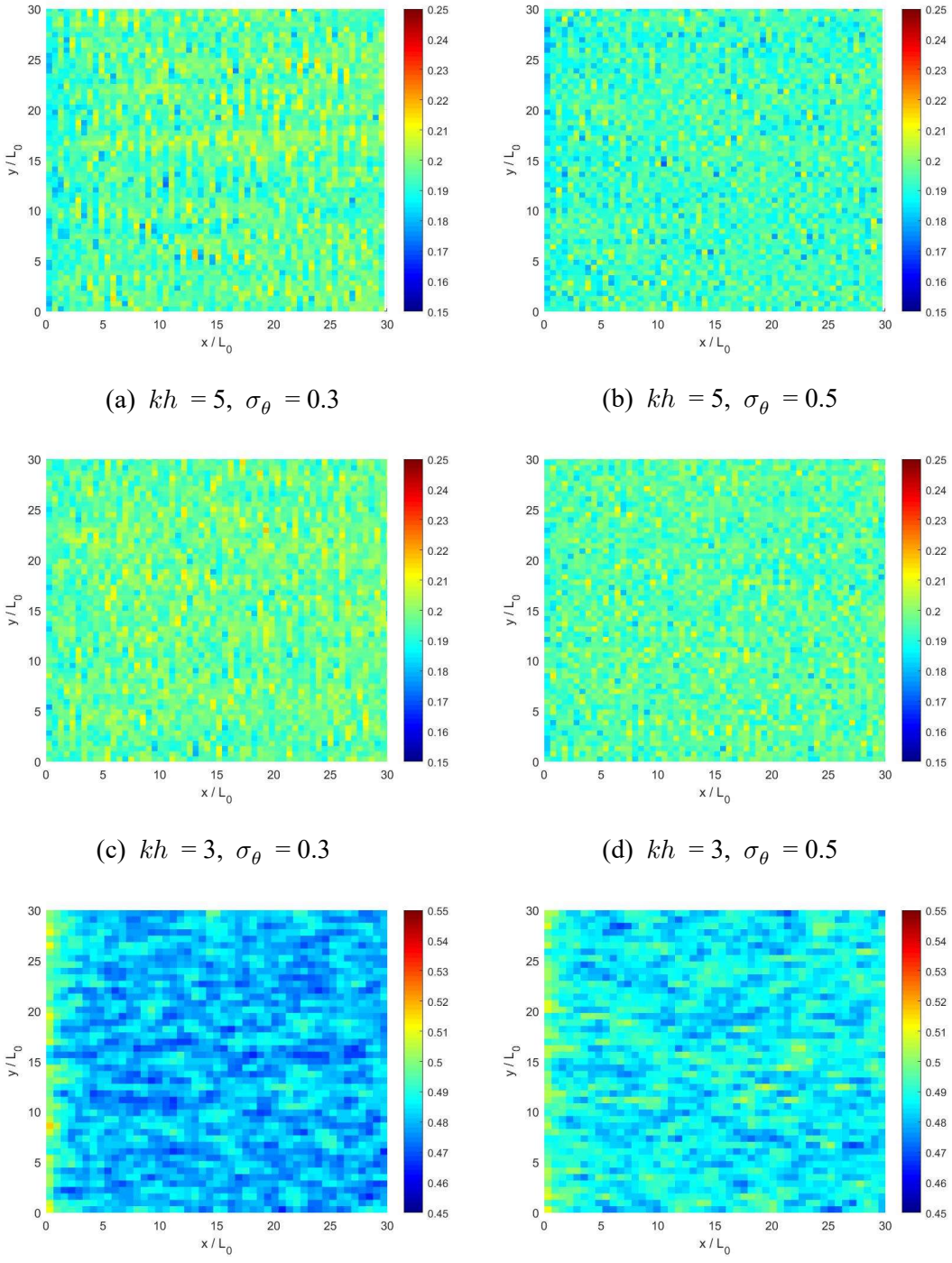

(a) $kh = 5,\ \sigma_\theta = 0.3$ (b) $kh = 5,\ \sigma_\theta = 0.5$

(c) $kh = 3,\ \sigma_\theta = 0.3$ (d) $kh = 3,\ \sigma_\theta = 0.5$

(e) $kh = 1.1,\ \sigma_\theta = 0.3$ (f) $kh = 1.1,\ \sigma_\theta = 0.5$

Figure 4.14 Mean skewness of surface elevation in the 2D wavefield at different directional spread and water depth with initial BFI = 0.4

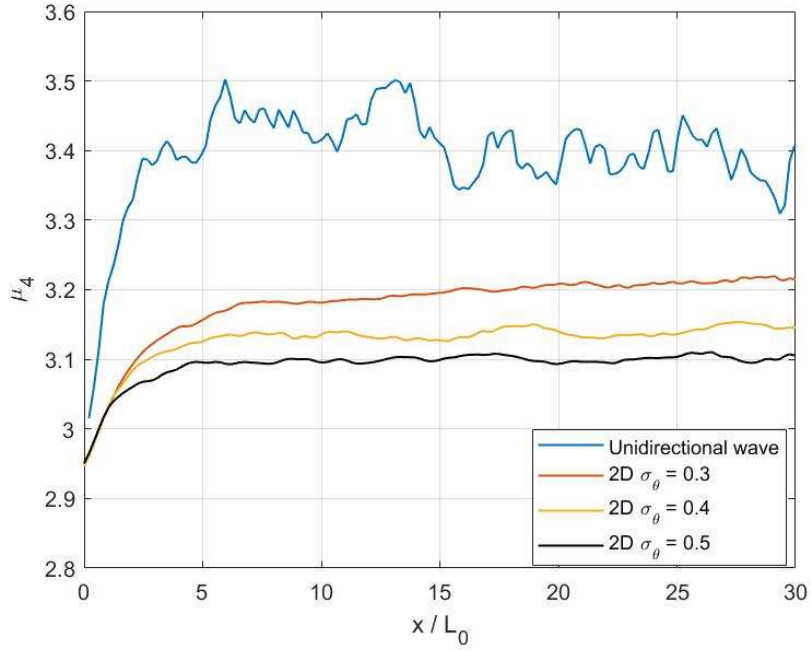

Figure 4.15 Spatial evolution of kurtosis of surface elevation from directional spread σ_θ with initial BFI = 0.5, kh = 7

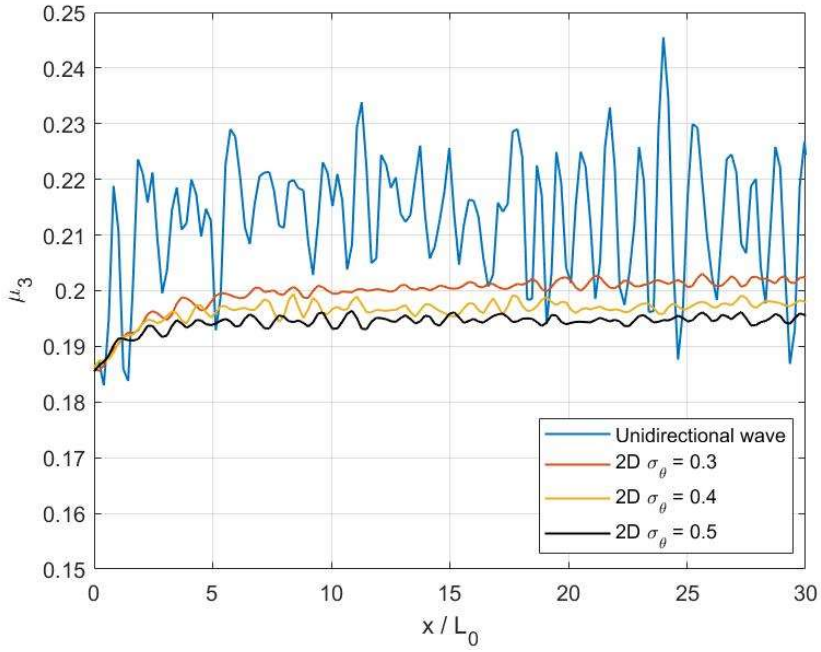

Figure 4.16 Spatial evolution of skewness of surface elevation from directional spread σ_θ with initial BFI = 0.5, kh = 7

Table 4.1 The ensemble-averaged κ_{40} dependence on BFI and σ_θ at different kh

kh	σ_θ	Initial BFI	Max κ_{40}	Mean κ_{40}	$\alpha_{\max}$	α_{mean}
7.0	0.3	0.5	6.329	0.180	4.187	0.119
7.0	0.4	0.5	4.555	0.127	4.018	0.112
7.0	0.5	0.5	4.206	0.092	4.638	0.101
7.0	0.6	0.5	3.841	0.064	5.082	0.085
7.0	0.3	0.4	4.441	0.136	4.591	0.141
7.0	0.5	0.4	3.725	0.083	6.418	0.143
5.0	0.3	0.4	3.976	0.117	4.110	0.121
5.0	0.5	0.4	3.368	0.070	5.803	0.121
3.0	0.3	0.4	3.148	0.065	3.254	0.067
3.0	0.5	0.4	2.948	0.038	5.079	0.066
1.1	0.3	0.4	2.294	0.059	2.371	0.061
1.1	0.5	0.4	2.754	0.113	4.745	0.195

4.3.2 Evolution of modulated wave over 2D uneven bottoms

The discussion about unidirectional wave train in **Chapter 3** indicates that the second-order effect plays an important role in the medium and shallow water depth, and the result in **4.3.1** confirms that a similar conclusion can be derived for the 2D flat bottom. Not only the water depth kh, but also the bottom topography contributes to the wave evolution with the second-order effect in shallow water. To consider the impact from bottom shapes on the non-linear evolution of modulated wave trains in a 2D wavefield, we conduct the Monte Carlo simulation of the 2D wave model for uneven bottoms.

In the numerical model of the unidirectional wave train, the β_h in the evolution equation reaches its maximum at the end of the sloping region in **Figure 3.9**. In a very shallow water depth (kh = 1.1), the gradient of relative depth change $\mathrm{d}h/h$ and the group speed c_g will continue to increase if the slope angle is constant, and it immediately becomes zero when it comes to a flat bottom in the shallow water. In the physical experiment in the wave tank (Kashima and Mori, 2019; Trulsen et al., 2020) and our numerical result in **Chapter 3**, this sudden change contributes to the after-effect. In a 2D wavefield, we find the after-effect will be significantly magnified due to the dispersion effect at the third-order from the directional spread.

To make our simulation closer to the natural seabed, we adjust the sloping region in **Figure 4.1** between A and B to become more smooth and continuously decrease as **Figure 4.17**: the sloping region is divided into 2 parts, where (2) has a constant slope angle and (3) has a changing slope angle generally decreasing to zero. (1) is flat bottom in deep-water and (4) is flat bottom in shallow water. We consider four different bottom shapes which have different lengths of region (2) in **Table 4.2**, where h_s is the water depth at the demarcation point of (2) and (3), and γ_s is a constant slope angle at (2). To make the transition smooth, we set the changing slope is a function of γ_s and the slope at demarcation point C equal to γ_s, which makes the effect from different slope can also be reflected in (3). The topography of the four types of bottom in **Table 4.2** are given in **Figure 4.18**. In B_1 the district (3) is flat, and it is the same as the unidirectional wave model on principal wave direction. From B_1 to B_4, the transition region becomes milder with different value of h_s, and the length of (3) becomes

longer until kh decreases to 1.1 in (4). In **Figure 4.19**, we give the spatial variation of β_h at the transition region from different bottom types with γ_s = 0.05. We can see there is a spike of β_h at the end of (2) in B_1, and it becomes smaller as the bottom change is getting milder. In B_3 and B_4, the variation of β_h is more smooth.

To examine the effect from different bottom types on the wave evolution process, we give the Monte Carlo result of kurtosis μ_4 on uneven bottoms with initial BFI = 0.4, σ_θ =0.3, γ_s = 0.05 in **Figure 4.20**. The result is plotted in 1D on the principal wave direction. As the wave train propagates from deep-water into shallow water, water depth kh decreases from 5 to 1.1. μ_4 decreases with the decrease of kh in deep and medium water but has a rebound at the end of the sloping region. The magnitude of rebound is determined by the bottom types, and we find the rebound will decrease if the bottom topography becomes mild and smooth. However, even the mildest bottom B_4 leads to a non-negligible rebound, which implies the effect from slope angle starts to contribute to the wave evolution in the water depth deeper than kh = 1.363. We apply the bottom type B_3 in the following discussion about the wave evolution over the 2D uneven bottom.

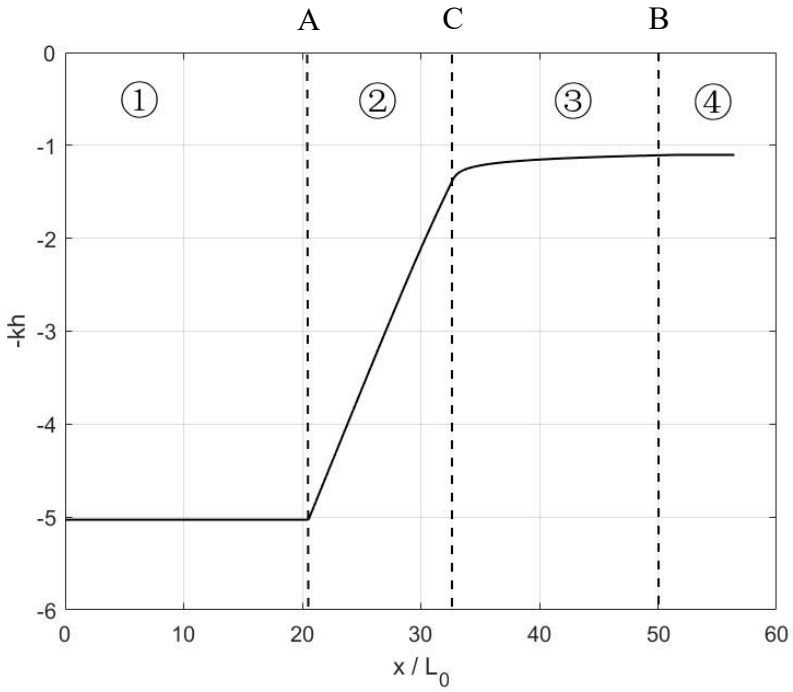

Figure 4.17 Modified uneven bottom topography from deep to shallow water

Table 4.2 Four different bottom topography types

Bottom type	h_s	kh in ①	$h'(x)$ in ②	$h'(x)$ in ③	kh in ④
B_1	1.1	5.0	γ_s	0	1.1
B_2	1.15	5.0	γ_s	$\gamma_s(\frac{h}{h_s})^{40}$	1.1
B_3	1.2	5.0	γ_s	$\gamma_s(\frac{h}{h_s})^{40}$	1.1
B_4	1.363	5.0	γ_s	$\gamma_s(\frac{h}{h_s})^{15}$	1.1

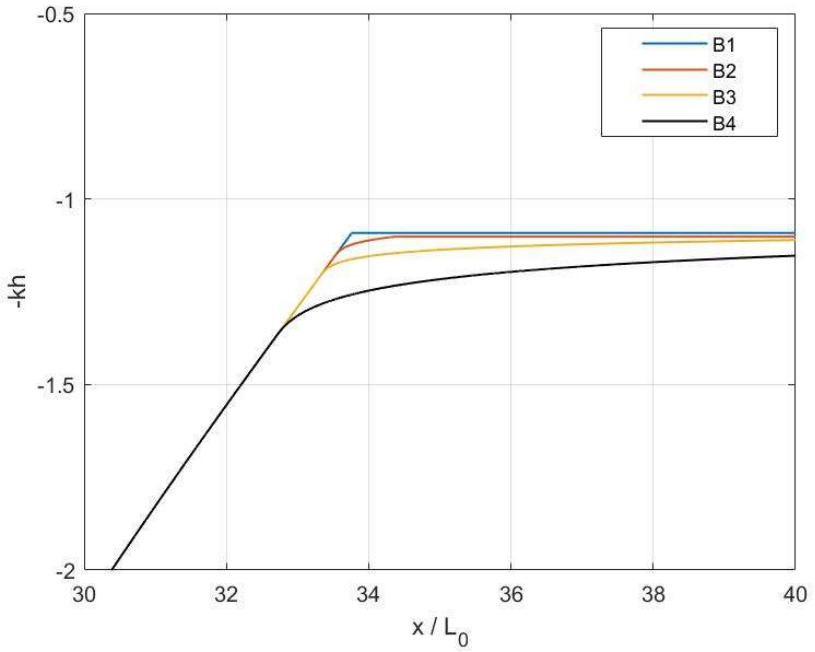

Figure 4.18 Spatial variation of water depth of different bottom types in **Table 4.1**

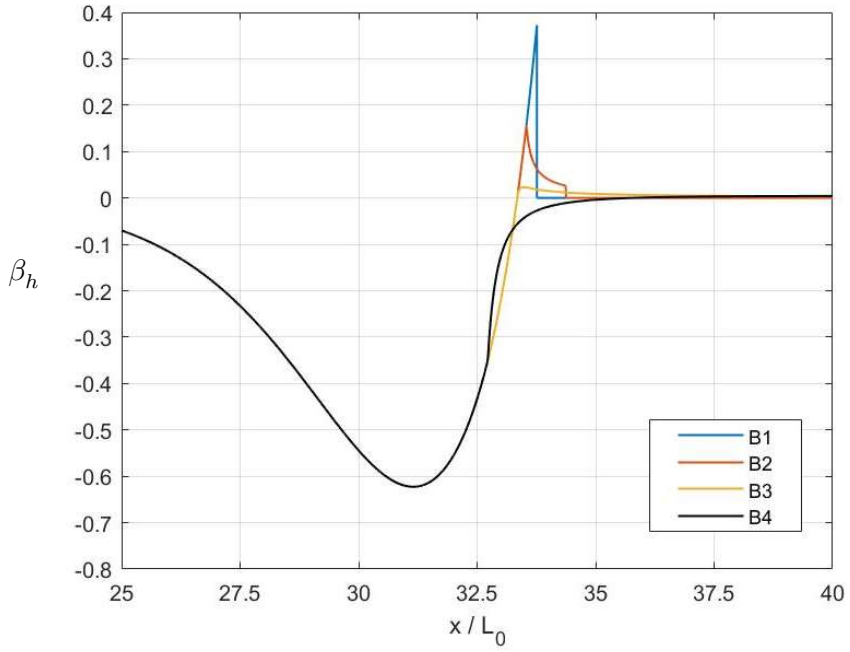

Figure 4.19 spatial variation of β_h of different bottom types in **Table 4.1** with γ_s = 0.05

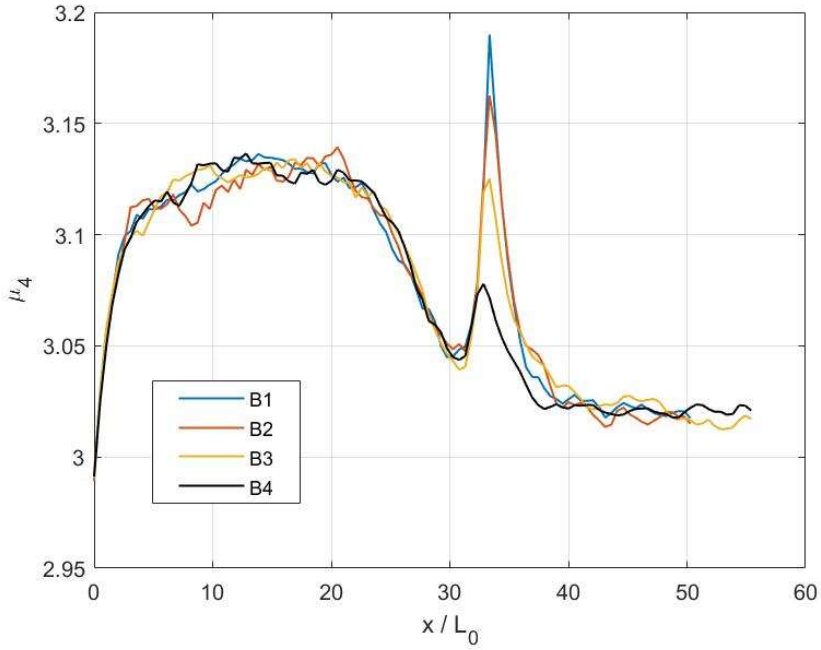

Figure 4.20 Mean kurtosis of surface elevation in Monte Carlo simulation from different bottom types with initial BFI = 0.4, σ_θ =0.3, γ_s = 0.05

From **Figure 4.21** to **Figure 4.23**, we give the mean value from the Monte Carlo simulation of the bottom type B_3. In **Figure 4.21**, we give the mean kurtosis μ_4 in 2D and 1D form at the different directional spread σ_θ and slope angle γ_s with initial BFI = 0.4. Comparing the result from different σ_θ in **Figure 4.21 (a)**, **(b)** and **(c)**, we find the μ_4 decreases in the deep-water depth but increases in the shallow water when σ_θ increases from σ_θ = 0.3 to σ_θ = 0.5, which shows the same phenomenon with the result in a flat bottom in **4.3.1**. In the medium water depth region between A and C, μ_4 decreases as the decrease of water depth, and it rebounds at the end of the constant sloping region where kh = 1.2. In the region between C and B where the slope angle mildly decreases, μ_4 decreases and becomes stable at the same level with the final flat bottom in shallow water kh = 1.1. The evolution of μ_4 indicates that the directional dispersion effect decreases the occurrence probability of freak wave in deep and medium water but increases it in shallow water. As the wave propagates from the medium water to shallow water, the wave evolution is significantly affected by the bottom topography, and the 1D result in **Figure 4.21 (d)** clearly gives the rebound of μ_4 due to the slope angle. To further study the effect from the bottom topography, we give the mean μ_4 at γ_s = 0.02 and γ_s = 0.01 with initial BFI = 0.4 and σ_θ = 0.3 in **Figure 4.21 (e)** and **Figure 4.21 (f)**. The result shows the rebound of μ_4 decreases as the bottom change becomes milder, and **Figure 4.21 (g)** provides the variation of μ_4 on the principal wave direction in 1D. Comparing the μ_4 over uneven bottoms between the unidirectional wave train and the 2D wavefield, we find the slope angle affects the wave evolution in a similar way but its contribution is more significant in 2D due to the dispersion effect on four-wave interaction, which implies the second-order effect plays a more important role in a directional 2D wavefield.

In **Figure 4.22**, we give skewness μ_3 in the same form with μ_4 in **Figure 4.21** at the same condition. Different from μ_4, μ_3 is hardly affected by directional spread from **Figure 4.22 (a)**, **(b)**, **(c),** and **(d)**. When the bottom topography changes, **Figure 4.22 (e)**, **(f),** and **(g)** show the μ_3 increases as the water depth become shallow. This process will slow down if the slope angle becomes mild, but it only means μ_3 is determined by the water depth kh and the change from slope angle γ_s has little influence. Different from the unidirectional wave train, μ_3 in the 2D wavefield is basically only determined by the second-order effect. When the wave

trains propagate into shallow water, the μ_3 increases with the increase of wave steepness ε.

To examine the evolution of the directional spectrum, we give the mean Q_p from Eq. (4-14) at different directional spread σ_θ and slope angle γ_s with initial BFI = 0.4 in **Figure 4.23**. As σ_θ increases from 0.3 to 0.5 in **Figure 4.23 (a)**, **(b)** and **(c)**, the Q_p significantly rises since the directional dispersion increases from the initial condition. With the water depth decreases from deep to shallow, Q_p slowly decreases in each bottom type. The variation of Q_p in the 2D wavefield is similar to the low BFI result in the unidirectional wave in **Figure 3.19**, and the effect from different slope angle is very limited. The decrease of Q_p in shallow water indicates the directional spread will become weak slightly compared with the initial condition.

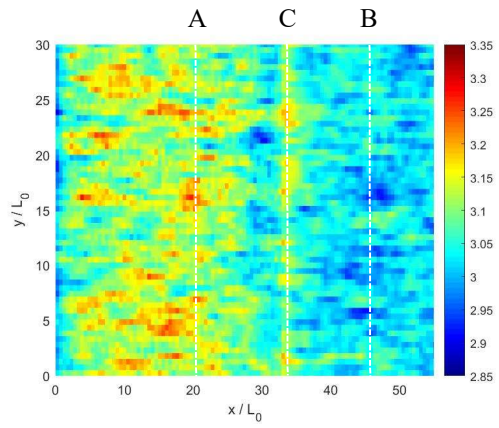

(a) $\sigma_\theta = 0.3,\ \gamma_s = 0.05$

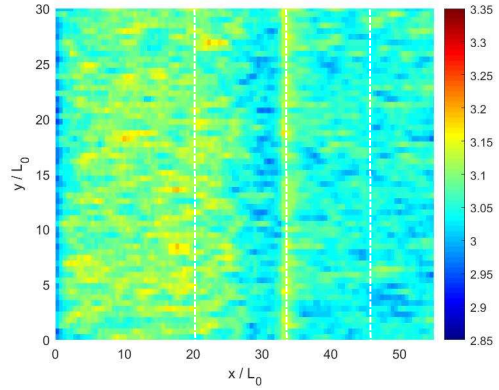

(b) $\sigma_\theta = 0.4,\ \gamma_s = 0.05$

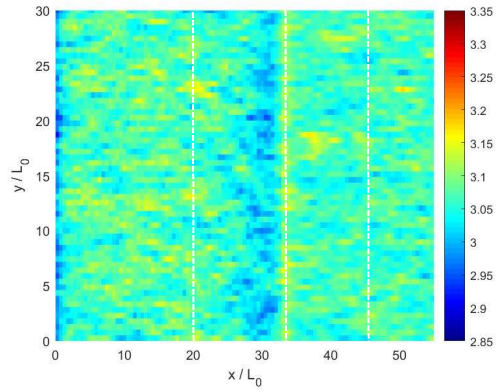

(c) $\sigma_\theta = 0.5,\ \gamma_s = 0.05$

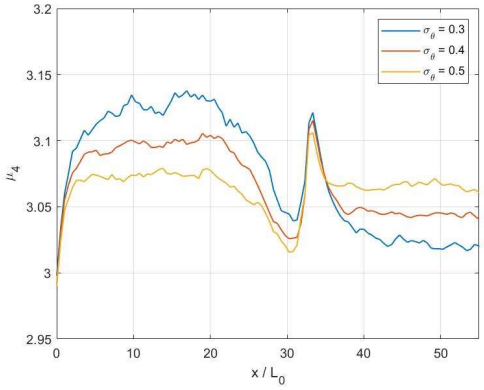

(d) : $\sigma_\theta = 0.3, 0.4, 0.5,\ \gamma_s = 0.05$

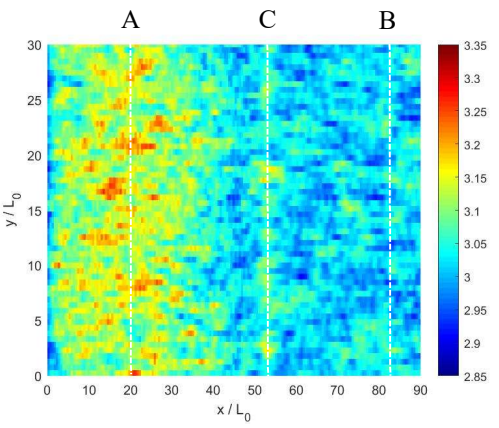

(e) $\sigma_\theta = 0.3,\ \gamma_s = 0.02$

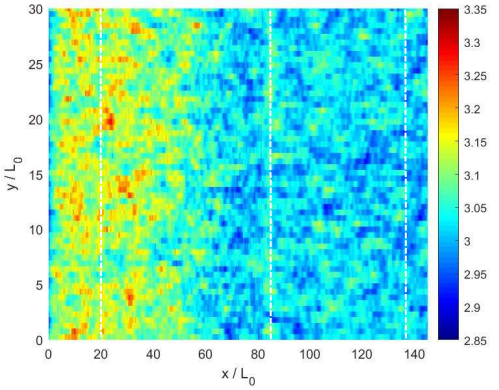

(f) $\sigma_\theta = 0.3,\ \gamma_s = 0.01$

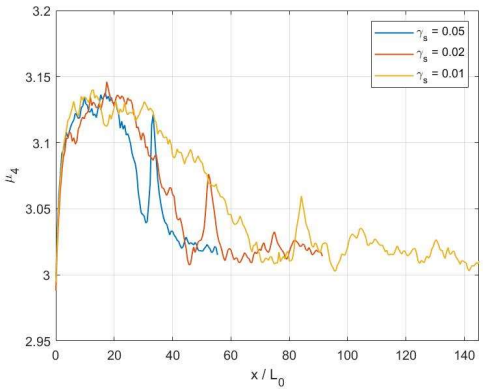

(g) $\sigma_\theta = 0.3,\ \gamma_s = 0.05, 0.02, 0.01$

Figure 4.21 Mean kurtosis of surface elevation η at uneven bottoms at different directional spread σ_θ and slope angle γ_s with initial BFI = 0.4

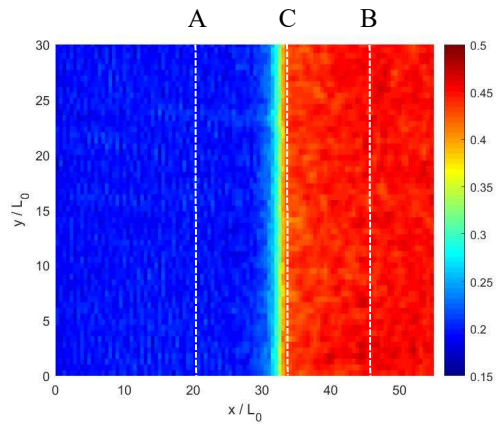

(a) $\sigma_\theta = 0.3,\ \gamma_s = 0.05$

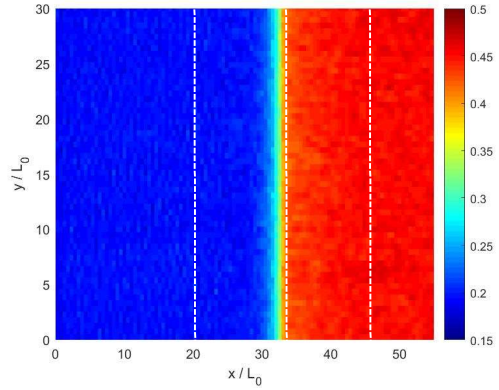

(b) $\sigma_\theta = 0.4,\ \gamma_s = 0.05$

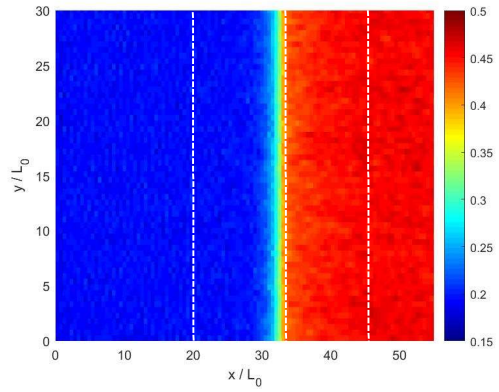

(c) $\sigma_\theta = 0.5,\ \gamma_s = 0.05$

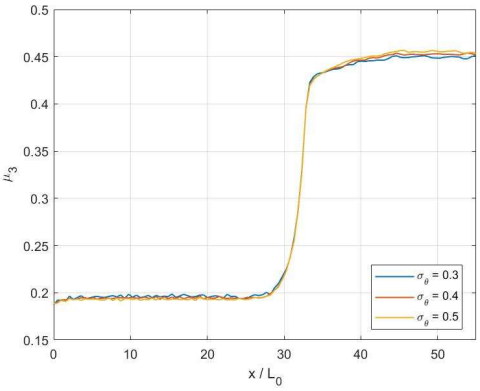

(d) : $\sigma_\theta = 0.3, 0.4, 0.5,\ \gamma_s = 0.05$

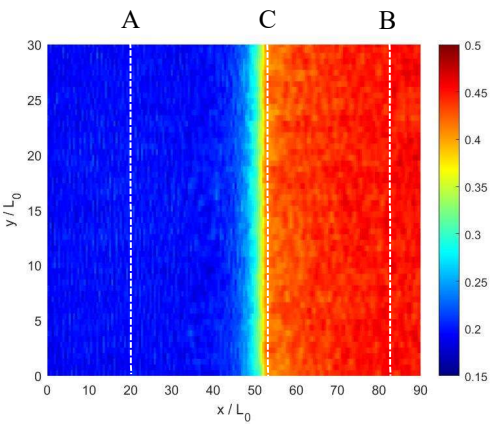

(e) $\sigma_\theta = 0.3,\ \gamma_s = 0.02$

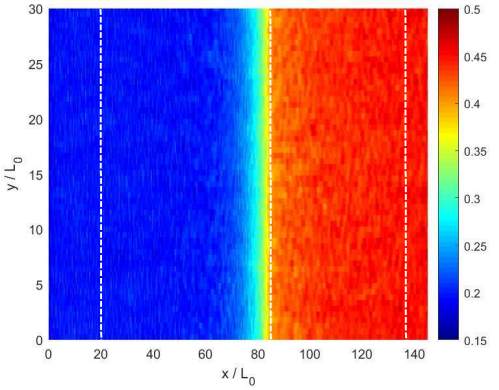

(f) $\sigma_\theta = 0.3,\ \gamma_s = 0.01$

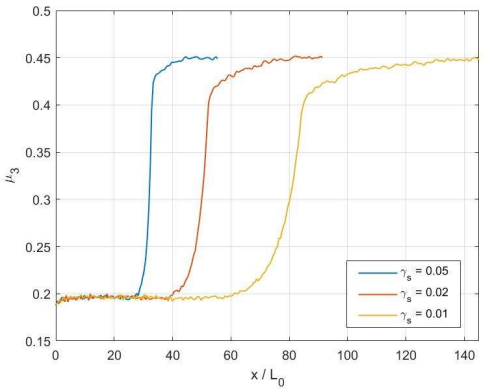

(g) $\sigma_\theta = 0.3,\ \gamma_s = 0.05, 0.02, 0.01$

Figure 4.22 Mean skewness of surface elevation η at uneven bottoms at different directional spread σ_θ and slope angle γ_s with initial BFI = 0.4

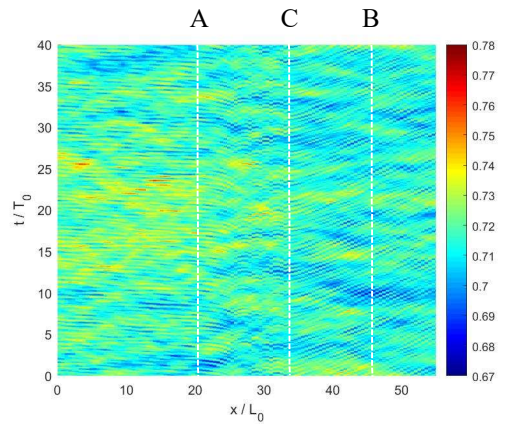

(a) $\sigma_\theta = 0.3,\ \gamma_s = 0.05$

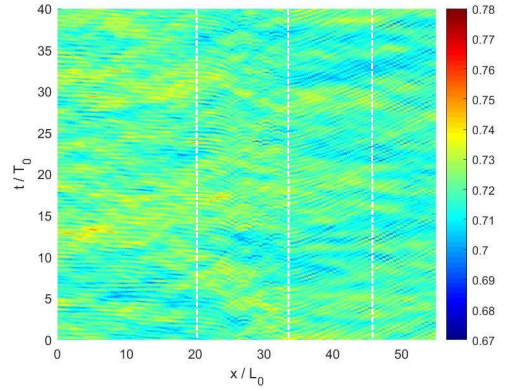

(b) $\sigma_\theta = 0.4,\ \gamma_s = 0.05$

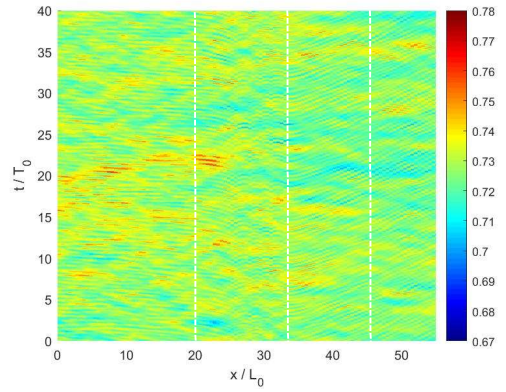

(c) $\sigma_\theta = 0.5,\ \gamma_s = 0.05$

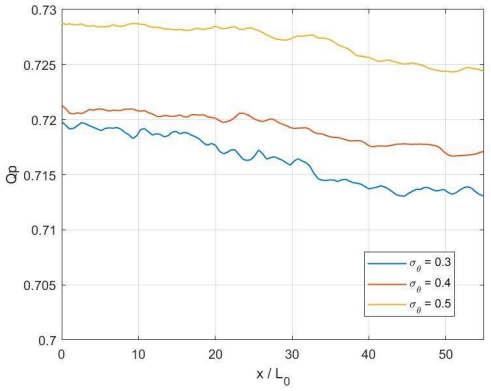

(d) : $\sigma_\theta = 0.3, 0.4, 0.5,\ \gamma_s = 0.05$

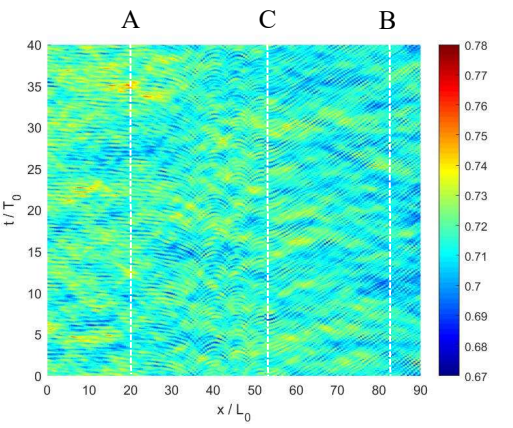

(e) $\sigma_\theta = 0.3,\ \gamma_s = 0.02$

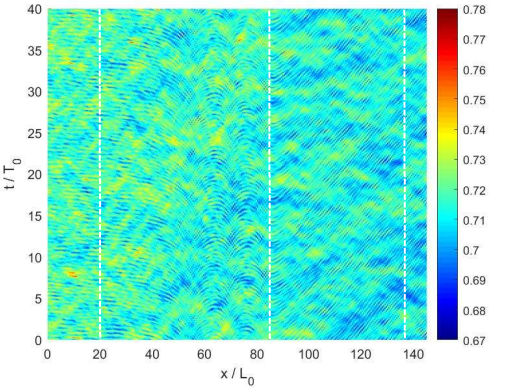

(f) $\sigma_\theta = 0.3,\ \gamma_s = 0.01$

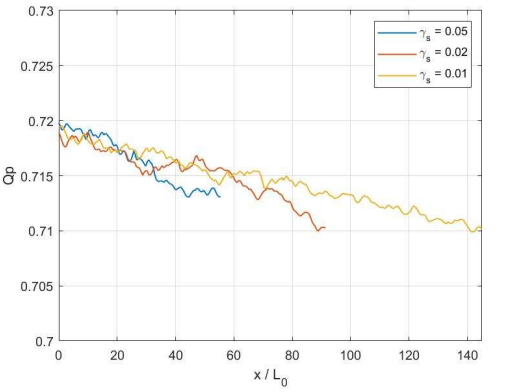

(g) $\sigma_\theta = 0.3,\ \gamma_s = 0.05, 0.02, 0.01$

Figure 4.23 Mean Q_p of surface elevation η at uneven bottoms at different directional spread σ_θ and slope angle γ_s with initial BFI = 0.4

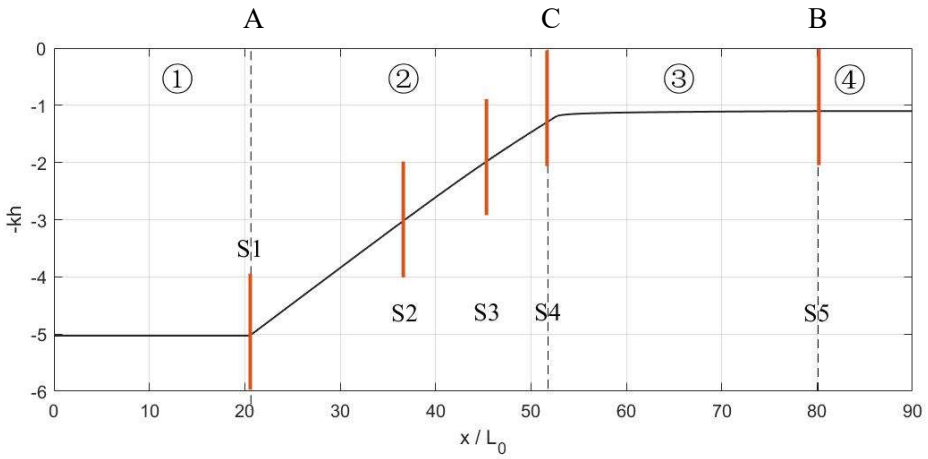

Figure 4.24 Five different sections on the uneven bottom type B_3 with γ_s = 0.02

To discuss the occurrence of extreme events in a more visible way, we give the distribution of the wave height and crest from the Monte Carlo simulation. On principal wave direction, we record the maximum wave height $H_{\max}$ and maximum wave crest $\eta_{\max}$ on the lateral direction from 40 periods of wave trains in 300 ensemble sizes. On the basis of it, we give the Cumulative Distribution Function (CDF) for the 2D wavefield in the same form as the unidirectional wave train. From deep to shallow water, we choose five different sections on the sloping region as **Figure 4.24**: S1 represents the demarcation point between the end of flat bottom in deep-water and the start of the sloping region at kh = 5 (dashed line A in previous figures); S2 is the section when water depth kh = 3; S3 is the section when water depth kh = 2; S4 is the demarcation point between the end of the sloping region with a constant slope γ_s and the start of decreasing slope at kh = 1.2 (dashed line C in previous figures); S5 is the demarcation point between the end of the sloping region and the start of flat bottom in shallow water at kh = 1.1 (dashed line B in previous figures).

Figure 4.25 shows the exceedance probability of the wave height and free surface elevation from the different directional spread in logarithmic coordinates at γ_s = 0.05, initial BFI = 0.4. In **Figure 4.25 (a)**, we give the CDF of the maximum wave height $H_{\max}$ from the numerical model with σ_θ = 0.3, 0.4, 0.5 and Rayleigh distribution. As the water depth decreases from S1 to S5, the occurrence probability of extreme wave height significantly

decreases from the comparison with the Rayleigh distribution (the linear distribution model doesn't change with water depth). The non-linear model gives a higher exceeding probability of extreme events than the linear distribution in deep-water (S1) but lower in shallow water (S4, S5). In medium water depth (S2, S3), they have a similar prediction of wave heights distribution. In S1-S4, the increase of directional spread σ_θ leads to the decrease of the exceeding probability for $H_{\max}/\eta_{\mathrm{rms}} > 7$. However, in a very shallow water depth (S5), the result from the larger σ_θ shows a slightly higher occurrence probability of extreme events. Corresponding to the variation of kurtosis in **Figure 4.21**, the increase of σ_θ has different consequents in $H_{\max}$ at different water depths, which comes from the change of the four-wave interaction on the wave train instability. In shallow water, the incident wave with higher σ_θ gives more dispersion on BFI, and the increase of the wave train instability due to the second-order effect becomes more significant. This result is consistent with the previous discussion in the evolution of wave train nonlinearity in 1D and 2D. In **Figure 4.25 (b)**, we give the exceeding probability of wave crest $\eta_{\max}$ from the different directional spread. The CDF of $\eta_{\max}$ has similar behaviors with $H_{\max}$ under the effect from σ_θ and water depth. However, the deviation between the $\eta_{\max}$ from the non-linear model and Rayleigh distribution is very significant, which reflects the contribution from the non-linear effect in the surface construction.

The CDF of maximum wave height and crest at σ_θ = 0.3, initial BFI = 0.4 from different bottom topography is given in **Figure 4.26**. In **Figure 4.26 (a)**, the effect from slope angle mainly reflects in the medium and shallow water depth in S2-S4. The exceeding probability of extreme events will increase if the slope angle γ_s gets steep, and this trend is getting obvious in shallower water depth. When the bottom change is very mild (in S5), the effect from different γ_s is very small. The CDF of $\eta_{\max}$ from different bottom topography in **Figure 4.26 (b)** gives a similar conclusion. The result from different bottom topography mainly reflects the second-order effect, which is one of the important determining factors of the wave train instability in the medium and shallow water depth. If we compare **Figure 3.21** and **Figure 4.26**, we will find different bottom topography has a similar effect in both 1D and 2D, but the result in 1D wave has a lower exceeding probability of extreme events in shallow water than 2D due to the lack of directional dispersion effect.

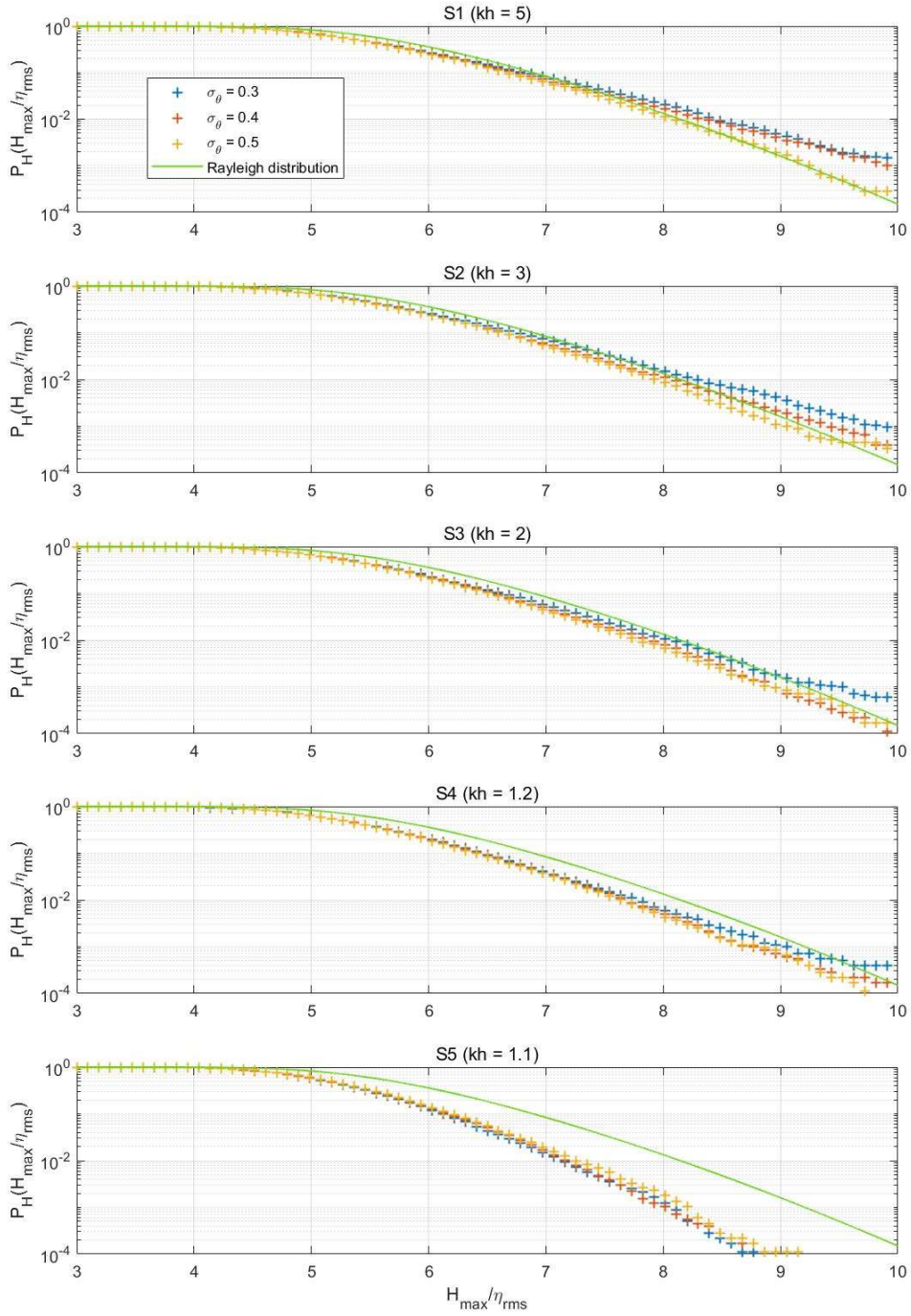

(a) Maximum wave height $H_{\max}$ from different directional spread

Figure 4.25 Exceedance probability of wave height and free surface elevation distribution at γ_s = 0.05, initial BFI = 0.4

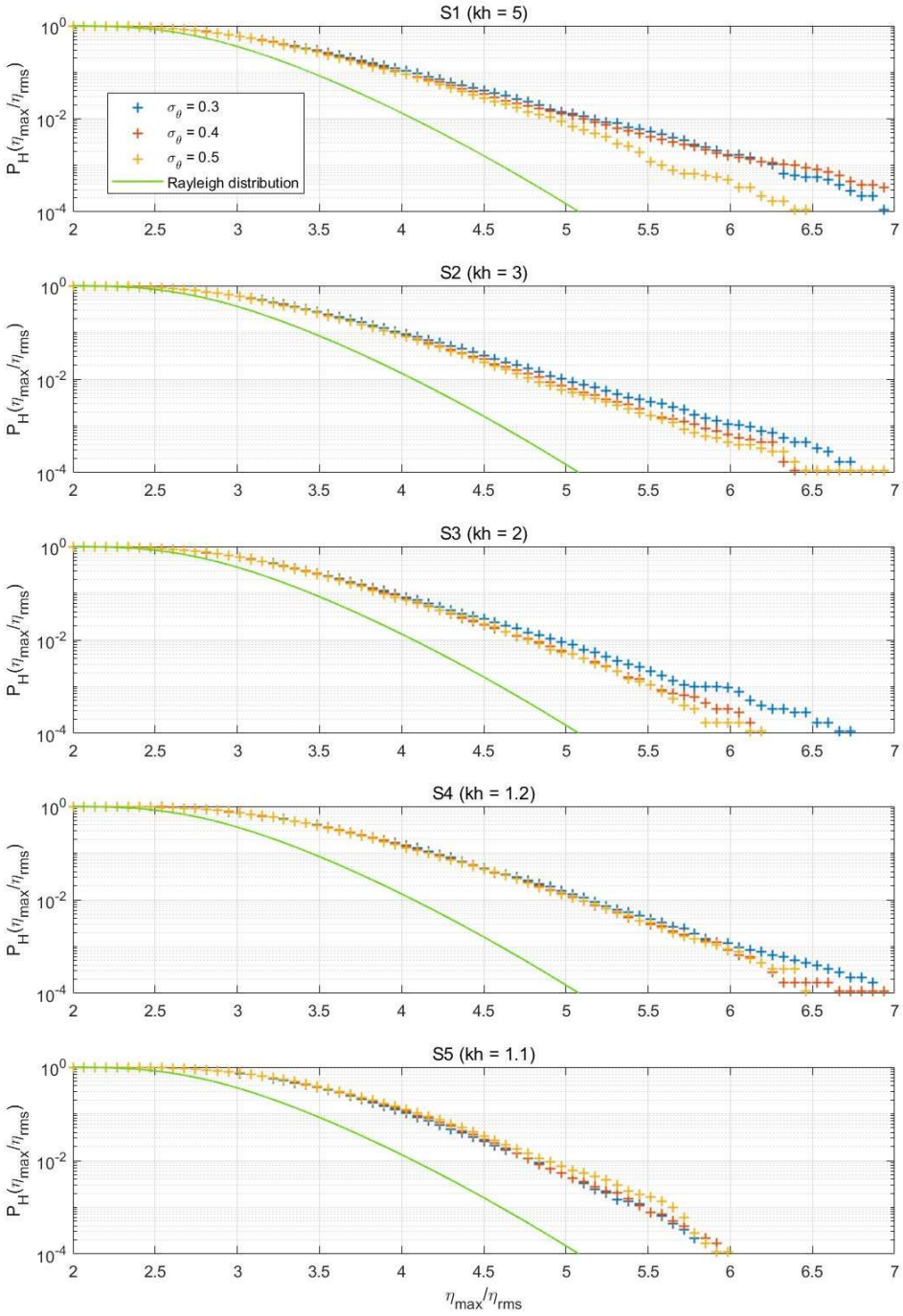

(b) Maximum wave crest $\eta_{\max}$ from different directional spread

Figure 4.25 Exceedance probability of wave height and free surface elevation distribution at γ_s = 0.05, initial BFI = 0.4 (cont.)

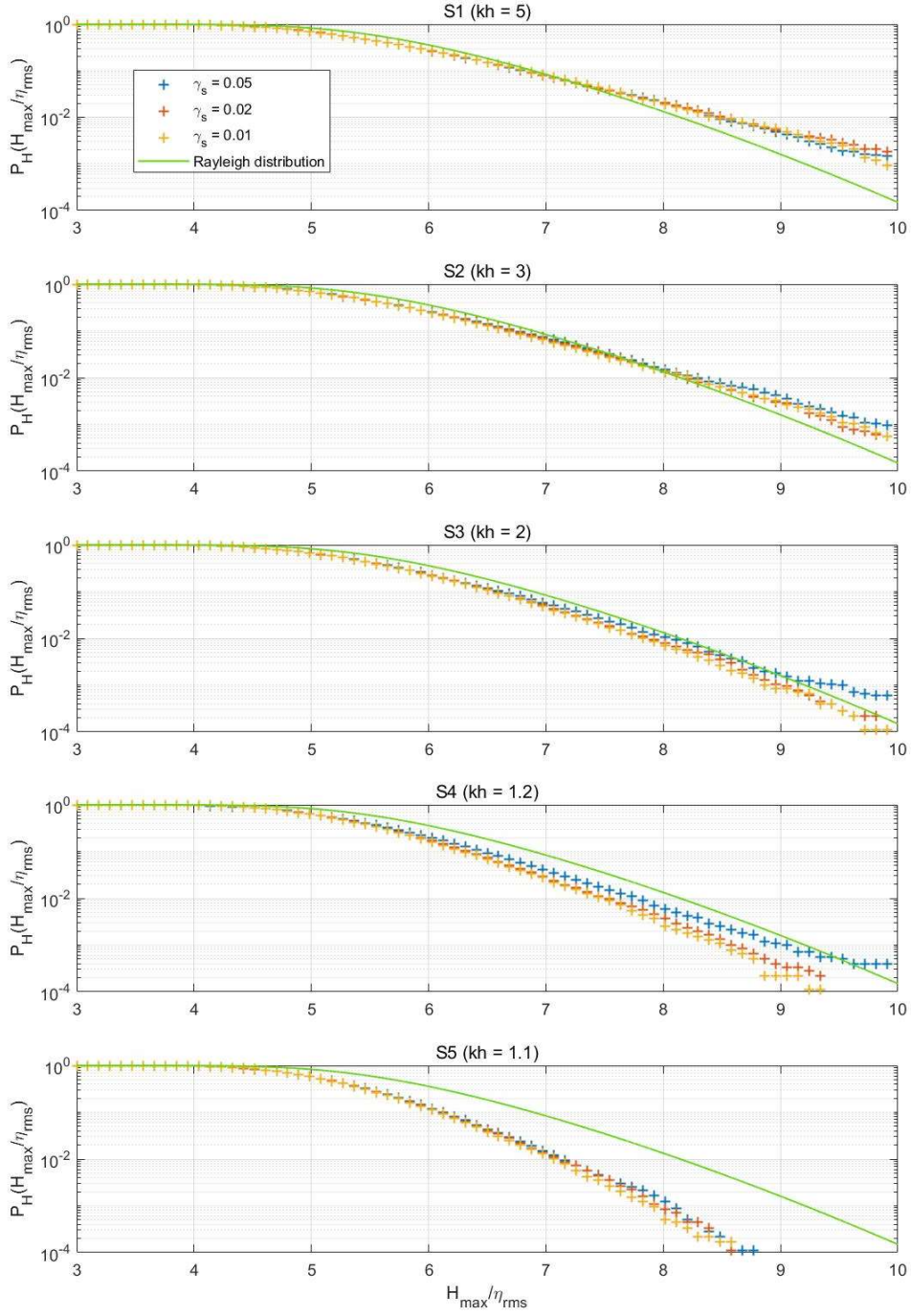

(a) Maximum wave height $H_{\max}$ from different slope angle

Figure 4.26 Exceedance probability of wave height and free surface elevation distribution at σ_θ = 0.3, initial BFI = 0.4

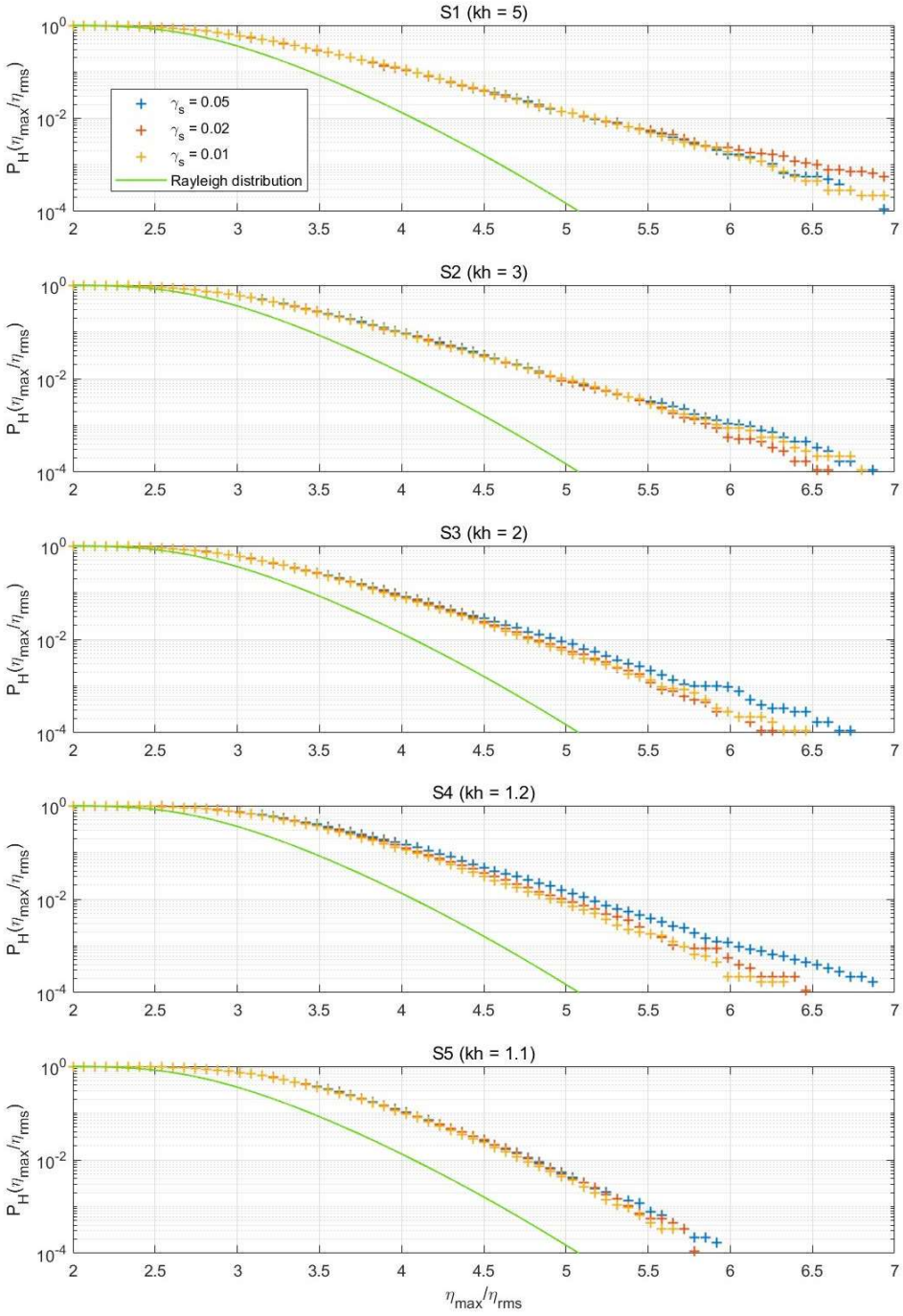

(b) Maximum wave crest $\eta_{\max}$ from different slope angle

Figure 4.26 Exceedance probability of wave height and free surface elevation distribution at σ_θ = 0.3, initial BFI = 0.4 (cont.)

4.3.3 Evolution of oblique modulated wave

If we assume the principal wave propagation direction θ_0 has a small oblique angle that $\tan\theta_0 < O(\varepsilon)$, the carrier wave number $k_0 \approx k_x$ in the numerical tank. We here apply the numerical model to consider the slightly oblique modulated wave in the 2D wavefield.

Firstly, we conduct the simulation at a flat bottom. **Figure 4.27** gives the above view of the surface elevation given in Eq. (4-13) from a single sample at $\tan\theta_0$ = 0.1, 0.2 and 0.3. To make the wave propagation easier to be distinguished, we set the initial BFI = 1 in this example to make the wave train more regular. The coherent wave envelope reflects the principal wave direction and the oblique angle between it and the x axis. In **Figure 4.28**, we give the mean kurtosis and skewness from Monte Carlo simulation at flat bottoms from a different oblique angle θ_0 with initial BFI = 0.4, σ_θ = 0.3, kh = 5. The result from $\tan\theta_0$ = 0.1 to 0.3 don't show the difference caused by the change of θ_0. The statistical parameters are uniform in an SSS 2D field, so the stabilized μ_4 and μ_3 are constant in each direction. In **Figure 4.29**, we give the mean Q_p from Monte Carlo simulation at flat bottoms from different oblique angles θ_0 with initial BFI = 0.4, σ_θ = 0.3, kh = 5. Different from μ_4 and μ_3, the increase of θ_0 brings about the significant rise of Q_p. This is because we calculate Q_p by the spatial distribution of η on the lateral direction of the bottom contour, not the principal direction, and Q_p is given in an $x-t$ plane. As the increase of incident oblique angle, the directional dispersion increases on the y axis, which reflects in the spectral bandwidth and Q_p, but it is only a difference in expression and there is no change occurs in the wave field.

The result by a flat bottom only provides an examination of the numerical model and a reference for the following discussion. Essentially, the change in the incident oblique angle does not lead to any influence on the wave evolution in a 2D wavefield with the flat bottom condition. The difference in result is only caused by the statistical method in different directions. However, when we consider an uneven bottom, the oblique angle may bring about changes since the wave propagation direction is not consistent with the contour line of the bottom topography.

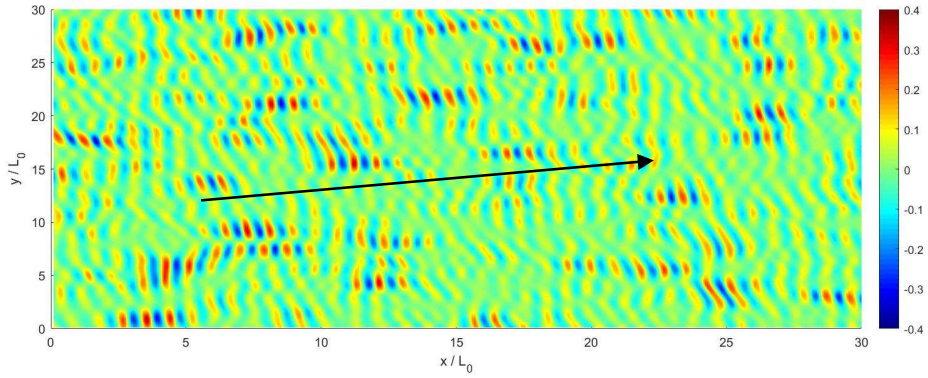

(a) $\tan\theta_0 = 0.1$

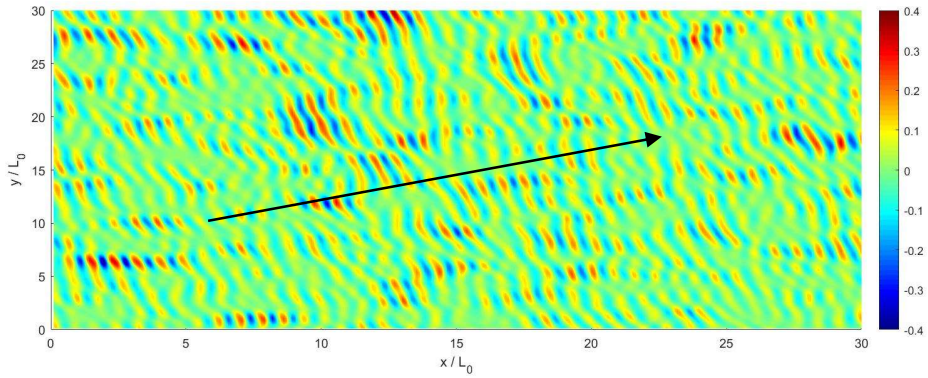

(b) $\tan\theta_0 = 0.2$

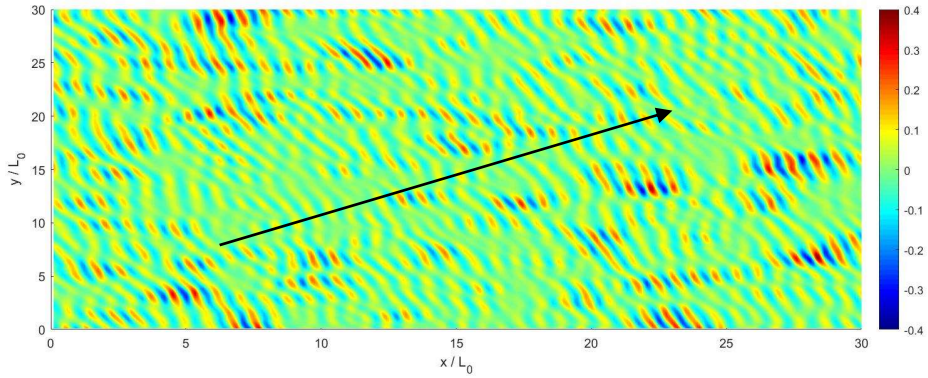

(c) $\tan\theta_0 = 0.3$

Figure 4.27 Surface elevation η over a flat bottom at $t = 40T_0$ from different directional spread σ_θ with initial BFI = 1, $\sigma_\theta = 0.3$, $kh = 5$

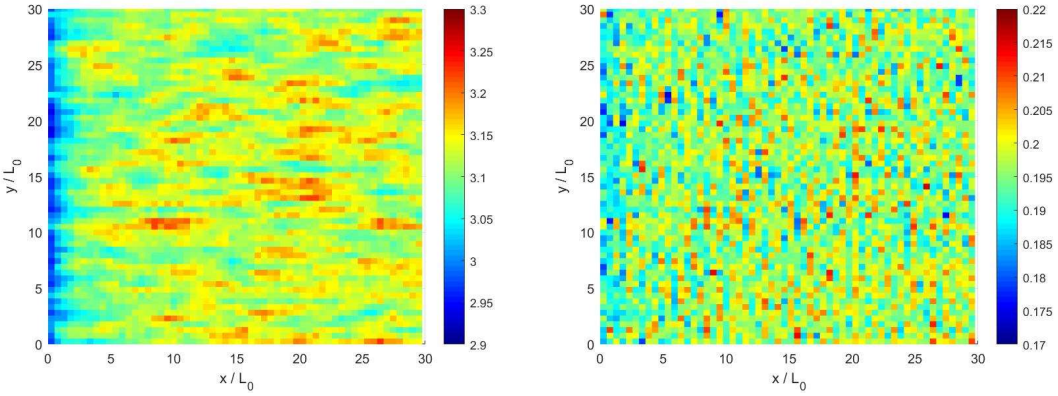

(a) μ_4 at $\tan\theta_0 = 0.1$ (b) μ_3 at $\tan\theta_0 = 0.1$

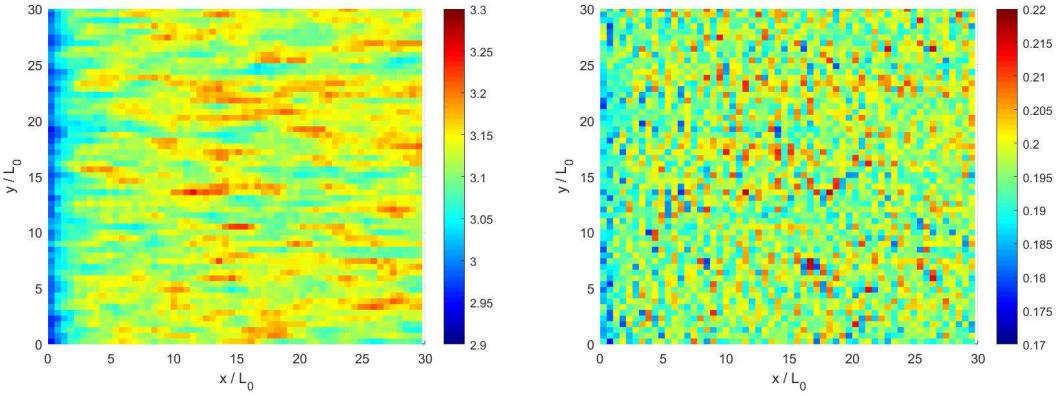

(c) μ_4 at $\tan\theta_0 = 0.2$ (d) μ_3 at $\tan\theta_0 = 0.2$

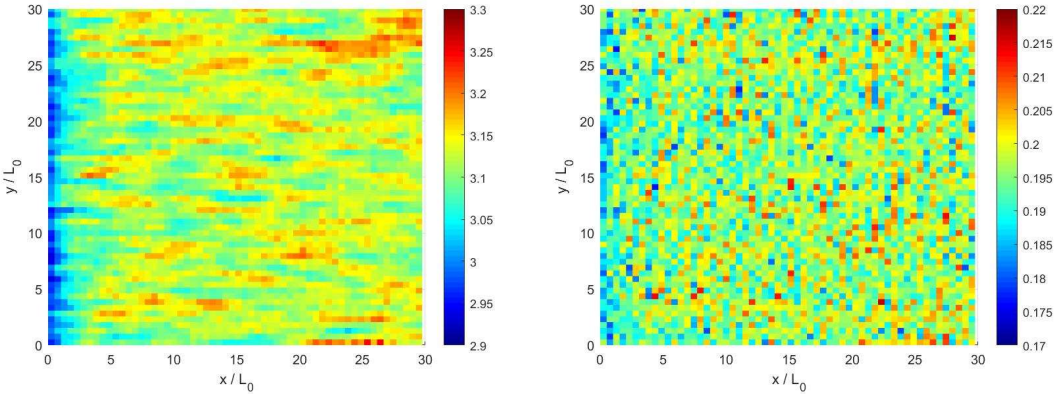

(e) μ_4 at $\tan\theta_0 = 0.3$ (f) μ_3 at $\tan\theta_0 = 0.3$

Figure 4.28 Mean μ_4 and μ_3 of surface elevation η at flat bottoms from different oblique angle θ_0 with initial BFI = 0.4, $\sigma_\theta = 0.3$, $kh = 5$

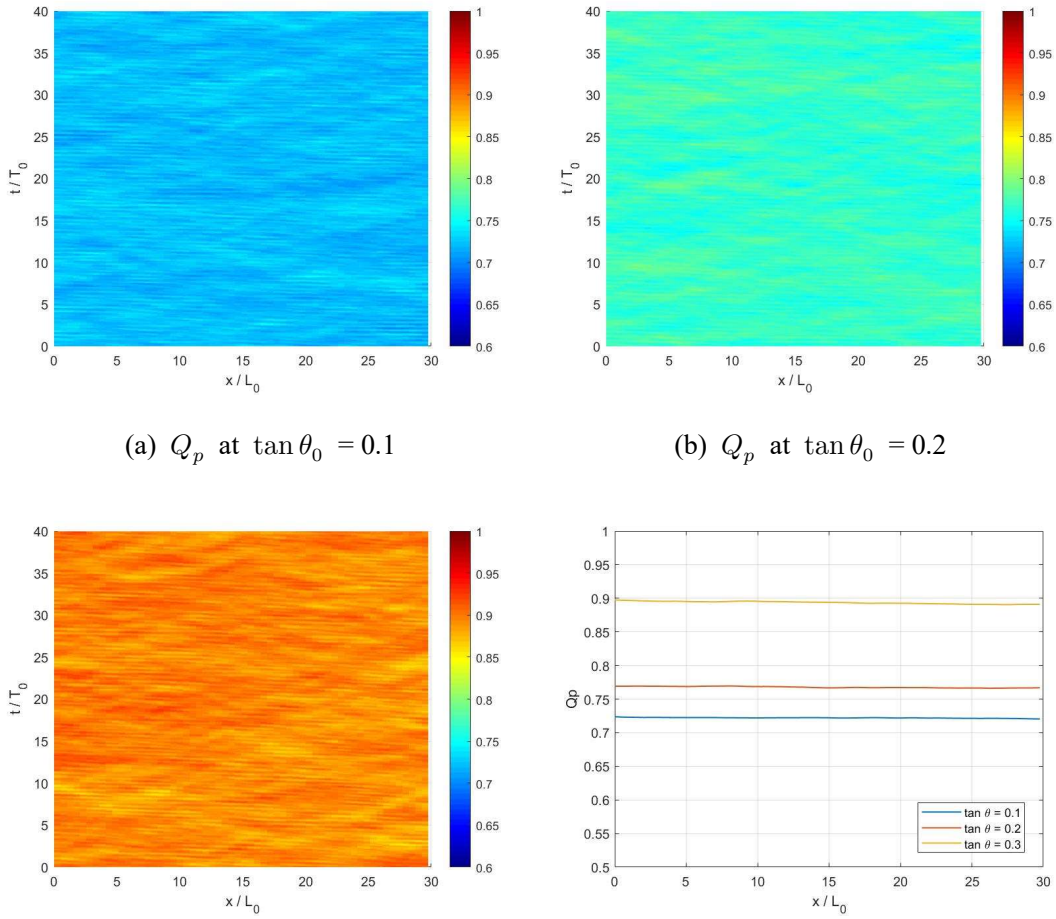

(a) Q_p at $\tan\theta_0 = 0.1$

(b) Q_p at $\tan\theta_0 = 0.2$

(c) Q_p at $\tan\theta_0 = 0.3$

(d) Q_p on the principal direction

Figure 4.29 Mean Q_p of surface elevation η at flat bottoms from different oblique angle θ_0 with initial BFI = 0.4, $\sigma_\theta = 0.3$, $kh = 5$

Next, we conducted a series of numerical simulations for oblique waves on the slopes. When $\tan\theta_0$ = 0.3, the carrier wave number $k_0 \approx 1.044k_x$ and the result may not be reliable. Thus we take $\tan\theta_0$ = 0, 0.1 and 0.2 for the sloping cases that the principal wave direction is different from the gradient direction of depth. In **Figure 4.30**, we calculated the ensemble-averaged kurtosis μ_4 and skewness μ_3 from Monte Carlo simulation at the uneven bottom B_3 with γ_s = 0.05 from the different oblique angle θ_0 with initial BFI = 0.4, σ_θ = 0.3. On the sloping region and shallow water depth, the result from the oblique angle $\tan\theta_0$ = 0 to 0.2 almost have no difference. **Figure 4.30 (g)** and **Figure 4.30 (h)** give the mean μ_4 and μ_3 in 1D from the lateral direction of the gradient of water depth change (i.e. the x axis) instead of the principal wave direction, and the change of oblique angle have very little influence on the variation of μ_4 and μ_3. The little change in μ_4 and μ_3 indicates, the third-order and second-order nonlinearities of 2D wavefield are hardly affected by the included angle between the wave propagation direction and the gradient of water depth change statistically when this angle is not significant. In the estimation of the maximum wave height and crest, the extreme events are basically triggered by the instability caused by the non-linear effect, so the approximately unchanged results of μ_4 and μ_3 imply the oblique angle is not an important factor in the freak wave analysis.

For the purpose of developing the simulation model of the non-linear modulated wave evolution, we continue to explore the change in wavefield due to the oblique angle. In **Figure 4.31**, we give the mean Q_p of surface elevation η at the uneven bottom B_3 from the different oblique angle θ_0 with initial BFI = 0.4, σ_θ = 0.3, γ_s = 0.05. When the wave propagates into shallow water, the Q_p significantly increases at $\tan\theta_0$ = 0.2. From the 1D mean result on the gradient direction of depth in **Figure 4.31 (d)**, the increase of θ_0 leads to an increasing trend of Q_p at the sloping region in shallow water. However, Q_p decreases slightly as the water depth decrease when θ_0 = 0 in **Figure 4.23**, which gives an opposite result.

Different from the other index in the analysis of nonlinearity of wave train, the increase of Q_p with the increase of the oblique angle θ_0 in shallow water reflects the influence from the disagreement between the principal wave direction and the gradient direction of depth. In the

wave shoaling process, the group speed c_g and wave steepness ε increase with the decrease of water depth on the bottom contour as well as the contribution from the slope angle. If the oblique angle θ_0 is large enough, the differenct c_g on the lateral direction of the principal wave direction will lead to the refraction and the change of the principal wave direction. However, these changes don't exist in our wave model for small θ_0. We assume the directional wave spectrum is in Gaussian distribution with θ_0 as the expectation from the initial condition, and the increase of Q_p in shallow water represents the width of directional spectral peak becomes wider with the decrease of water depth in shallow water. The value of the oblique angle θ_0 seems to play a role in the evolution of the directional wave spectrum in shallow water with an uneven bottom, even the initial spectrum has the same shape and bandwidth. The increase of θ_0 disperses the wave energy into more directions as the water depth decreases on the slope. In spite of this, this effect is not significant in terms of the magnitude of the values.

To check the reflection from the wave nonlinearity on the real surface elevation, we give the ensemble-averaged maximum wave height $H_{\max}/\eta_{\mathrm{rms}}$ and maximum wave crest $\eta_{\max}/\eta_{\mathrm{rms}}$ in **Figure 4.32**. Even the increase of the incident oblique angle θ_0 brings about the increase of Q_p in shallow water, this contribution is so weak that the distribution of the expected maximum value doesn't change with the oblique angle. It is more clear in the averaged $H_{\max}/\eta_{\mathrm{rms}}$ and $\eta_{\max}/\eta_{\mathrm{rms}}$ on the x axis in 1D from **Figure 4.32 (g)** and **Figure 4.32 (h)**. In **Figure 4.33**, we give the exceedance probability of wave height and free surface elevation distribution in the same form with **Figures 4.25** and **4.26** for $\tan\theta_0$ = 0, 0.1 and 0.2. At different sections of water depth, the effect from oblique angle θ_0 is not significant in neither the CDF of $H_{\max}$ or $\eta_{\max}$.

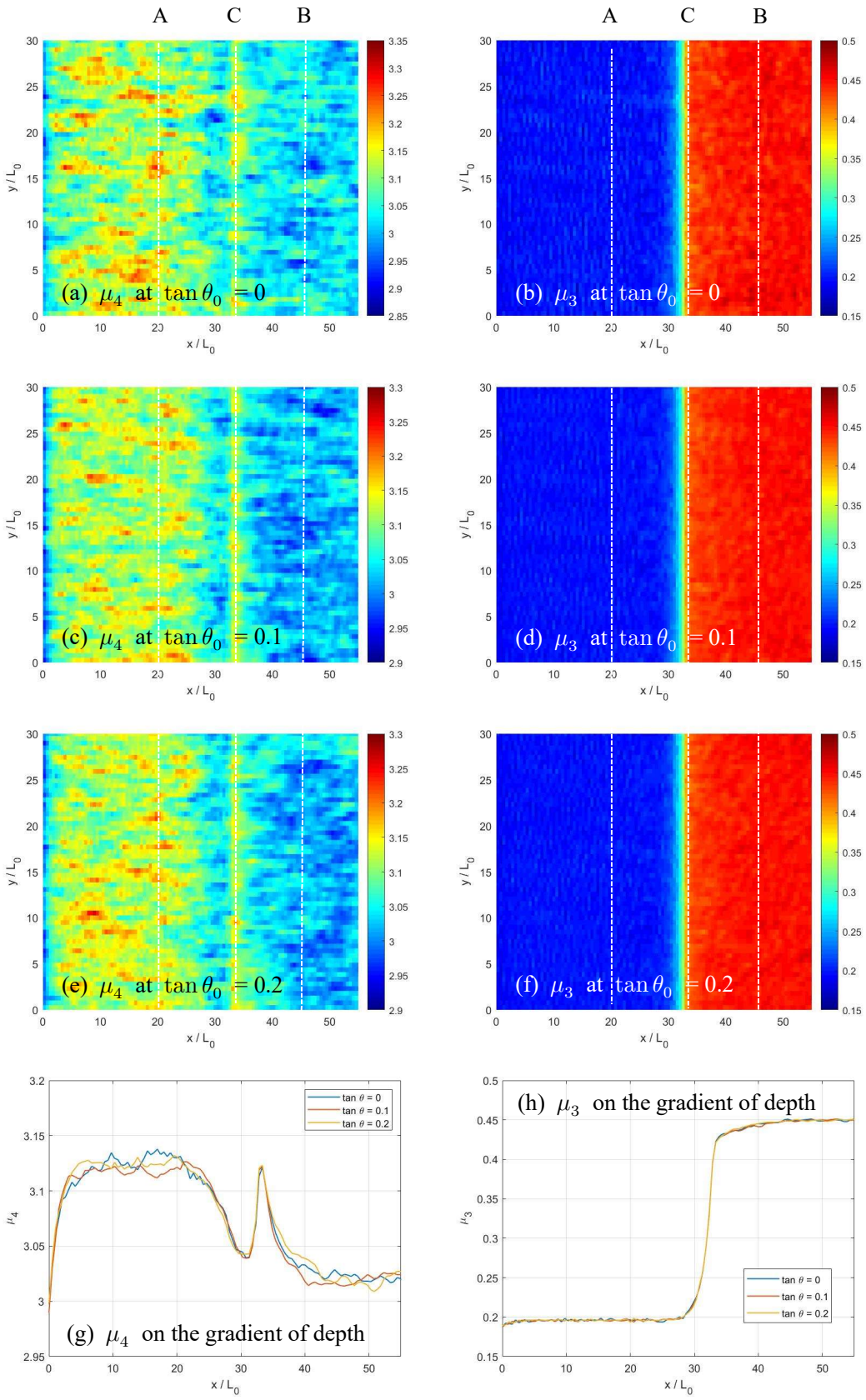

Figure 4.30 Mean μ_4 and μ_3 of surface elevation η at uneven bottoms from different oblique angle θ_0 with initial BFI = 0.4, $\sigma_\theta = 0.3$, $\gamma_s = 0.05$

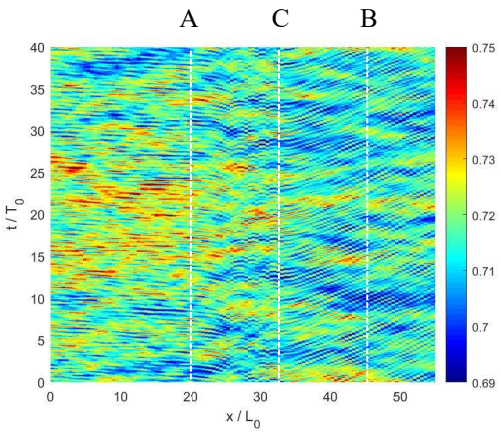

(a) Q_p at $\tan\theta_0 = 0$

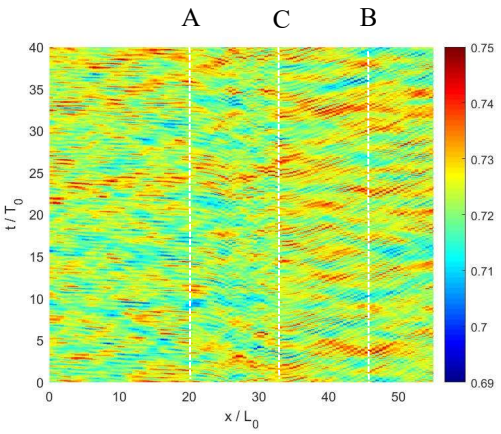

(b) Q_p at $\tan\theta_0 = 0.1$

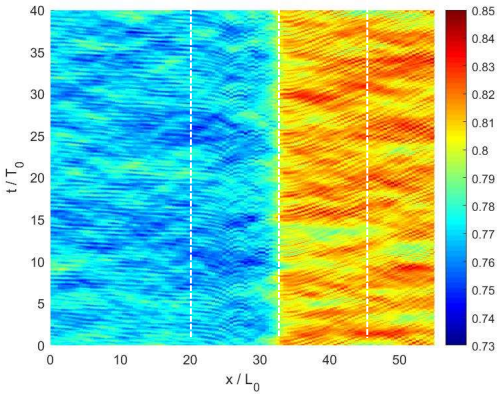

(c) Q_p at $\tan\theta_0 = 0.2$

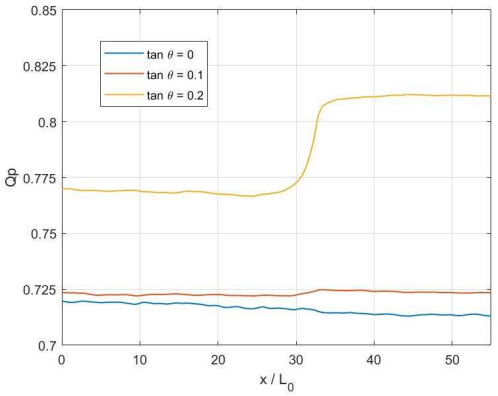

(d) Q_p on the gradient direction of depth

Figure 4.31 Mean Q_p of surface elevation η at uneven bottoms from different oblique angle θ_0 with initial BFI = 0.4, $\sigma_\theta = 0.3$, $\gamma_s = 0.05$

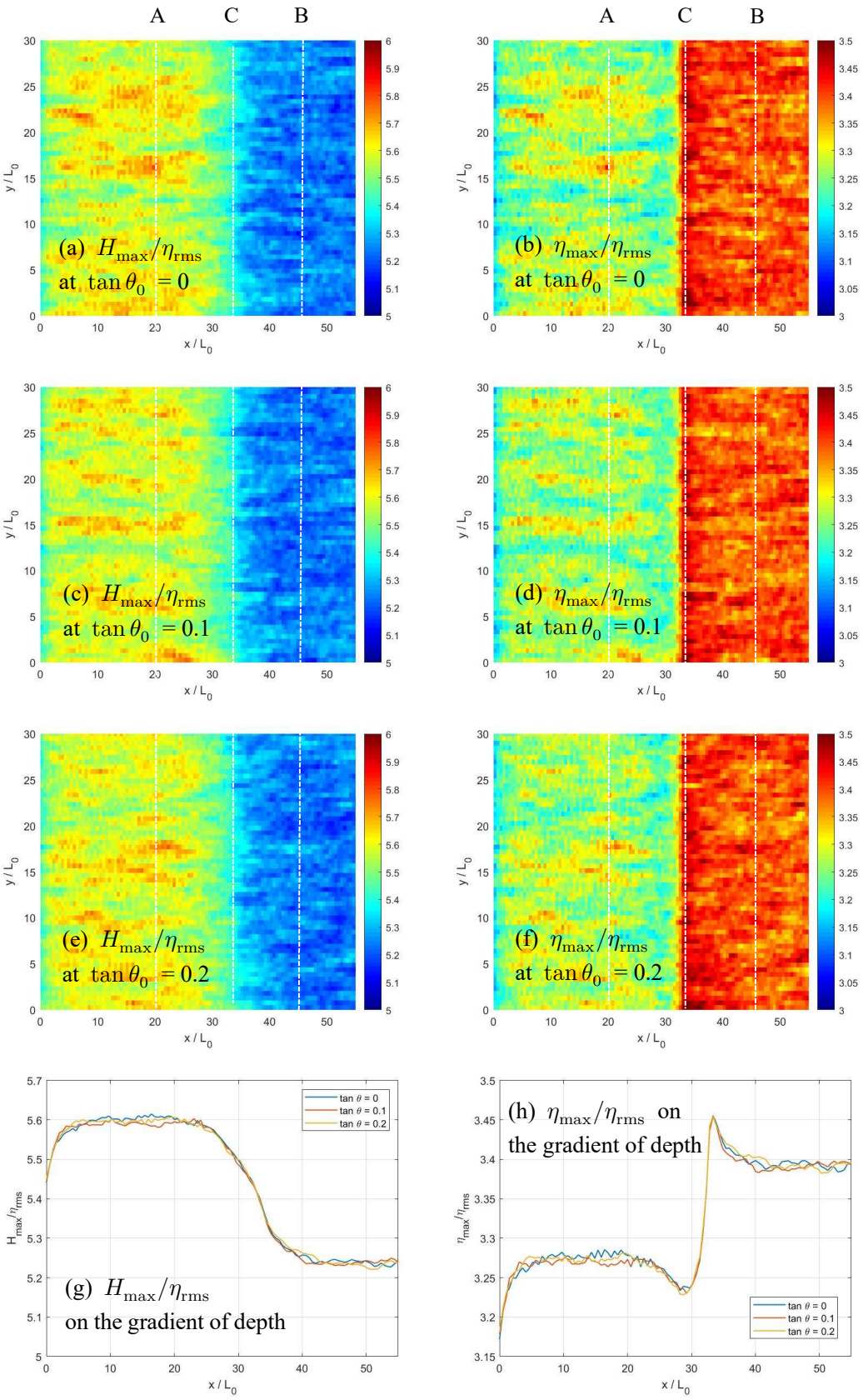

Figure 4.32 Ensemble-averaged maximum wave height and surface elevation at uneven bottoms from different oblique angle θ_0 with initial BFI = 0.4, $\sigma_\theta = 0.3$, $\gamma_s = 0.05$

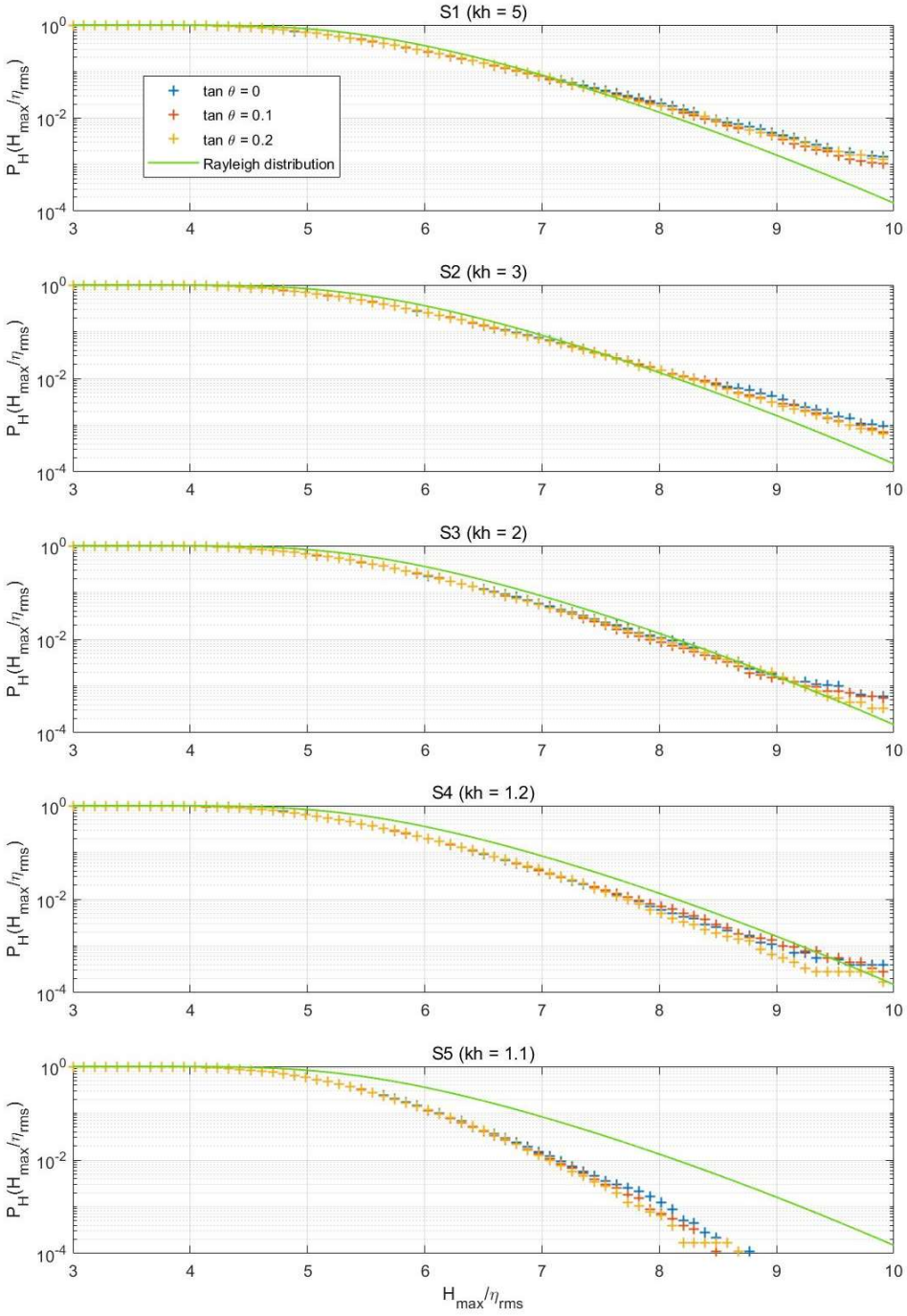

(a) Maximum wave height $H_{\max}$ from different oblique angle θ_0

Figure 4.33 Exceedance probability of wave height and free surface elevation distribution at σ_θ = 0.3, initial BFI = 0.4, γ_s = 0.05

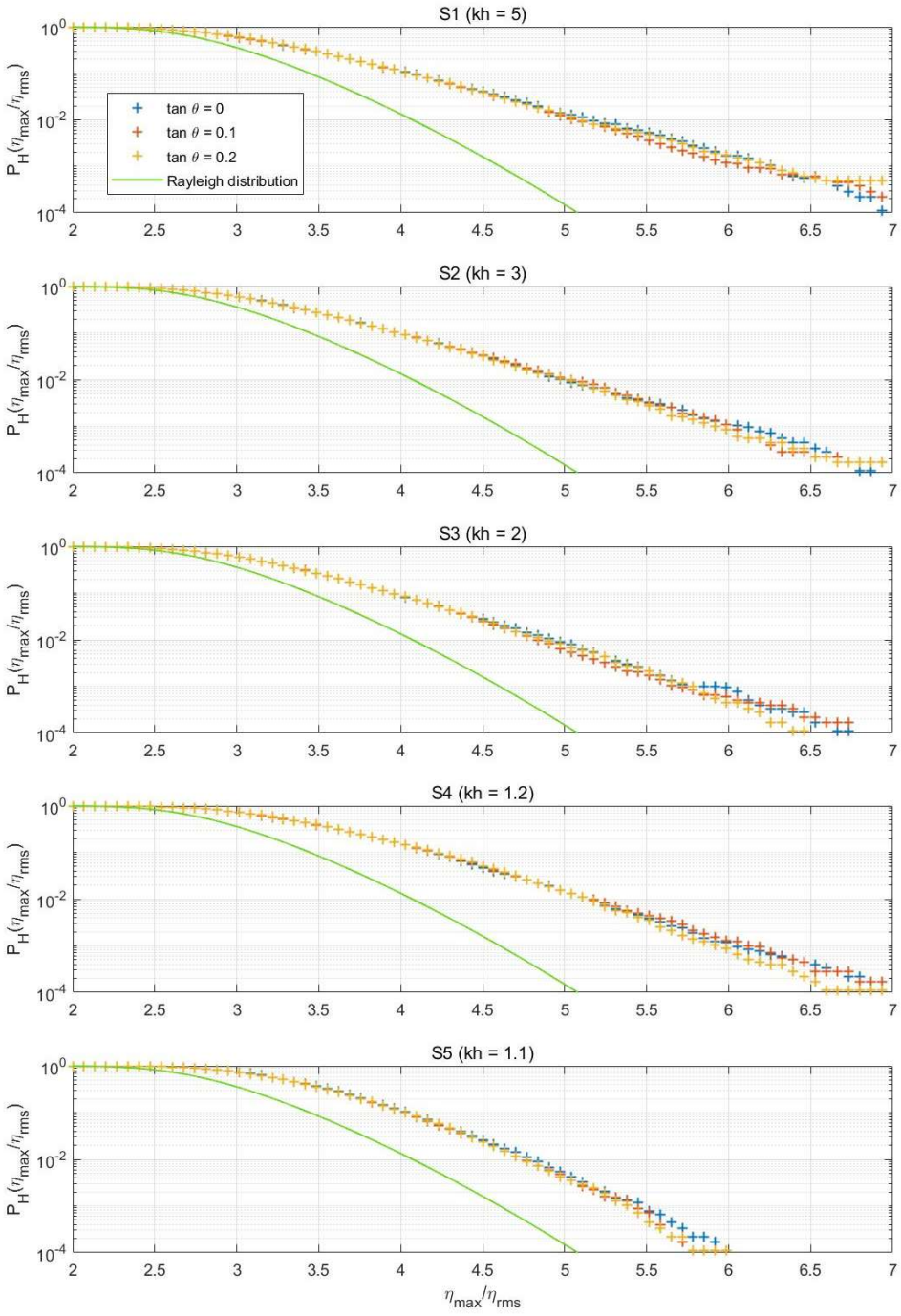

(b) Maximum wave crest $\eta_{\max}$ from different oblique angle θ_0

Figure 4.33 Exceedance probability of wave height and free surface elevation distribution at σ_θ = 0.3, initial BFI = 0.4, γ_s = 0.05 (cont.)

4.4 Summary

Based on the 2D mNLS equation and pseudo spectral method, we expand the third-order non-linear model for the evolution of the unidirectional wave train into a 2D wavefield for variable depth. With the Monte Carlo simulation from random initial phase information, we study the evolution of directional modulated wave trains over the uneven bottom with the consideration of directional dispersion and spatial inhomogeneity from different bottom types. In a similar way with the analysis of 1D, we discuss the surface instability from the high-order moment of surface elevation and the distribution of extreme wave height and crest. Additionally, we also consider the wave evolution with a small oblique incident angle with the contour line of the bottom topography. The result indicates:

A) The directional dispersion effect can weaken the four-wave interaction in a 2D wavefield. The rise of the directional dispersion will make the kurtosis of surface elevation decrease in deep-water but increase in shallow water, in a similar way with the decrease of the initial BFI. Correspondingly, the directional spread contributes to the exceedance probability of maximum wave height and crest the same as to kurtosis.

B) The directional dispersion effect has almost no effect on the skewness of surface elevation, and the skewness in a 2D wavefield is mainly determined by the wave steepness.

C) Steep slope angle leads to the rebound of kurtosis in the shallow water due to wave shoaling as the unidirectional wave train, and it reflects in the increase of the exceedance probability of maximum wave height and crest.

D) When we estimate the directional spectrum peakedness by Q_p on the lateral direction, Q_p is related to the directional spread. For direct incident waves, Q_p decreases slightly from the deep-water to shallow water, but Q_p increases in the medium and shallow water when the included angle between the contour line and the principal wave direction increases before the wave refraction occurs.

Chapter 5

Conclusions

The study on the freak wave contributes to the understanding of the non-linear fluctuation in natural phenomena, and helps to the estimation of ocean waves for navigation and ocean engineering in a practical sense. Previous study indicates the occurrence of freak wave is caused by the modulational instability from the high-order interactions.

In this research, we investigate the generation of the freak wave by the simulation of non-linear modulated wave trains. As a simplified expression of the weak non-linear modulated wave, the NLS equation is applied to give the evolution equation of wave envelope. Based on the bottom boundary equation with mild changing depth, we derive the 2D modified NLS equation in a similar form with previous theoretical research.

The particular solution of the NLS equation has been given as soliton, breather, and so on, and the numerical simulations in deep-water have well explained the generation of freak wave in related studies. In this dissertation, we concentrate on the medium and shallow water depth from offshore to onshore, and we intend to investigate the specific impacts from the bottom topography on the modulated wave trains at sea states. Whether it is in the unidirectional wave or the 2D wavefield, the spatial inhomogeneity contributes to the wave train instability through the change of dispersion relation and the shoaling effect due to the slope angle.

We build the non-linear evolution model for the unidirectional wave train and the 2D wavefield by numerically solving modified NLS equation on the gradient direction of depth. To simulate the real wave surface in more accurate way, we construct the surface elevation from the solution of wave envelope considering the second-order and second-harmonic term. Monte Carlo simulation is applied to give the estimation of the high-order moment kurtosis and

skewness of the surface elevation, which reflect the wave train instability and are related to the occurrence probability of the freak wave. We also record the distribution of maximum wave height and crest from the ensemble data as the outcomes in real surface.

The initial condition plays an important role in both the unidirectional wave and the 2D wavefield. We assume the initial frequency spectrum is consistent with the Gaussian distribution, and give the initial BFI as the ratio between the wave steepness and dimensionless spectral bandwidth. The degree of four-wave interaction varies in the wave trains starting with different BFI, and it is affected by the water depth: in the deep-water, wave train with higher initial BFI has larger kurtosis and skewness; in the medium and shallow water, the rise of BFI gives the decrease of kurtosis and skewness. In a 2D wavefield, the initial spectrum has the Gaussian shape distribution on the frequency and the direction of component waves, so we introduce the directional spread as another variable to determine the spectral bandwidth in 2D. The numerical result shows that the directional spread has a dispersion effect on the four-wave interaction as the theoretical prediction: the increase of the directional spread leads to the decrease of kurtosis in deep-water, but it will make the kurtosis increase in shallow water, which has similar effect as decreasing the initial BFI. Different with kurtosis, the directional spread hardly affects skewness.

From the deep-water to shallow water, the evolution of kurtosis and skewness reflect the contribution from the water depth change and bottom types. In deep-water, the wave train instability is mainly determined by the four-wave interaction, and it increases when the water depth gets deeper. As the wave propagates into the medium and shallow water, the effect from the four-wave interaction becomes weak and the increase of initial BFI will instead lead to the decrease of kurtosis in very shallow water. As opposed to the four-wave interaction at the third-order, the second-order effect gradually becomes an important factor from the bound wave. In the wave shoaling process, the wave steepness and the group speed increases with the decrease of water depth, which reflects in the increase of the second-order nonlinearity by skewness. The slope angle contributes to the wave train instability in the wave shoaling, and it becomes more significant in a shallower depth. Steep slope angle brings about a rebound process of kurtosis in the shallow water, and it disappears when the slope becomes very mild or the wave propagates into a flat bottom.

The theoretical occurrence probability of the freak wave can be estimated by kurtosis, and it is sufficiently reflected in the distribution of wave height and free surface elevation from the numerical result. The exceedance probability of extreme events is corresponding to the variation of kurtosis at different conditions. In summary, the increase of the initial BFI and the decrease of the directional spread give the rise of the occurrence rate of the freak wave in deep-water but reduce it in the shallow water. Steep slope angle also contributes to the increase of the occurrence probability of freak wave in medium and shallow water. As a linear prediction, the Rayleigh distribution underestimates the exceedance probability of maximum wave height in deep-water and overestimates it in the shallow water. The distribution of the wave crest shows a significant exceeding than the wave height due to the contribution from the non-linear term in the surface construction.

The spectrum peakedness Q_p is applied to give an estimation of spectral bandwidth in the wave train evolution. Q_p of the frequency spectrum is highly relevant of the initial BFI, and Q_p of the directional spectrum reflects the magnitude of the directional spread. When the principal wave direction has a little oblique angle θ_0 with the gradient of water depth change, kurtosis and skewness almost have no change but the Q_p of directional spectrum increases in the shallow water, which indicates that θ_0 contributes to the evolution of the directional wave spectrum and disperse the wave energy into more directions on the slope.

The summary of the effect from the initial condition and the bottom topography change acting on the non-linear wave evolution is given in **Figure 5.1**.

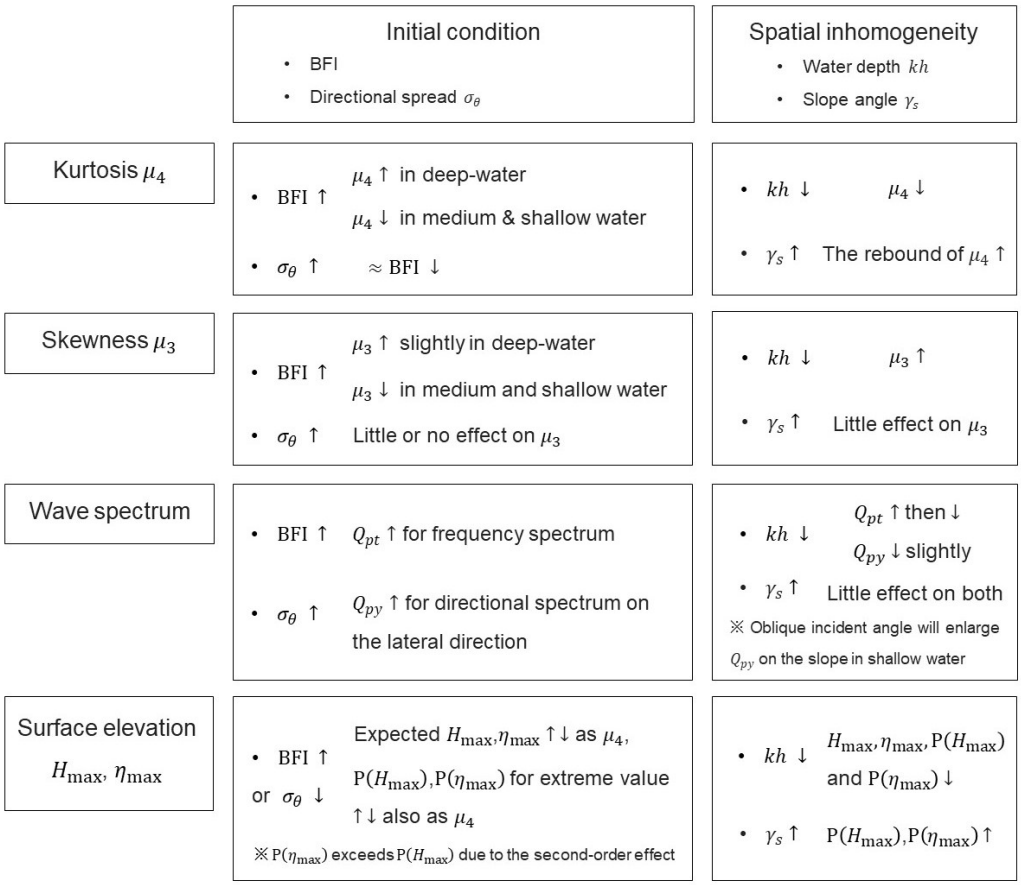

Figure 5.1 The summary of the effect from the initial condition and the bottom topography change acting on the non-linear wave evolution

Bibliography

Alber I., and Saffman P.: Stability of random nonlinear deep-water waves with finite bandwidth spectra. *TRW, Defense and Space System Group Tech*. Rep. 31326-6035-RU-00, 89 pp, 1978.

Banner M. L., Young I. R.: Modeling spectral dissipation in the evolution of wind waves, *Journal of physical oceanography*, 24(7): 1550-1571, 1994.

Benjamin T.B.: Instability of periodic wavetrains in nonlinear dispersive systems. *Proceedings of the Royal Society of London, Series A, Mathematical and Physical Sciences*, 299(1456), pp. 59-76, 1967.

Benney D. J., Newell A. C.: The propagation of nonlinear wave envelopes, *Journal of mathematics and Physics*, 46(1-4): 133-139, 1967.

Chu V. and Mei C.C., On slowly-varying Stokes waves, *Journal of Fluid Mechanics*, Volume 41(4), pp. 873-887, 1970.

Davey A., Stewartson K.: On three-dimensional packets of surface waves, *Proceedings of the Royal Society of London, A, Mathematical and Physical Sciences*, 338(1613), pp. 101-110, 1974.

Dean R.G.: Freak waves: A possible explanation. In A. Torum & O.T. Gudmestad (Eds.), *Water Wave Kinematics,* (pp. 609-612), Kluwer,1990.

Dias F., Kharif C., Nonlinear gravity and capillary-gravity waves. *Annual review of fluid mechanics*, 31(1): 301-346, 1999.

Djordjevic V. D., Redekopp L. G.: On two-dimensional packets of capillary-gravity waves, *Journal of Fluid Mechanics*, 79(4): 703-714, 1977.

Djordjevié V.D., Redekopp L.G.: On the development of packets of surface gravity waves moving over an uneven bottom, *Zeitschrift für angewandte Mathematik und Physik ZAMP*, 29(6), pp. 950-962, 1978.

Draper L.: 'Freak' ocean waves. *Marine Observer* 35, 193-195, 1965.

Dysthe K. B.: Note on a modification to the nonlinear Schrödinger equation for application to

deep water waves, *Proceedings of the Royal Society of London. A, Mathematical and Physical Sciences*, 369(1736): 105-114, 1979.

Dysthe K. B., Trulsen K., Krogstad H., and Socquet-Juglard H.: Evolution of a narrow-band spectrum of random surface gravity waves, *Journal of Fluid Mechanics*, 478, 1–10, 2003.

Ewans K. C.: Observations of the directional spectrum of fetch-limited waves, *Journal of Physical Oceanography*, 28(3): 495-512, 1998.

Forristall G. Z., Ewans K. C.: Worldwide measurements of directional wave spreading, *Journal of Atmospheric and oceanic technology*, 15(2): 440-469 1998.

Franceschetti G., Riccio D.: Scattering, natural surfaces, and fractals, *Elsevier*, 2006.

Goda Y.: Numerical experiments on wave statistics with spectral simulation, *Report Port Harbour Res. Inst*., 9: 3-57, 1970.

Goda Y.: Random Seas and Design of Maritime Structures, 2d ed. *World Scientific*, 464 pp, 2000.

Gramstad O., Trulsen K.: Influence of crest and group length on the occurrence of freak waves, *Journal of Fluid Mechanics*, 582: 463, 2007.

Hammack J. L., Henderson D. M.: Resonant interactions among surface water waves, *Annual review of fluid mechanics*, 25(1): 55-97, 1993.

Hasimoto H., Ono H.: Nonlinear modulation of gravity waves, *Journal of the Physical Society of Japan*, 33(3): 805-811, 1972.

Haver S.: A possible freak wave event measured at the Draupner Jacket January 1 1995, *Rogue waves.* 2004: 1-8, 2004.

Hui W. H., Hamilton J.: Exact solutions of a three-dimensional nonlinear Schrödinger equation applied to gravity waves, *Journal of Fluid Mechanics*, 93(1): 117-133, 1979.

Janssen P.A.E.M.: Nonlinear four-wave interactions and freak waves, *Journal of Physical Oceanography*, 33(4), pp. 863-884, 2003.

Janssen P.A.E.M., Bidlot J. R.: On the extension of the freak wave warning system and its verification, *European Centre for Medium-Range Weather Forecasts*, Memo. 588, 42 pp, 2009.

Janssen T. T., Battjes J. A., Dongeren A. R. Van: Long waves induced by short-wave groups over a sloping bottom, *Journal of Geophysical Research: Oceans*, 108(C8), 2003.

Kashima H., Mori N.: Aftereffect of high-order nonlinearity on extreme wave occurrence from deep to intermediate water, *Coastal Engineering*, 153: 103559, 2019.

Kharif C.， Giovanangeli J.P., Touboul J., et al.: Influence of wind on extreme wave events: Experimental and numerical approaches, *Journal of Fluid Mechanics*, 594: 209-247, 2008.

Krasitskii V. P.: Canonical transformation in a theory of weakly non-linear waves with a nondecay dispersion law, *Journal of Experimental and Theoretical Physics*, 71, 921–927, 1990.

Liu P.L.F., Dingemans M.W.: Derivation of the third-order evolution equations for weakly nonlinear water waves propagating over uneven bottoms, *Wave motion*, 11(1), pp. 41-64, 1989.

Liu P.L.F., Advances in coastal and ocean engineering, *World Scientific*, 1999.

Lo E.Y., Mei C. C.: A numerical study of water-wave modulation based on a higher-order nonlinear Schrödinger equation, *Journal of Fluid Mechanics*, 150: 395-416, 1985.

Lo E. Y., Mei C. C.: Slow evolution of nonlinear deep water waves in two horizontal directions: A numerical study, *Wave motion*, 9(3): 245-259, 1987.

Longuet-Higgins M.: The effect of non-linearities on statistical distributions in the theory of sea waves, *Journal of fluid mechanics*, 1963, 17(3): 459-480, 1963.

Longuet-Higgins M.: On the nonlinear transfer of energy in the peak of a gravity-wave spectrum: a simplified model, *Proceedings of the Royal Society of London. A. Mathematical and Physical Sciences*, 347(1650): 311-328, 1976.

Mei C C., Benmoussa C.: Long waves induced by short-wave groups over an uneven bottom, *Journal of Fluid Mechanics*, 139: 219-235, 1984.

Mori N., Janssen P.A.E.M.: On kurtosis and occurrence probability of freak waves, *Journal of Physical Oceanography*, 36(7), pp. 1471-1483, 2006.

Mori N., Onorato M., Janssen P.A.E.M., Osborne A.R., Serio M., 2007. On the extreme statistics of long-crested deep-water waves: theory and experiments. *Journal of Geophysical Research: Oceans*, 112(C9), 2007.

Mori N., Onorato M., Janssen P.A.E.M.: On the estimation of the kurtosis in directional sea states for freak wave forecasting. *Journal of Physical Oceanography*, 41 (8), 1484-1497, 2011.

Nikolkina I., Didenkulova I.: Rogue waves in 2006–2010, *Natural hazards and Earth system sciences*, 2011, 11(11): 2913-2924, 2011.

Onorato M., Cavaleri L., Fouques S., et al.: Statistical properties of mechanically generated surface gravity waves: a laboratory experiment in a three-dimensional wave basin, *Journal of Fluid Mechanics*, 627, 235–257, 2009a.

Onorato M., Waseda T., Toffoli A., et al.: Statistical properties of directional ocean waves: the role of the modulational instability in the formation of extreme events, *Physical review letters*, 102(11): 114502, 2009b.

Peregrine D. H.: Water waves, nonlinear Schrödinger equations and their solutions, *The ANZIAM Journal*, 25(1): 16-43, 1983.

Segur H., Ablowitz M. J.: Asymptotic solutions and conservation laws for the nonlinear Schrödinger equation. I, *Journal of Mathematical Physics*, 17(5): 710-713, 1976.

Stansberg C.: Extreme waves in laboratory generated irregular wave trains, *Water Wave Kinematics, A. Tørum and O. Gudmestad*, Eds., Kluwer Academic, 573–590, 1990.

Trulsen K., Raustøl A., Jorde S., & Rye L.: Extreme wave statistics of long-crested irregular waves over a shoal, *Journal of Fluid Mechanics*, 882, R2, 2020.

Turpin F.-M., Benmoussa C., Mei C. C.: Effects of slowly varying depth and current on the evolution of a Stokes wavepacket, *Journal of Fluid Mechanics*, 132: 1-23, 1983.

Waseda T.: Impact of directionality on the extreme wave occurrence in a discrete random wave system, *Proceedings of 9th International Workshop on Wave Hindcasting and Forecasting*, Victoria, Canada, Environment Canada, P8, 2006.

Waseda T., Kinoshita T., and Tamura H.: Evolution of a random directional wave and freak wave occurrence, *Journal of Physical Oceanography*, 39, 621–639, 2009.

Yasuda T., Mori N., and Ito K.: Freak waves in a unidirectional wave train and their kinematics, *Proc. 23th Int. Conf. on Coastal Engineering*, Venice, Italy, ASCE, Vol. 1, 751–764, 1992.

Yuen H., Lake B.: Instabilities of waves on deep water, *Annual Review of Fluid Mechanics*, 12(1): 303-334, 1980.

Yuen H., Lake B.: Nonlinear dynamics of deep-water gravity waves, *Advances in applied mechanics*, 22: 67-229, 1982.

Zakharov V.E.: Stability of periodic waves of finite amplitude on the surface of a deep fluid,

Journal of Applied Mechanics and Technical Physics, 9(2), pp. 190-194, 1968.

Zeng H., Trulsen K.: Evolution of skewness and kurtosis of weakly nonlinear unidirectional waves over a sloping bottom, *Natural Hazards and Earth System Sciences*, 12(3), 631, 2012.

Related Peer Reviewed Publication

Lyu, Z., Mori, N., Kashima, H.: Evolution of nonlinear directional random wave train from deep to shallow water, *Journal of Japan Society of Civil Engineers, Series B2(Coastal Engineering)*, 2021, Vol. 77, No.2.

Lyu, Z., Mori, N., Kashima, H.: Freak wave in high-order weakly nonlinear wave evolution with bottom topography change, *Coastal Engineering*, 167: 103918, 2021.

Lyu, Z., Mori, N., Kashima, H.: Evolution of high-order weakly nonlinear waves with bottom topography change, *Journal of Japan Society of Civil Engineers, Series B2(Coastal Engineering)*, 2020, Vol. 76, No.2.

Lyu, Z., Kashima, H., Mori, N.: High order nonlinear wave interactions from deep to finite water depth with bottom topography change, *Proceedings of 36th virtual International Conference on Coastal Engineering*, 2020, Waves.24.